HOW THE CENTRAL AMERICAN SEAWAY ALTERS LARGE-SCALE OCEAN CIRCULATION, CLIMATE AND MARINE BIOGEOCHEMISTRY

by

LORI SENTMAN

A Dissertation submitted to the

School of Graduate Studies

Rutgers, The State University of New Jersey

In partial fulfillment of the requirements

For the degree of

Doctor of Philosophy

Graduate Program in Atmospheric Science

Written under the direction of

Anthony J. Broccoli

And approved by

_____

_____

_____

_____

New Brunswick, New Jersey

January, 2018

ABSTRACT OF THE DISSERTATION

How the Central American Seaway Alters Large-Scale Ocean Circulation, Climate and Marine Biogeochemistry

By LORI SENTMAN

Dissertation Director:

Dr. Anthony J. Broccoli

The study of past climates using climate models and paleoclimate proxy records is helpful for understanding how the Earth system responds to external natural forcing on time scales longer than the current instrumental records. The Central American Seaway (CAS) was an important ocean gateway connecting the Pacific and Atlantic Oceans until its gradual shoaling and final closure near the end of the Pliocene (5.3-2.6 Ma), when paleoclimate proxy records indicate a major reorganization in large-scale ocean circulation and shifting spatial patterns in global climate and marine biogeochemistry. Climate models are not consistent in reconciling the impact of the seaway on global deep-water circulation, tropical Pacific and Southern Hemisphere physical mean state, and interannual tropical Pacific climate variability, and have not been able to explore the

coupled impacts on ocean biogeochemistry or sediment calcium carbonate ($CaCO_3$) long-term burial. For the first time, as far as this author knows, a suite of four idealized experiments, including a very narrow (109 km-wide) single meridional grid point channel, are performed for multi-millennial scale simulations using the Geophysical Fluid Dynamics Laboratory Earth System Model, GFDL-ESM2G, with high ocean spatial resolution to explore the mechanistic role of changing topography – varying only seaway widths and sill depths – associated with the various stages of seaway constriction and shoaling on global ocean circulation, climate and marine biogeochemistry compared to "preindustrial" 1860 climate. Model output is combined with an uncoupled box model to obtain the first sediment $CaCO_3$ (as calcite) long-term burial estimates and atmosphere pCO_2 concentrations associated with a very narrow seaway for comparison with proxy records.

Independent of the CAS configuration in GFDL-ESM2G, the open CAS alters ocean physical mean state and deep water properties globally, driven by the direct impacts of the seaway on global mass, heat and salt transports. Net mass transport from the Pacific through the CAS into the Caribbean is 20.5-23.1 Sv with the 2000-m deep seaways, but only 14.1 Sv for the 200-m shallow seaway. The CAS provided a shortcut for southern sourced Pacific water mass transport, warming the South Atlantic and reducing Indonesian Throughflow mass transport by 59-82%. The CAS suppressed Antarctic Bottom Water northward extent, allowing North Atlantic Deep Water to deepen ~500 m and slightly strengthen (~2Sv), in contrast to preindustrial observational estimates and previous studies with an open CAS using climate models. Global mean climate and tropical Pacific interannual variability are sensitive to the presence of the

CAS, with the largest sensitivity occurring in the Southern Hemisphere for the relatively wide (1308 km) and 2000-m deep CAS. In response to the global ocean reorganization associated with the CAS opened to various shoaling stages, global mean surface air temperatures warm 0.4-0.7°C with a bipolar, asymmetric response of Northern Hemisphere cooling up to ~2°C in the northwest Pacific and Southern Hemisphere warming up to ~8°C near the Ross Sea, in contrast to global mean cooling in climate models. In the tropical Pacific, opening the CAS leads to a global mean warming 0.4-0.8°C in the top 300 m, increased equatorial sea surface temperature gradient in the central and east Pacific, decreased meridional sea surface temperature asymmetry about the equator at 110°W, and the thermocline deepens 5-11 m. Opening the CAS leads to larger El Niño-Southern Oscillation (ENSO) amplitude with more La Niña or cold events, a weaker annual cycle, and ~3 months earlier development.

Opening the CAS results in stronger ventilation and a reduction in the sequestration efficiency of the biological pump, allowing respired CO_2 to escape to the atmosphere via increased ocean CO_2 outgassing. The loss of dissolved inorganic carbon increases the deep ocean carbonate (CO_3^{2-}) leading to a short-term (< 500 kyr) increase in global $CaCO_3$ burial of 0.002 PgC a^{-1} corresponding to large long-term increases in the global sediment $CaCO_3$ pool (~200 PgC over 10^5 years) and a net migration of ~150 PgC from the spatial distribution of $CaCO_3$ in the active layer of 10 cm surface sediment, providing the upper limit on the decrease in ocean alkalinity (~300 PgC), in which alkalinity and DIC are removed in a 2:1 ratio. The enhanced burial of $CaCO_3$ leads to an additional release of 237.9 ppmv (506.8 PgC) to the atmosphere from the partitioning of carbon species implying short-term warming of 0.4-1.0 K in the Pliocene with a very narrow

CAS. Overall, this paleoclimate application has broad implications for the sensitivity of coupled ocean-atmosphere dynamics and ocean biogeochemistry to changing ocean circulation with far-reaching, long-term climate, ENSO, marine ecosystem, ocean biogeochemical, and atmosphere pCO_2 impacts.

Acknowledgements

I express my gratitude to the people who have made this work possible. First and foremost, this work would not have been possible without the support of the NOAA Oceanic and Atmospheric Research Graduate Studies Program and the Geophysical Fluid Dynamics Laboratory (GFDL) director, Dr. V. "Ram" Ramaswamy.

I offer my utmost appreciation to my former GFDL supervisor and mentor, Ronald J. Stouffer. I embarked on this journey with his encouragement and under his guidance, and appreciate his dedication and participation in committee meetings, his broad range of climate expertise, and influence in helping me to think about the "big picture".

I also owe my utmost gratitude to my current GFDL supervisor, mentor, and committee member, Dr. John P. Dunne, for his dedication and being by my side throughout this journey, guiding me with his expertise and insight on oceanography, climate, and ocean biogeochemistry, and challenging me to expand on my research horizons, from which I learned a great deal.

I offer tremendous gratitude to my former GFDL colleague and Rutgers advisor, Dr. Anthony J. Broccoli, for serving as my advisor, his dedication, expertise and insight on paleoclimate, among many other disciplines, and support in a vast array of areas, as well as his personal experience on his similar academic path. I appreciate his guidance and dedication.

I express my sincere gratitude to my committee members, Dr. James R. Miller and Dr. Enrique Curchister, for their dedication, expertise, and insight which improved this research and allowed me to grow academically. I acknowledge their time and effort to serve on my committee.

I owe a debt of gratitude to my colleagues both internal and external to GFDL for their scientific, technical, and personal support; Dr. Robbie Toggweiler, for his expertise and insight on paleoclimate and biogeochemistry, reviewing portions of this research, and participation in many committee meetings which improved this work, Dr. John P. Krasting, for providing the control experiment simulation data, his climate expertise and insight, assistance with diagnostics, reviewing portions of this research, and his personal academic experiences, Dr. Andrew Wittenberg, for his expertise and insight on tropical Pacific interannual variability from which I learned a great deal, and for reviewing portions of this research, Dr. Charles A. Stock, for his expertise and insight on ocean biogeochemistry, Dr. Eric Galbraith for providing preliminary data from which I was able to perform preliminary analysis and defend the proposal for this research, and Zachary Naiman, for his climate expertise and for reviewing portions of this research.

I extend my thanks to Catherine Raphael for enhancing many of the illustration figures. For providing technical support, I thank Dr. Alistair Adcroft, Dr. Matthew J. Harrison, Dr. Zhi Liang, and GFDL Operations, Systems and Model Development teams. I wish to thank Aparna Radhakrishnan and the GFDL Data Portal Team for publicly serving my data, and Erik Mason, National Center for

Atmospheric Research (NCAR) collaborators, and NCAR Climate Analysis Section for providing and supporting the Climate Variability Diagnostics Package. I extend my gratitude to Gail Haller who provided support in obtaining copyright permissions included in this dissertation. Additionally, I would like to thank all of my friends and colleagues at GFDL and Rutgers University whose support and guidance was an integral part of my academic experience.

Finally, but most importantly, I would like to thank my family and friends; without their support this research would not have been possible. I am eternally grateful to my parents, Eileen and the late Bruce Thompson, for their support and encouragement in helping me get to where I am today, instilling in me the confidence that I can do anything I set my mind to, and helping to care for my children to make this accomplishment possible.

I also would like to express my gratitude to my sister, Karen Dreboty, for her support, encouragement, and assistance juggling my children while I completed this dissertation, as well as my mother- and father-in-law, Bernadette and James Sentman.

Lastly, I express my absolute gratitude to my husband, James Sentman, for being by my side and my rock, tirelessly tackling many of the household and family burdens that come with babies that are up all night and very active young children, so that I could pursue my academic goals, and the insight to know when I needed words of encouragement.

Thank you to all of you –without your encouragement and support, this

dissertation would not have been possible.

Dedication

To my sons, Chase, Matthew and Ryan – for being so patient and understanding at such a young age. I hope you learn that you can do anything you set your mind to with dedication and perseverance, just as I learned from my parents.

Table of Contents

Abstract of the dissertation ii

Acknowledgements vi

Dedication x

Table of Contents xi

Chapter 1: Introduction 1

1.1 Motivation 1

1.2 The Evolution of the Central American Seaway (CAS) 4

1.3 Relevant Pliocene Paleoclimate Proxy Indicators 6

1.4 Relevant Idealized CAS Climate Models 9

1.5 Dissertation Overview 15

Chapter 2: Experiment Design 20

2.1 GFDL-ESM2G Description and $CaCO_3$ Long-Term Burial 20

2.2 GFDL-ESM2G Strengths and Biases 23

2.3 GFDL-ESM2G CAS Idealized Experiments 27

Chapter 3: Seaway Impacts on Ocean Physical Mean State and Circulation 31

3.1 Motivation and Overview 31

3.2 Seaway Impacts on Global Ocean Circulation 31

3.3 Seaway Impacts on Inter-basin and Intra-basin Transport 33

3.4 Seaway Impacts on Ocean Physical Mean State 37

3.5 Seaway Impacts on Global Overturning Circulation 40

3.6 Comparison with Proxy Records, Climate Models, and Implications 41

Chapter 4: Sensitivity in Climate Mean State and Interannual Variability to the Seaway 46

4.1 Motivation and Overview 46

4.2 Sensitivity in Global and Inter-hemispheric Time-Mean Climate to the Seaway 46

4.3 Sensitivity in Tropical Time-Mean Climate to the Seaway 49

4.4 Sensitivity in Interannual Climate Variability to the Seaway 54

4.5 Comparison with Proxy Records, Climate Models, and Implications 56

Chapter 5: Ocean Biogeochemical Impacts and Atmosphere pCO_2 Implications 64

5.1 Motivation and Overview 64

5.2 Seaway Impacts on Global Ocean Biogeochemistry 65

5.3 Seaway Impacts on Global Ocean Nutrients and Primary Productivity . 67

5.4 Seaway Impacts on Global and Inter-basin Carbonate Chemistry 71

5.5 Seaway Impacts on Short Time Scale Ocean-Atmosphere Carbon Fluxes and Atmosphere pCO_2 Concentrations 74

5.6 Comparison with Proxy Records, Climate Models, and Implications 76

Chapter 6: Summary and Concluding Remarks 82

6.1 Summary of the Dissertation 82

6.2 Concluding Remarks 86

References 89

List of Tables

Table 1.1. Details of paleoclimate proxy indicators from Ocean Drilling Program (ODP) sites referenced in this dissertation 108

Table 1.2. Details of climate model simulations studying the role of the CAS on ocean circulation, climate, and marine biogeochemistry referenced in this dissertation 109

Table 2.1. GFDL-ESM2G CAS experiment design..... 110

Table 3.1. GFDL-ESM2G global and hemispheric ocean physical mean state 111

Table 4.1. GFDL-ESM2G global and hemispheric atmosphere mean state 112

Table 4.2. GFDL-ESM2G Southern Hemisphere extratropical mean climate 113

Table 4.3. GFDL-ESM2G tropical ocean physical mean state 114

Table 4.4. GFDL-ESM2G equatorial Pacific meridional and zonal temperatures 115

Table 5.1. GFDL-ESM2G global ocean biogeochemical mean state 116

Table 5.2. GFDL-ESM2G global ocean nutrients and productivity 117

Table 5.3. GFDL-ESM2G inter-basin carbonate state 118

List of Illustrations

Fig. 1.1. (a) Comparison of surface water (planktic) oxygen isotope records (‰ vs Vienna Pee Dee Belemnite) from the Caribbean (ODP Site 999; Haug and Tiedemann 1998) and the eastern Pacific (ODP site 851; Cannariato and Ravelo 1997) for 2.2-5.3 Ma showing an increased gradient between ~4.7-4.2 Ma attributed to a major shoaling phase of the CAS (grey shading), reprinted from "Atlantic Deep-water Response to the Early Pliocene Shoaling of the Central American Seaway" by Bell et al. (2015) licensed under *CC-BY-4.0*. Bold lines represent 50 kyr running averages (Haug et al. 2001; Fig. 2A). **(b)** Time series of δ^{13}C data (‰ vs Vienna Pee Dee Belemnite) from various Atlantic ODP sites, reprinted from "Atlantic Deep-water Response to the Early Pliocene Shoaling of the Central American Seaway" by Bell et al. (2015) licensed under *CC-BY-4.0*. Horizontal black lines show average δ^{13}C values for the time slice intervals prior to (5.0-4.7 Ma) and after (4.2-3.6 Ma) CAS shoaling. Arrows indicate approximate modern δ^{13}C values at each site. ODP site details are included in Table 1.1. 119

Fig. 1.2. Temperature evolution of the western and eastern equatorial Pacific since 12 Ma. Republished with permission of American Association for the Advancement of Science, from "A 12-Million-Year Temperature History of the Tropical Pacific Ocean", Zhang, Y. G., M. Pagani, and Z. Liu, *Science*, 344(6179), 2014. 121

Fig. 1.3. (a) Power spectral densities (PSDs) estimated by the maximum-entropy method for PWP fossil corals (blue, coral 1; red, coral 2; Watanabe et al. 2011[1]), **(b)** modern coral $d^{18}O$ (Watanabe et al. 2011[1]), **(c)** the Niño 3.4 index (red, 1950–1984; blue, 1975–2010; Scroxton et al. 2011[2]), **(d)** ENSO Index plots for March, April, and May mean (MAM) at ODP site 846 from HadCM3 running (*left*) preindustrial and (*right*) mid-Piacenzian Warm Period (mPWP; PRISM interval 3.264–3.025 Ma) simulations at two different depths, 5 m (*top*) and 200 m (*middle*; Scroxton et al. 2011[2]), and **(e)** frequency of SST anomalies over the 200 year time series at 5 m and 200 m depth (grey, preindustrial; red, mPWP; Scroxton et al. 2011[2]). ODP site details are included in Table 1.1. [1] Reprinted by permission from Macmillan Publishers Ltd: Nature, Watanabe, T., and Coauthors, Permanent El Niño during the Pliocene warm period not supported by coral evidence, 471, 209–211, copyright 2011. [2] Reprinted with permission from "Persistent El Niño-Southern Oscillation variation during the Pliocene Epoch" by Scroxton et al. (2011) licensed under *CC-BY-3.0.*..... 122

Fig. 1.4. Carbonate sand-fraction mass accumulation rates (sand MAR) at ODP sites 999 (Colombian basin, *left axis*) and 846 (eastern tropical Pacific basin, *right axis*) for 2–5.3 Ma. Reprinted by permission from Macmillan Publishers Ltd.: Nature Publishing Group (Haug and Tiedemann, Nature, 393, 674-676, copyright 1998).. 124

Fig. 2.1. GFDL-ESM2G bathymetry (m; shaded) for **(a)** CLOSED, **(b)** NARROW, **(c)** WIDE, and **(d)** WIDESHALLOW seaway simulations and 5-m ocean velocity (m s^{-1}; vectors). Stars show locations of local ODP drilling sites 999 (red), 851 (green), 929 (purple) and 925 (yellow) referenced in Fig. 1.1 and Fig. 1.4. The yellow boxes (18º-8ºN; 100º-77 ºW) in **(c)** and **(d)** and transect (77.5ºW; 8.2ºN) in **(b)** were used for the WIDE/WIDESHALLOW and NARROW transport calculations (Section 3.3), respectively. See Table 2.1 for the GFDL-ESM2G CAS experiment widths and depths. ODP site details are included in Table 1.1..... 125

Fig. 2.2. Paleogeography reconstructions of Central America in the mid-Miocene before the Isthmus of Panama; **(a)** archipelago model (Coates and Obando 1996) reprinted from (Kirby and MacFadden 2005) with permission from Elsevier[1], **(b)** peninsula model (Whitmore and Stewart 1965) reprinted from (Kirby and MacFadden 2005) with permission from Elsevier[1], and **(c)** early seaway model similar to climate models (Table 1.2), republished with permission of *Oceanus Magazine*, from "How the Isthmus of Panama put ice in the Arctic", G. H. Haug and L. D. Keigwin, 42, 2, 2004; permission conveyed through Copyright Clearance Center, Inc. Emergent land is represented by gray **(a)** and **(b)** and tan **(c)**. Timing and structure of the paleogeography is uncertain (Kirby and MacFadden 2005). [1]**(a)** and **(b)** reprinted from *Palaeogeogr. Palaeoclimatol. Palaeoecol.*, M.X. Kirby and B. MacFadden. "Was southern Central America an archipelago or a peninsula in the middle Miocene? A test using land-mammal body size", Vol. 228, No. 3-4, p. 193–202, 2005, Copyright Elsevier with permission from Elsevier. 127

Fig. 2.3. GFDL-ESM2G global average upper 2000-m ocean temperature (°C) for the CLOSED (black), NARROW (red), WIDESHALLOW (green), and WIDE (blue) seaway simulations for model integration years 1-4000. The yellow shading represents the 100-year analysis period (1301-1400) mainly used in this study (except for the maximum Atlantic Meridional Overturning Circulation analysis). The wide seaway experiments (e.g., WIDE and WIDESHALLOW) began with a warmer global integrated ocean and average surface air temperature than the NARROW seaway experiment because more land grid cells were replaced with warm, tropical ocean grid cells than in the NARROW seaway. The global average upper 2000-m ocean temperature for the WIDESHALLOW seaway converges toward the NARROW simulation faster than the WIDE simulation that was initialized with additional warm ocean grid cells. The NARROW and WIDE simulations were integrated longer than the spin-up and analysis periods to assess the convergence rate. The WIDE simulation converges toward the NARROW simulation at a rate of approximately 0.1˚C / 1000 years, requiring an additional 1000 integration years for near-convergence. 128

Fig. 2.4. Global annual (black) average atmosphere pCO_2 flux from the land and ocean (PgC a^{-1}) for the **(a)** CLOSED and **(b)** NARROW GFDL-ESM2G seaway simulations. 5-year boxcar smoothing is applied (red) to the annual average values (black). Green lines indicate ±1 PgC a^{-1} for evaluation of quasi-equilibrium via the CMIP5 criteria defined in Dunne et al. (2012b). 130

Fig. 3.1. Simplified GFDL-ESM2G global ocean circulation (modified from Rahmstorf (2002)) for the **(a)** CLOSED, **(b)** NARROW, **(c)** WIDE, and **(d)** WIDESHALLOW seaway simulations. Red (blue) lines indicate surface (deep/bottom) waters. Yellow ovals indicate deep-water formation regions. Shading represents regions with salinity > 36 psu (green) and < 34 psu (blue). 131

Fig. 3.2. Sea surface height (SSH) anomalies (m) relative to the global mean for the **(a)** CLOSED, **(b)** NARROW, **(c)** WIDESHALLOW, and **(d)** WIDE GFDL-ESM2G seaway simulations. Blue (red) contours indicate positive (negative) SSH anomalies. 132

Fig. 3.3. GFDL-ESM2G 100-year annual average vertically integrated full-depth current (m s^{-1}; vectors) from 20ºN-20ºS for **(a)** WIDE, **(b)** WIDESHALLOW, **(c)** NARROW, **(d)** CLOSED, and the time progression of the gradual shoaling and closure of the seaway: **(e)** WIDE-WIDESHALLOW, **(f)** WIDESHALLOW-NARROW, and **(g)** NARROW-CLOSED differences. 133

Fig. 3.4. GFDL-ESM2G 100-year annual average depth-integrated **(a)** net inter-basin and **(b)** bi-directional inter- and intra-basin mass transport (Sv; 10^6 m^3 s^{-1}) exchange in the CAS region as defined by the yellow transect (Fig. 2.1b; 77.5ºW; 8.2ºN) and boxes (Fig. 2.1c and Fig. 2.1d; 18º-8ºN; 100º-77ºW) for the NARROW and WIDE/WIDESHALLOW experiments, respectively. Positive (negative) mass transport values indicate transport from the Pacific to the Caribbean (Caribbean to Pacific). Full depth-integrated net inter-basin mass transport (Sv) values are included in parenthesis in the legend. 135

Fig. 3.5. GFDL-ESM2G 100-year annual average **(a)** net water mass (Sv; 10^6 m^3 s^{-1}), **(b)** ocean heat (PW), and **(c)** salt (10^6 kg s^{-1}) transports calculated for the CLOSED (black), NARROW (red), WIDE (blue), and WIDESHALLOW (green) seaway experiments for 13 transects in the Pacific (green), Atlantic (blue), and Indian (magenta) Oceans. Total transport is integrated from 0-5499 m with northward/eastward (southward/westward) positive (negative). Bering Strait (green) at 65ºN; North Pacific Ocean (green) at 25ºN; South Pacific Ocean (green) at 30ºS; CAS NARROW (green) at 77.5ºW and 8.2ºN; CAS WIDE and WIDESHALLOW (green) at 18º-8ºN and 100º-77 ºW; Drake Passage (green) at 70ºW; Denmark Strait (blue) at 65ºN; GIN Seas/Denmark Strait/Labrador Sea (blue) at 58ºN; North Atlantic (blue) at 25ºN; South Atlantic (blue) at 30ºS; Africa to Antarctica (blue) at 25ºE; South Indian Ocean (magenta) at 30ºS; Indonesian Throughflow (magenta) at 115ºE; Australia to Antarctica (magenta) at 115ºE. The yellow shading **(b)** indicates the only transport direction reversal. 136

Fig. 3.6. GFDL-ESM2G 100-year annual average NARROW (red), WIDE (blue), and WIDESHALLOW (green) minus CLOSED northward **(a)** ocean heat transport (PW) and **(b)** salt transport (10^6 kg s^{-1}) difference. 138

Fig. 3.7. GFDL-ESM2G 100-year annual average **(a)** CLOSED, **(b)** NARROW-CLOSED, **(c)** WIDESHALLOW-CLOSED, and **(d)** WIDE-CLOSED differences in sea surface temperature (SST; ºC; *left*) and sea surface salinity (SSS; psu; *right*) for the four seaway simulations. 140

Fig. 3.8. GFDL-ESM2G 100-year annual average precipitation rate minus evaporation rate (cm day^{-1}) for **(a)** NARROW-CLOSED, **(b)** WIDESHALLOW-CLOSED, and **(c)** WIDE-CLOSED. 142

Fig. 3.9. GFDL-ESM2G 100-year annual average **(a)** CLOSED, **(b)** NARROW-CLOSED, **(c)** WIDESHALLOW-CLOSED, and **(d)** WIDE-CLOSED differences in the upper 100-m average ocean density (kg m^{-3}, *left*), and changes in the upper 100-m average ocean density from only changes in salinity with a seaway (kg m^{-3}, *middle*), and from only changes in temperature with a seaway (kg m^{-3}, *right*) for the four seaway simulations. Coefficient of determination (r^2) values are indicated in red. 143

Fig. 3.10. GFDL-ESM2G 100-year annual average vertical profiles of ocean density (kg m^{-3}; *left*), salinity (psu; *middle*), and temperature (°C; *right*) for the **(a)** Atlantic, **(b)** Pacific, **(c)** Southern, and **(d)** Indian Oceans for the CLOSED (black dashed), NARROW (red), WIDE (blue), and WIDESHALLOW (green) seaway experiments. 146

Fig. 3.11. GFDL-ESM2G 100-year annual average global (*left*) and North Atlantic (*right*) meridional overturning streamfunction (1 Sv=10^6 m^3 s^{-1}) for the **(a)** CLOSED, **(b)** NARROW, **(c)** WIDESHALLOW, and **(d)** WIDE seaway experiments. Positive (negative) values in red (blue) indicate clockwise (counterclockwise) circulation. 148

Fig. 3.12. Maximum Atlantic Meridional Overturning Circulation (AMOC; Sv) time series in density space from 20º-80ºN for the CLOSED (black), NARROW (red), WIDESHALLOW (green), and WIDE (blue) seaway experiments for model integration years 1-4000. The yellow shading indicates the 500-year period (1001-1500) used to compute the maximum AMOC values shown and 50-year boxcar smoothing is applied. 149

Fig. 3.13. GFDL-ESM2G 100-year annual average relative contribution of NADW (%) computed from (Eq. 1) and characterized by salinity for the **(a)** CLOSED, **(b)** NARROW, **(c)** WIDESHALLOW, and **(d)** WIDE seaway experiments. The calculation is based on Oppo and Fairbanks (1987) using end members chosen to represent the average salinity of the North Atlantic (20º-80 ºN; 30º-50ºW) and Drake Passage (50º-70 ºS; 70 ºW) from 1469-5499 m. 150

Fig. 4.1. GFDL-ESM2G 100-year annual global average **(a)** northward total (atmosphere plus ocean) heat transport (PW), **(b)** northward total heat transport difference with the CAS (PW), and **(c)** northward total heat transport difference with CAS (PW) by component with atmosphere (solid) and ocean (dashed) for the CLOSED (black), NARROW (red), WIDESHALLOW (green), and WIDE (blue) seaways 151

Fig. 4.2. GFDL-ESM2G 100-year annual average 2-m surface air temperature (SAT; K; *left*) and precipitation rate (mm day^{-1}; *right*) for **(a)** CLOSED and the differences between the **(b)** NARROW, **(c)** WIDESHALLOW, and **(d)** WIDE and CLOSED seaway experiments. 153

Fig. 4.3. GFDL-ESM2G 100-year annual average difference in **(a)** 2-m surface air temperature (SAT; K; *left*) and **(b)** precipitation rate (mm day^{-1}; *right*) between the CMIP5 RCP2.6 experiment and CLOSED seaway experiment (i.e., CMIP5 1860 preindustrial control)..... 154

Fig. 4.4. GFDL-ESM2G 100-year zonal average **(a)** precipitation rate (mm day^{-1}), **(b)** 2-m surface air temperature (SAT; K), **(c)** total cloud amount (%), and **(d)** 2-m zonal wind (m s^{-1}) NARROW-CLOSED (red), WIDESHALLOW-CLOSED (green), and WIDE-CLOSED (blue) differences, and CLOSED (d; black) seaway simulations..... 155

Fig. 4.5. GFDL-ESM2G 100-year annual average tropical (20ºN-20ºS) SST (ºC; *left*), 0-300m average ocean temperature (ºC; *middle*), and 20ºC isotherm depth (m; *right*) for **(a)** CLOSED, and the difference between **(b)** NARROW, **(c)** WIDESHALLOW, and **(d)** WIDE and CLOSED. The dotted region indicates the Niño-3 region (5°N-5°S, 150°-90°W). 156

Fig. 4.6. GFDL-ESM2G 100-year annual equatorial Pacific (2°N-2°S, 140°E-90°W) meridional average **(a)** SST (°C) and **(b)** depth of maximum *dT/dz* (m; representing the thermocline depth), and slice at 110°W **(c)** SST (°C) and **(d)** depth of maximum *dT/dz* (m) for the CLOSED (black dash), NARROW (red), WIDESHALLOW (green), and WIDE (blue) seaway simulations. 158

Fig. 4.7. GFDL-ESM2G 100-year annual equatorial Pacific (2°N-2°S, 140°E-90°W) meridional average difference in **(a)** SST (°C) and **(b)** depth of maximum *dT/dz* (m; representing the thermocline depth), and slice at 110°W difference in **(c)** SST (°C) and **(d)** depth of maximum *dT/dz* (m) between the NARROW (red), WIDESHALLOW (green), and WIDE (blue) and the CLOSED seaway simulations. Zero line is included for reference (black dash). 159

Fig. 4.8. GFDL-ESM2G Niño-3 (5°N-5°S, 150°-90°W) time series for 500-year (model years 1001-1500) monthly average sea surface temperatures (SST; °C) for the **(a)** CLOSED, **(b)** NARROW, **(c)** WIDESHALLOW, and **(d)** WIDE seaway simulations. Grey, black, and red lines indicate monthly, annual, and decadal time-averages. 160

Fig. 4.9. GFDL-ESM2G Niño-3 (5°N-5°S, 150°-90°W; dotted box in Fig. 4.5) 500-year monthly average SST spectral density period (years; *left*) and SST power spectra ($°C^2$ $octave^{-1}$) vs period (years; *right*) for the **(a)** CLOSED, **(b)** NARROW, **(c)** WIDESHALLOW, and **(d)** WIDE seaway simulations and from NOAA's Extended Reconstruction version 4 for 1880-2016 observations (ERSST.v4; Huang et al. 2015; black, *right*). Details of the wavelet analysis method are described in Wittenberg et al. (2006, caption in their Fig. 20). 161

Fig. 4.10. GFDL-ESM2G 500-year average **(a)** El Niño (*left*) and **(b)** La Niña (*right*) Hovmöller SST anomaly (°C) average (3°N-3°S, 85°E-150°W) composites for the Hadley Centre Sea Ice and Sea Surface Temperature (HadISST) data set (Rayner et al. 2003) (black dash), CLOSED (black solid), NARROW (red), WIDESHALLOW (green), and WIDE (blue) seaway simulations..... 162

Fig. 4.11. Niño-3.4 (5°N-5°S, 170-120°W) spatial composite maps of 2-m air and sea surface temperature (°C; shaded) and mean sea level pressure (hPa; contours) anomalies for DJF^{+1} (boreal winter year 1) for the **(a)** Hadley Centre Sea Ice and Sea Surface Temperature (HadISST) data set (Rayner et al. 2003), NOAA Merged Land-Ocean Surface Temperature Analysis V3.5.3 (MLOST; Vose et al. 2012), and NOAA CIRES Twentieth Century Global Reanalysis version 2 (20thC_ReanV2; Compo et al. 2009) 1920-2011 observations, and GFDL-ESM2G 500-year **(b)** CLOSED, **(c)** NARROW, **(d)** WIDESHALLOW, and **(e)** WIDE seaway simulations..... 163

Fig. 5.1. Global annual **(a)** ocean mean ideal age (years), **(b)** ocean NO_3^- inventory (PgN), **(c)** ocean alkalinity inventory (exagrams C equivalent), **(d)** ocean dissolved inorganic carbon inventory (DIC; exagrams C; EgC), **(e)** annual air-sea CO_2 flux (PgC a^{-1}; positive flux into the ocean), **(f)** integrated air-sea CO_2 flux (PgC; positive flux into the ocean), **(g)** annual ocean surface sediment $CaCO_3$ burial flux (PgC a^{-1}; solid lines; positive flux downward), river runoff flux of DIC (PgC a^{-1}; dashed lines); values represent long-term (~100 kyr) results using the offline calcite box model, **(h)** ocean surface sediment $CaCO_3$ inventory (PgC), **(i)** annual atmosphere pCO_2 flux from land and ocean ($PgCO_2$ a^{-1}; positive flux into atmosphere), and **(j)** annual integrated atmosphere pCO_2 flux from land and ocean (PgC; positive flux into atmosphere) for the CLOSED (black) and NARROW (red) GFDL-ESM2G seaway simulations. 20-year **(e)** and **(g),** and 50-year **(i)** boxcar smoothing is applied. Dashed lines represent the air-sea interface (zero line) in **(f)** and **(j)**. 165

Fig. 5.2. 100-year **(a)** global monthly and **(b)** zonal annual average mixed layer depth (m) for the CLOSED (black dash) and NARROW (red) GFDL-ESM2G seaway simulations. 166

Fig. 5.3. 100-year annual average ocean ideal age (years) at 500 m (*left*) and 2049 m (*right*) for the **(a, b)** CLOSED, and **(c, d)** NARROW-CLOSED, **(e, f)** WIDESHALLOW-CLOSED, and **(g, h)** WIDE-CLOSED difference in the GFDL-ESM2G seaway simulations. 167

Fig. 5.4. 100-year global annual mean nitrate (NO_3^-) concentration (μmol kg^{-1}) averaged in the top 100 m (*left*) and total net primary productivity (NPP; molC m^{-2} a^{-1}) from NO_3^- using Anderson (1995) stoichiometry integrated in the top 100 m (*right*) for the **(a)** CLOSED and **(b)** NARROW-CLOSED difference in the GFDL-ESM2G seaway simulations. 168

Fig. 5.5. 100-year global annual mean nitrate (NO_3^-) concentration (μmol kg^{-1}) at 2049 m (*left*) and particulate organic nitrogen sinking flux (molC m^{-2} a^{-1}) at 100 m (*right*) using Anderson (1995) stoichiometry for the **(a)** CLOSED and **(b)** NARROW-CLOSED difference in the GFDL-ESM2G seaway simulations. 169

Fig. 5.6. 100-year global annual mean phosphate (PO_4^{3-}) concentration (μmol kg^{-1}) averaged in the top 100 m (*left*) and total net primary productivity (molC m^{-2} a^{-1}) from PO_4^{3-} using Anderson (1995) stoichiometry integrated in the top 100 m (*right*) for the **(a)** CLOSED and **(b)** NARROW-CLOSED difference in the GFDL-ESM2G seaway simulations. 170

Fig. 5.7. 100-year global annual mean phosphate (PO_4^{3-}) concentration (μmol kg^{-1}) at 2049 m (*left*) and particulate organic phosphate sinking flux (molC m^{-2} a^{-1}) at 100 m (*right*) using Anderson (1995) stoichiometry for the **(a)** CLOSED and **(b)** NARROW-CLOSED difference in the GFDL-ESM2G seaway simulations. 171

Fig. 5.8. 100-year global annual mean dissolved iron (Fe) concentration (nmol kg^{-1}) in the top 100 m (*left*), at 2049 m (*middle*), and total net primary productivity (molC m^{-2} a^{-1}) from Fe using 10,000C:1Fe stoichiometry (Anderson and Morel 1982; Morel and Hudson 1985) integrated in the top 100 m (*right*) for the **(a)** CLOSED and **(b)** NARROW-CLOSED difference in the GFDL-ESM2G seaway simulations..... 172

Fig. 5.9. 100-year annual average dissolved oxygen (μmol kg^{-1}) averaged from 200-1000 m for the **(a)** CLOSED and **(b)** NARROW-CLOSED difference in the GFDL-ESM2G seaway simulations. 173

Fig. 5.10. Vertical profiles of global average concentrations of **(a)** dissolved O_2 (μM), **(b)** total (solid) and preformed (dashed) PO_4^{3-} (μM), and **(c)** apparent oxygen utilization (AOU; μM) for the CLOSED (black) and NARROW (red) GFDL-ESM2G seaway simulations. AOU in **(c)** computed from the difference between O_2 at saturation assuming equilibrium with the air-sea interface and actual dissolved O_2 concentrations. The difference in remineralized dissolved inorganic carbon (ΔDIC_{remin}) between the NARROW and CLOSED seaways is 241 PgC released to the atmosphere. 174

Fig. 5.11. 100-year annual average ocean alkalinity (*left*) and dissolved inorganic carbon, DIC (*right*) at 2049 m depth for the **(a)** CLOSED and **(b)** NARROW-CLOSED difference in the GFDL-ESM2G seaway simulations. Units are in μmol kg^{-1}..... 175

Fig. 5.12. Global 100-year annual zonal average **(a)** atmosphere pCO_2 flux from the land and ocean (PgC a^{-1} deg^{-1}; positive into the atmosphere) and **(b)** from the ocean only (PgC a^{-1} deg^{-1}; positive into the atmosphere), and **(c)** annual total meridional atmosphere CO_2 flux transport (PgC a^{-1}; northward positive) for the CLOSED (black) and NARROW (red) GFDL-ESM2G seaway simulations. Dashed line (zero line) represents the air-sea interface..... 176

Fig. 5.13. 100-year annual average air-sea CO_2 flux (mol m^{-2} a^{-1}) for the **(a)** CLOSED and **(b)** NARROW GFDL-ESM2G seaway simulations. Positive values (red) indicate a flux out of the ocean. 177

Chapter 1

Introduction

1.1 Motivation

The study of past climates, or paleoclimates, is helpful to better understand how the Earth system – the coupled climate and carbon cycle – responds to external natural forcing such as solar, orbital, geological, and atmospheric composition on multi-centennial to millennial time scales, and abrupt transitions between climate states on decadal to centennial time scales. Paleoclimate information documents these changes and is important for evaluating Earth system feedbacks and variability on time scales longer than the present instrumental records (Masson-Delmotte et al. 2013). The Central American Seaway (CAS) was an important ocean gateway connecting the Pacific and Atlantic Oceans until around the end of the Pliocene (5.3-2.6 Ma, mega-annum; Schmidt 2007). The CAS is of great interest to both the paleoclimate proxy (Table 1.1) and climate modeling communities (Table 1.2) because it is hypothesized to have reorganized the large-scale ocean circulation, and significantly changed climate and ocean biogeochemistry. Understanding the coupled physical and biogeochemical mechanisms involved in these changes before and after the CAS closure is important for a better understanding of how the Earth system will respond to external natural and anthropogenic forcings in the future.

Variability in the Atlantic Meridional Overturning Circulation (AMOC) – an important component of the global ocean circulation – affects Atlantic sea surface temperature (SST) variability and impacts climate (Kushnir 1994; Delworth and Mann

2000; Knight et al. 2005; O'Reilly et al. 2016). Models of various complexity show that the AMOC is sensitive to changes in extratropical salinity fluxes (Stommel 1961; Bryan 1986; Manabe and Stouffer 1988; Mikolajewicz and Maier-Reimer 1994; Rahmstorf 1995; Schiller et al. 1997; Yin and Stouffer 2007). Changes in the AMOC impact global climate through changes in inter-hemispheric heat flux (Broecker et al. 1998; Stocker 1998) and may contribute to abrupt climate transitions (Manabe and Stouffer 1988). Recently, Delworth and Zeng (2016) demonstrated that the positive phase of the North Atlantic Oscillation strengthens the AMOC and increases horizontal density gradients and deep-water formation. However, the rate and magnitude of changes in the AMOC in response to changes in future climate is very uncertain (Kirtman et al. 2013). North Atlantic hosing (i.e., anomalous freshwater input) experiments aimed at shutting down the AMOC simulate both a weakening of El Niño-Southern Oscillation (ENSO) variability – the leading mode of present-day tropical Pacific interannual variability – as the tropical thermocline deepens (Timmermann et al. 2005), and an amplification in ENSO variability as the annual cycle weakens (Dong and Sutton 2007; Timmermann et al. 2007).

Ocean source water mixing and the associated changes in ocean ventilation governing the exchange rate between the deep ocean and surface, affect the sequestration efficiency of the ocean pumps (e.g., biological) with implications for changing global marine nutrient concentrations, net primary productivity (NPP), and various biogeochemical cycles including atmospheric CO_2 concentrations (Broecker, 1982). Changes in ventilation affect the regional supply of chemical species (e.g., carbon) and nutrients from below the surface as well as their regional sequestration in deep water. The

marine environment provides about half of the global NPP via phytoplankton production (Falkowski et al. 1998; Field et al. 1998) and is controlled by factors such as temperature, carbon dioxide (CO_2), nutrient supply, and light through radiative properties and ocean mixed-layer depths. Ventilation of oxygen minimum zones (OMZs), or severely hypoxic regions where dissolved oxygen (O_2) concentration falls below 0.5 mL L^{-1} or 22 μmol kg^{-1} or 7.5% saturation (Kamykowski and Zentara 1990; Levin 2003; Rogers 2000), has implications for altering marine biodiversity and global ocean biogeochemical cycling. Furthermore, ocean physical mean state properties (e.g., temperature and salinity) affect the solubility of CO_2 and, thereby, its air-sea exchange. The sequestration time scales of the biological pump impact the concentration of dissolved carbonate (CO_3^{2-}) in the deep ocean and its sequestration or dissolution as calcium carbonate ($CaCO_3$) is formed in seawater. The dissolution or precipitation of $CaCO_3$ drives changes in global total alkalinity, air-sea CO_2 exchange, and atmosphere pCO_2 (i.e., the volume fraction of CO_2 in the atmosphere in ppmv) concentrations via the partitioning of carbon species and carbonate chemistry. Therefore, the mixing of Atlantic and Pacific water masses and their physical mean state properties with the addition of the CAS during the Pliocene has important implications for ocean biogeochemistry and NPP, and short time scale (<500 kyr in the absence of chemical weathering) atmosphere pCO_2 concentrations.

In fact, there is "medium confidence" that atmosphere pCO_2 concentrations (~350-450 ppmv) during the Mid-Pliocene Warm Period (~3.3-3 Ma) were higher than preindustrial, or year 1860 (286 ppm), and global mean surface air temperatures (SATs) were 1.9 to 3.6 °C higher than preindustrial levels, and "high confidence" in polar amplification in response to these changes in atmosphere CO_2 concentrations (Masson-

Delmotte et al. 2013). These mean climate patterns of the Pliocene are analogous to the projected mean climate as a result of increasing present-day concentrations of greenhouse gases (Dowsett et al. 2012). Therefore, a better understanding of the mechanisms driving changes in global ocean circulation and, thereby, the oceanic heat and carbon uptake, their effect on climate and marine biogeochemistry, and how the Earth system responds to forcing on a variety of time scales in paleoclimates is helpful in improving confidence in climate model decadal predictions and climate projections.

1.2 The Evolution of the Central American Seaway (CAS)

The gradual closure of the CAS was the result of the underthrusting of the Cocos Ridge under Costa Rica and western Panama, and the emergence and collision of the Central American volcanic arc, as part of the trailing edge of the Caribbean plate, wedged between the Yucatan Peninsula and South America (Sykes et al. 1982) between 12.8 and 7.1 Ma (Duque-Caro 1990; Coates et al. 2004). It is suggested that this collision shut off deep-water flow across the CAS (Montes et al. 2012a, 2012b), supported by the divergence of benthic foraminiferal faunas between the Caribbean and Pacific between 12 and 10 Ma, inferring that the sill uplifted by 1000 m around this time (Duque-Caro 1990). Shallow water exchange continued after this time and ceased around 3.5 Ma (Molnar 2008, and references therein). However, the timing of final closure between 1 Ma and ca. 5 Ma (Corrigan et al. 1990; Lonsdale and Klitgord 1978; Collins et al. 1995; de Boer et al. 1995) remains controversial.

The “Great American Exchange” of land mammals between North and South

America began ca. 3 Ma and major exchange is precisely dated ca. 2.6-2.7 Ma (Marshall 1985; Webb 1985; Webb and Rancy 1996). This was originally proposed to have marked the CAS final closure since inter-continental mammal exchange required a continuous land bridge. However, Molnar (2008) suggested that the exchange may actually be the result of vegetation biome changes associated with climate change from intensification of Northern Hemisphere Glaciation (NHG) ca. 3.1 to 2.7 Ma, rather than climate changes due to the closure of the CAS. Recently available neodymium and lead isotopes from the Ocean Drilling Program (ODP) sites (Table 1.1) in the eastern equatorial Pacific (EEP) and Caribbean have been used to better constrain the final stages of the CAS closure, which affected changes in ocean circulation and climate, and the width of the seaway, believed to be important for water mass throughflow. However, these records have conflicting timelines. One record indicates a narrowing of the CAS to 200 km by the early Miocene (ca. 23-17 Ma) and final closure by 12 Ma (Montes et al. 2012a, 2012b), long before NHG and proxy record evidence suggest changes in ocean circulation. Another record indicates restriction in deep water exchange by 7 Ma and periodic shallow exchange until ~2.5 Ma (Osborne et al. 2014). Sepulchre et al. (2014) included neodymium isotope responses to the shoaling of the CAS in coupled atmosphere ocean general circulation model (AOGCM; hereafter simply referred to as climate models) simulations and inferred that a 50 to 200 m deep sill could have been achieved by 10 Ma. Thus, additional paleoclimate proxy records are needed to better constrain the time of final closure. Therefore, this dissertation is an attribution study focusing on the time-independent, mechanistic role of the presence and evolution of the CAS's topography on ocean circulation, climate and marine biogeochemistry to better constrain the available

paleoclimate proxy indicators.

1.3 Relevant Pliocene Paleoclimate Proxy Indicators

Early Pliocene mixed-layer δ^{18}O planktonic foraminifera (*G. Sacculifer*) records (Keigwin 1982) and Cd/Ca measurements (Maier-Reimer et al. 1990) suggest that prior to 4 Ma, sea surface salinity (SSS) in the EEP and Caribbean were similar. Divergence in the mixed-layer δ^{18}O records after 4 Ma indicates 1.0-1.5 psu depletion in Caribbean Pliocene SSS (Keigwin 1982). Furthermore, around 4.4 Ma, diverging planktonic foraminifera δ^{18}O records from the Caribbean and EEP (Table 1.1) indicate a build-up of the modern Pacific-Caribbean salinity contrast (Fig. 1.1a; Haug and Tiedemann 1998). These records are also consistent with increasing foraminiferal Mg/Ca ratios at the same time (4.4 Ma), indicating rising temperatures in the Caribbean consistent with isolation from the EEP (Groeneveld et al. 2008). From ~3.3-2.6 Ma, global mean SATs experienced a long-term decrease and ice volume increased (Lisiecki and Raymo 2005; Mudelsee and Raymo 2005; Fedorov et al. 2013). Recent Ross Sea and Antarctic proxy indicator reconstructions indicate reduced sea ice extent and duration before 3.3 Ma which is believed to have preconditioned the Northern Hemisphere (NH) for continental glaciation (McKay et al. 2012). In addition, proxy records (e.g., foraminifera, Mg/Ca ratios, and alkenone unsaturation index) imply that sea surface temperatures (SSTs) in the EEP cold tongue were similar to those in the tropical West Pacific Warm Pool (WPWP) before ~4 Ma (Chaisson and Ravelo 2000; Molnar and Cane 2002; Ravelo et al. 2004;

Wara et al. 2005; Fedorov et al. 2006; Steph et al. 2010). Low- and mid-latitude upwelling regions were characterized by warm surface water, a deep thermocline, and low biogenic productivity (Fedorov et al. 2006; Dekens et al. 2007) during the Pliocene.

Proxy records used to determine the strength of North Atlantic Deep Water (NADW) formation – an important component of the AMOC – based on ODP sites (Table 1.1) in the western Caribbean and deep equatorial Western Atlantic suggest reduced deep-water formation with the open CAS (Burton et al. 1997; Haug and Tiedemann 1998; Driscoll and Haug 1998; Billups et al. 1998; Haug et al. 2001; Frenz et al. 2006; Steph et al. 2010; Osborne et al. 2014). In particular, higher benthic δ^{13}C values and better carbonate preservation in the Caribbean at ODP Site 999 (Table 1.1) between 5 and 2 Ma indicate stronger ventilation, attributed to intensification of NADW in association with the gradual shoaling and closure of the CAS (Haug and Tiedemann 1998). However, there are discrepancies among the interpretations of these records. δ^{13}C records from benthic foraminifera, *Cibicidoides* (Woodruff and Savin 1989) suggest that NADW production increased after 10-12 Ma, significantly before the estimated CAS final closure (Section 1.2). Furthermore, analysis of marine sediment mass age distribution indicates an increase in the Pliocene to Quaternary (2.588 Ma to present) sediment mass compared to before the Pliocene and is attributed to erosion of sediment older than the Pliocene by deep water currents, suggesting high values of NADW formation during the Pliocene (Wold et al. 1994). Additional evidence for strong NADW formation during the Pliocene and an overall decrease in NADW production over the past ~3 Ma has been deduced from δ^{13}C comparisons of North Atlantic and Pacific sediments (Raymo et al. 1990, 1992; Raymo 1997). Micropaleontological results indicate increased influence of

southern component mass water in the North Atlantic and suggest reduced NADW formation (Ishman 1996) after 2.9 Ma, or after the estimated time of CAS final closure. Recently, Bell et al. (2015) analyzed $\delta^{13}C$ and $\delta^{18}O$ from ODP sites (Table 1.1) in the Atlantic, including the South Atlantic – a key area for the southern extent of NADW – and concluded that deep-water formation was as strong and frequently stronger in the early Pliocene (~4.7 Ma) compared to modern-day (Fig. 1.1b). Thus, there are inconsistencies in the paleoclimate proxy records regarding the strength of NADW during the Pliocene, requiring additional proxy indicators and climate models to better understand the role of the open CAS on NADW formation.

The "permanent El Niño-like state" of the Pliocene (Philander and Fedorov 2003) is inferred from a reduced east-west (i.e., zonal) tropical Pacific SST gradient that terminated ~3-4 Ma (Wara et al. 2005; Lawrence et al. 2006; Fedorov et al. 2006; Steph et al. 2010), and paleoclimate terrestrial records indicating that ENSO teleconnection patterns ~3 Ma were similar to those associated with present-day El Niños (Molnar and Cane 2002). Trends in $\delta^{18}O$ in Pacific mollusks (Teranes et al. 1996) indicate a shift from a permanent El Niño–like state in the Pliocene with less variability than today, to present-day ENSO variability (Molnar 2008). On the contrary, spectral analysis of $\delta^{18}O$ SST and salinity proxy records from corals in the Philippines indicate Pliocene ENSO variability similar to present-day (Fig. 1.3a-c; Watanabe et al. 2011). Sediment records suggest a lowering of the Indonesian Throughflow (ITF) between 5-3 Ma (Srinivasan and Sinha 1998), possibly from tectonic movements within the Archipelago restricting the throughflow (Kuhnt et al. 2004) or the presence of the CAS rerouting upwelled Pacific water through the CAS rather than the ITF (Schneider and Schmittner 2006).

Proxy evidence indicates a change from high to low productive species in the North Atlantic around the time of the estimated CAS final closure (Bartoli et al. 2005). In the EEP, the effect of increased upwelling and restriction of nutrient-rich Pacific waters through the CAS significantly increased nutrient concentrations. Proxy records show an increase and eastward shift in mass accumulation rates of calcite (Lyle 2003) and opal (Farrell et al. 1995) towards South America (80º-90ºW) ~6 Ma, and decreases in ^{13}C from benthic foraminifera in this region ~3 Ma (Mix et al. 1995). Proxy record evidence also points to a massive drop in opal accumulation rates in the North Pacific ~2.75 Ma and has been inferred as a decrease in marine NPP associated with a strong halocline and increased stratification after the CAS final closure (Haug et al. 1999). Furthermore, Haug and Tiedemann (1998) showed that the carbonate sand-fraction mass accumulation rates from the Caribbean and EEP began to diverge around 4.6 Ma (Fig. 1.4) with increased carbonate preservation in the Caribbean.

Overall, proxy records suggest that global ocean physical and biogeochemical characteristics, climate mean state and interannual variability, and marine nutrients and productivity were significantly different before and after the Pliocene, and the gradual shoaling and closure of the CAS during the Pliocene is hypothesized to have contributed significantly to these shifting patterns.

1.4 Relevant Idealized CAS Climate Models

The presence of the CAS permitted inter-basin exchange of water and its physical and biogeochemical characteristics between the Atlantic and Pacific Oceans, and the

large-scale ocean circulation, climate, and ocean biogeochemistry is noticeably different in climate models with an open and closed (i.e., preindustrial or modern) CAS (Table 1.2). Climate models simulate a net transport of relatively fresh and cool Pacific water into the North Atlantic through the CAS which decreases SSS in the Caribbean and Atlantic Ocean by 0.5-3 psu, and either shuts-down (Maier-Reimer et al. 1990; Mikolajewicz et al. 1993; Mikolajewicz and Crowley 1997; Murdock et al. 1997) or weakens (Nisancioglu et al. 2003; Klocker et al. 2005; Schneider and Schmittner 2006; Steph et al. 2006; Lunt et al. 2008; Steph et al. 2010; Butzin et al. 2011; Zhang et al. 2012; Yang et al. 2013) the AMOC. Net transport through the CAS is generally from the Pacific to the Atlantic, driven by the sea surface height gradient across the seaway, with a large range in magnitude (5-20 Sv; 1 Sv = 1 x 10^6 m^3 s^{-1}). Simulated net mass transport through the CAS increases from 5-10 Sv as the sill depth increases from 130 m to 700 m, and model parameterized ocean vertical diffusivity increases; 5-10.6 Sv net transport for low diffusivity values (0.3-1.3 cm^2 s^{-1}) and 7-16 Sv for high diffusivity values (0.6-1.6 cm^2 s^{-1}; Schneider and Schmittner 2006). Only a few models simulate net transport from the Atlantic to the Pacific which only occurred with a deeper sill (2559-2700 m; Nisancioglu et al. 2003; Motoi et al. 2005) and this Atlantic to Pacific net transport reversed as the sill shoaled above 1000 m, or the approximate depth of NADW (Nisancioglu et al. 2003). Motoi et al. (2005) found that the influx of relatively saline and warm Atlantic water through the relatively deeper CAS sill led to deep water formation and SAT warming of ~2.5 $^{\circ}$C in the North Pacific. "Island rule" and the quasi-island approaches (Godfrey 1989; Nof 2000, 2002) are analytical methods based on the integrated momentum equations used to determine the direction of flow around islands

(i.e., South America in the case of a CAS). In contrast to results from most CAS climate models, Nof and Van Gorder (2003) calculate net mass transport from the Atlantic to Pacific through the CAS based on the assumption that NADW is not present. However, when they include 20 Sv of NADW, similar to present-day estimates, they calculate CAS transport from the Pacific to Atlantic similar to most climate models. Proxy records also support a seasonal cycle of mass transport through the CAS, such as larger CAS transport in boreal summer and smaller CAS transport in boreal winter (Steph et al. 2006).

In general, AMOC weakening (~2-12 Sv; Zhang et al. 2012) in response to the presence of the CAS reduces northward ocean heat transport (OHT) ~14-33% from the tropics to the NH high latitudes and increases OHT ~13-25% to the Southern Hemisphere (SH) high latitudes. These changes in OHT with the CAS result in ~2-6 $^{\circ}$C SST cooling in the North Atlantic and ~2-3 $^{\circ}$C SST warming in the South Atlantic. This asymmetrical, bipolar SST response to the addition of a CAS results from sufficient zonal transport of SAT anomalies in coupled models (Lunt et al. 2008), and leads to cooler SATs in the NH, with reduced evaporation and precipitation, warmer SATs in the SH, and 0.2-0.28°C global mean SAT cooling (Lunt et al. 2008; Fedorov et al. 2013; Yang et al. 2013). The Intertropical Convergence Zone (ITCZ) shifts south towards the warmer SH (Steph et al. 2006; Lunt et al. 2008; Steph et al. 2010; Fedorov et al. 2013; Yang et al. 2013) from wind anomalies over the equatorial Pacific (Broccoli et al. 2006). Prange and Schulz (2004) found that changes in cross-equatorial ocean heat transports with the addition of a CAS affected the strength of the subtropical high pressure systems and the magnitude of trade winds, ceasing the "upwelling see-saw" – intensified upwelling along the southwest African coast and weakened upwelling along the northwest African coast – found with

the closed or modern CAS topography. Climate models have disputed the "Panama Hypothesis" (Lunt et al. 2008) or the direct role of the CAS on the initiation of NHG, and simulate only slight changes in perennial snow cover in the NH (Klocker et al. 2005), no change in the Greenland ice sheet extent (Schneider and Schmittner 2006), and only very small differences in ice sheet volume (Lunt et al. 2008). To find the mechanism(s) contributing to the unexplained warmth of the early Pliocene and resolve the "Pliocene paradox" – whether present-day climate and that of the early Pliocene are two different states in response to the same external forcing (e.g., atmosphere pCO_2 concentrations, solar) – Fedorov et al. (2013) considered the open CAS as a possible candidate. However, using an Earth System Model (ESM) with 3.0° x 3.0° horizontal spatial resolution (increasing to 1.0° x 1.0° at the equator) in the ocean component and prescribed/static preindustrial vegetation, they were unable to explain all of the climate patterns of early Pliocene warmth with an open CAS.

With the open CAS, the tropical Pacific zonal SST gradient decreases and the thermocline deepens in the EEP (Fedorov et al. 2006; Steph et al. 2010; Zhang et al. 2012; Fedorov et al. 2013), consistent with paleoclimate proxy records. Several mechanisms have been attributed to the AMOC weakening and EEP thermocline deepening from climate models, such as the absence of NHG (Fedorov et al. 2006) or the addition of the CAS (Steph et al. 2010), both reducing buoyancy in the North Atlantic. Twelve climate models related AMOC weakening (from global ocean reorganization with the addition of the CAS) to thermocline deepening in the EEP, and the response was amplified by wind-stress feedbacks included in the coupled climate models (Zhang et al. 2012). With an open CAS, climate models simulate an increase in ENSO amplitude and

weakening of the annual cycle of tropical Pacific SSTs (Song et al. 2017). Relative to present day, Scroxton et al. (2011) combined stable isotope proxy records with a coupled model simulation of the Pliocene and found a simulated Pliocene mean climate similar to observed present-day mean climate with more periodic and regular amplitude ENSO variability (Fig. 1.3d-e) than present-day and a deeper Pliocene thermocline attributed to warmer equatorial undercurrents and reduced upwelling. Similarly, Haywood et al. (2007) found persistent Pliocene ENSO variability similar to present-day ENSO variability in a climate model forced with Pliocene boundary conditions. Climate models show that an increase in the tropical Pacific east-west SST gradient from 1°C to 6°C increases ENSO amplitude by 30-40% (Manucharyan and Fedorov 2014) and 15-20% (Song et al. 2017). They also indicate a reduction by half in the intensification of the annual cycle from the weakening of the meridional wind stress with the open CAS (Song et al. 2017). In fact, when the ITF is closed and there is no net mass transport, interannual variability is intensified with more frequent warm events (El Niño) throughout the tropical Indo-Pacific domain (Song et al. 2007). The presence of the CAS rerouted upwelled Pacific water through the CAS rather than through the Indonesian Archipelago, decreasing net mass transport through the ITF from 20-24 Sv (Schneider and Schmittner 2006) and 13.5 Sv (Yang et al. 2013) when the CAS is closed, to 8-7 Sv (Schneider and Schmittner 2006) and 2.6 Sv (Yang et al. 2013) when the CAS is open. Therefore, the presence of the CAS may have increased interannual variability in the Indo-Pacific through decreased throughflow in the Indonesian Archipelago.

To my knowledge, the only published climate simulation that examined the role of the seaway on ocean ecosystems is that of Schneider and Schmittner (2006). They used a

relatively coarse spatial resolution (1.8º x 3.6º) ocean ecosystem model coupled to an energy balance model atmosphere to show that the weakened AMOC with the addition of the CAS increased ocean mixing time and decreased upwelling, leading to a decrease of 20-25% in globally integrated NPP. They found that surface nutrient concentrations increased in the North Atlantic and Arctic Ocean by 30-50% from the advection of nutrient-rich subsurface Pacific water into the Atlantic through the CAS. However, they were not able to simulate an increase in North Pacific NPP with the open CAS as inferred from the opal accumulation rate changes (Haug et al. 1999) previously discussed (Section 1.3). They attribute decreased nutrient concentrations in the bottom water of Panama Basin in the EEP to processes that remove ^{13}C depleted material from the sea floor, such as the reduction of nutrients due to the presence of the CAS transporting nutrients out of the region, or the decreased flux of organic material. They hypothesize that the three-fold decrease in NPP in the EEP, and the associated reduction in the sinking and remineralization of organic matter, would lead to weakening of OMZs and reduced denitrification – bacterial reduction of nitrate (NO_3^-) in the near-absence of oxygen in the sediments and water column.

In summary, climate models generally simulate the influx of relatively fresh Pacific water through the open CAS into the North Atlantic, decreased SSS in the Caribbean, weakened AMOC, decreased poleward OHT in the NH, and increased poleward OHT in the SH. The bipolar temperature response leads to a global mean SAT cooling and southward shift of the ITCZ. The AMOC weakening deepened the tropical Pacific thermocline and ENSO variability was similar to or more periodic than present-day ENSO variability. The AMOC weakening with the addition of the CAS increased the

ocean mixing time and decreased upwelling, resulting in a 20-25% decrease in globally integrated NPP. The advection of nutrient-rich subsurface Pacific water into the Atlantic with the open CAS increased surface nutrient concentrations in the North Atlantic and Arctic Ocean 30-50%, and decreased productivity by three-fold in the EEP.

1.5 Dissertation Overview

The balance of Pliocene paleoclimate proxy indicators (Table 1.1) and climate models (Table 1.2) suggests that there were major changes in ocean circulation, climate, and marine biogeochemistry before and after the CAS final closure, but there remains uncertainty in the role of the seaway on the coupled Earth system. While climate models have simulated the seaway shoaling by changing the seaway widths and sill depths, model limitations prevent the simulation of a very narrow, single grid point wide seaway, or the very late stages of shoaling. Divergence in interpretations of available paleoclimate proxy indicators previously discussed (Section 1.3) may represent different stages in the evolution of the CAS, including the late stages of CAS shoaling. The AMOC weakening with the CAS is attributed to changes in buoyancy from decreased SSS in the North Atlantic with a large range in values (0.5-3.0 psu). Furthermore, diversity in the magnitude of AMOC responses (~2-12 Sv; Zhang et al. 2012) with the open CAS among the models have been attributed to varying ocean model parameterizations, such as ocean diffusivity (Schneider and Schmittner 2006), and wind-stress feedbacks (Zhang et al. 2012). Also, how different water properties from the seaway shoaling affect the spatial pattern of deep-water circulation and the identification of the mechanisms driving the

changes in the tropics to changes in high latitude deep water remains unclear. Overall, Pliocene proxy records and climate models show that the open CAS may influence climate mean state, such as tropical Pacific SSTs and thermocline structure, although there is little consensus on the magnitude, direction, or mechanisms. Likewise, there remains little consensus on the impact of the presence of the CAS and its shoaling on ENSO variability either from paleoclimate proxies or climate models. While the primary focus of climate models has been on the physical climate response to the open CAS, very little is known about how the CAS impacted ocean biogeochemistry (especially in the CAS region), global marine nutrients and NPP, and atmosphere pCO_2 concentrations on short time scales – relative to geological time scales or < 500 kyr (Walker et al. 1981; Toggweiler 2008). It has not been determined if the massive decrease in opal accumulation rates from paleoclimate proxy indicators (Haug et al. 1999) is a result of the CAS closure or lower sea level following NHG around the same time which restricted the transport of fresh North Pacific water into the Arctic via the Bering Strait and increased North Pacific stratification. Did the CAS shoaling contribute to the diverging patterns of carbonate preservation in the Central American region in the paleoclimate proxy records (Haug and Tiedemann 1998)? To my knowledge, climate models to date have not been able to answer this question since it requires a coupled, interactive global carbon cycle and an acceleration of the long time scales associated with surface sediment $CaCO_3$ long-term burial.

To address these gaps in the state of the science regarding the role of the CAS on the Earth system, the primary research objectives of this dissertation are: (1) to configure a state-of-the-art ESM with documented realistic representation of preindustrial climate,

interannual tropical Pacific variability, and marine biogeochemistry to simulate the evolution of the CAS for multi-millennial time-scale simulations, (2) to determine the mechanistic role of the open CAS and its evolution on global ocean circulation including deep-ocean water mass characteristics and circulation, (3) to evaluate the response of the open CAS and its evolution on mean climate state, especially the SH extratropics and tropical Pacific, (4) to examine the sensitivity of the open CAS and its evolution on interannual climate variability including ENSO, (5) to analyze the quasi-equilibrium biogeochemical impacts with the open CAS and determine the short time-scale (<500 kyr) response in atmosphere pCO_2 concentrations, and (6) to reconcile the available paleoclimate proxy indicators with the ESM results to support my hypothesis that the open CAS contributed to large-scale changes in global ocean circulation, climate, and marine biogeochemistry, and made a significant (~1K) contribution to Pliocene climate warmth.

To achieve these goals, I performed idealized open/closed CAS multi-millennial simulations with a state-of-the-art Geophysical Fluid Dynamics Laboratory (GFDL) ESM, GFDL-ESM2G (Dunne et al. 2012b, 2013; Section 2.1 and Section 2.2), that includes a coupled, interactive carbon cycle and ocean biogeochemical component, and used GFDL-ESM2G output to drive a $CaCO_3$ box model (Dunne et al. 2012a) for examining long-term (e.g., associated with the ~100 kyr time scale of calcite compensation) $CaCO_3$ burial and atmospheric pCO_2 impacts. The evolution of the seaway is simulated via different model bathymetry to represent early to late seaway shoaling stages (Section 2.3). There are several aspects of this model and experiment design that make it novel and provide a realistic representation of the CAS, to my

knowledge. First, these are the first CAS idealized simulations that use an ESM with relatively *higher spatial resolution* in the ocean component (⅓° at the equator increasing to 1° at the poles) capable of resolving relatively small spatial-scale processes compared to climate models (Table 1.2). Second, the horizontal grid discretization allows for the simulation of a very narrow, *single-point channel* to represent the late stages of CAS closure without significant regional alteration of topography or land-sea mask. Third, the simulated ocean biogeochemistry in response to the open CAS is accelerated via an offline $CaCO_3$ box model to examine the *response in the surface sediment* $CaCO_3$ *long-term burial* for comparison with paleoclimate proxy indicators. Finally, the use of this ESM allows for the study of the open CAS's *direct impact on atmospheric* pCO_2 *concentrations*. GFDL-ESM2G has a highly skillful representation of ENSO (Wittenberg et al. 2006; Guilyardi et al. 2006) among Coupled Model Intercomparison Project version 5 (CMIP5; Taylor et al. 2012) models in the same class (Guilyardi et al. 2012), and is a good model to use for examining the role of the CAS on ENSO variability. Chapter 2 provides a description of the relevant physics, biogeochemistry, strengths and biases in GFDL-ESM2G, and the idealized CAS experiment configurations. In Chapter 3, I present model results of changes in global circulation influencing inter-basin mass, heat and salt transport, ocean physical mean state, and large-scale deep-ocean circulation, and comparison with proxy records. Chapter 4 includes model results of the sensitivity of the global, tropical, and SH mean climate, and interannual tropical Pacific variability to the addition of the CAS, and comparison with proxy records. In Chapter 5, model results of the open CAS impact on ocean ventilation, nutrients, NPP, carbonate chemistry, and atmosphere pCO_2 implications, and comparison with proxy records are presented.

Chapter 6 summarizes the dissertation, including implications and concluding remarks.

Chapter 2

Experiment Design

2.1 GFDL-ESM2G Description and $CaCO_3$ Long-Term Burial

GFDL-ESM2G, documented by Dunne et al. (2012b, 2013), is a state-of-the-art ESM without flux adjustments that participated in CMIP5. The atmosphere component, AM2 (Anderson et al. 2004), uses a 2˚ latitude x 2.5˚ longitude horizontal grid and 24 vertical levels and is similar to the component used the in the Climate Model version 2.1 (GFDL-CM2.1; Delworth et al. 2006). The sea ice component (SIS; Winton 2000) is also very similar to the sea ice component in GFDL-CM2.1 and incorporates full ice dynamics, three-layer thermodynamics, five different ice thickness categories plus open water, and sea ice diffusion for narrow, one meridional grid point-wide channels on a tripolar grid. The land model (LM3.0; Milly et al. 2014) exchanges water, energy and CO_2 between the land and atmosphere, and includes interactive, dynamic vegetation capable of simulating ecosystem dynamics in response to climate (LM3V; Shevliakova et al. 2009). The atmosphere CO_2 tracer was restored annually and globally to the preindustrial reference value of 286 ppmv allowing realistic diurnal and seasonal CO_2 variability over land and reduced atmosphere CO_2 drift during the model spin-up.

The isopycnal vertical coordinate-based ocean component, Generalized Ocean Layer Dynamics (GOLD; Hallberg 1995), uses a 1˚ horizontal grid increasing to ⅓˚ meridionally at the equator, tripolar above 65˚N, and 63 vertical levels, including two

mixed layers (Hallberg 2003; Thompson et al. 2003), two buffer layers, and 59 interior layers. To my knowledge, the ocean component in climate models simulating the open Central American Seaway (CAS) had relatively coarse resolution compared to GFDL-ESM2G and may not have resolved many small-scale processes that affect the horizontal and vertical circulation with a seaway important for realistic climate simulations (Table 1.2), such as the baroclinic (Rossby radius) scale which is about 1˚ near the equator and smaller at high latitudes or the Equatorial Undercurrent near the Central American region, both of which impact tropical Pacific climate. For example, baroclinic wave guide properties and, thereby, Rossby and Kelvin waves, exert a substantial influence on thermocline depth and SSTs (Moore and Philander 1977; Cane and Sarachik 1979). The model uses the areal depth average of high-resolution bathymetry with the full sill depth, represents explicit exchanges across 14 straits, and provides a reasonable resolution across the narrow density and broad dense-to-light water structures. To avoid excessively deep mixed layer depths (Hallberg 2003), sub-mesoscale eddy-driven restratification of the mixed layer is parameterized after Fox-Kemper et al. (2011), and a diapycnal mixing scheme (Hallberg 2000) is used to ensure water mass structure preservation. The background diapycnal diffusivity (K_d) described in Harrison and Hallberg (2008) is 2 x 10^{-6} m^2 s^{-1} at the equator and increases to 2 x 10^{-5} m^2 s^{-1} at 30˚N, representing realistic spatial dependence of global ocean vertical mixing, a model-dependent parameterization that ocean overturning is particularly sensitive to in climate model simulations with an open CAS (Schneider and Schmittner 2006).

The ocean biogeochemical and ecological component is Tracers of Ocean Phytoplankton with Allometric Zooplankton code version 2.0 (TOPAZ2; Dunne et al.

2010; Henson et al. 2009) with 30 tracers representing various biogeochemical cycles (e.g., carbon, nitrogen, phosphorus, alkalinity, iron, and surface sediment $CaCO_3$ (Dunne et al. 2012a). Carbon is cycled through the atmosphere, ocean, and land in GFDL-ESM2G, while alkalinity, dissolved inorganic carbon (DIC), and nitrate (NO_3^-) have external sources and sinks that allow these ocean inventories to change while the other tracers do not. TOPAZ2 includes three explicit phytoplankton groups with modified growth physiology (Geider et al. 1997), a size-based relationship of production and loss (Dunne et al. 2005), and diazotroph (nitrogen fixers) CO_2:NO_3^-:O_2 stoichiometry of 106:16:150 (Anderson 1995). CO_2 gas exchange follows Najjar and Orr (1998). NO_3^-, phosphate (PO_4^{3-}), silicate, and oxygen (O_2) are initialized from World Ocean Atlas 2005 observations (Garcia et al. 2006a, 2006b; Collier and Durack 2006), and alkalinity and DIC are initialized from the Global Ocean Data Analysis Project (Key et al. 2004). Negative O_2 in TOPAZ2 represents an accumulation of respiration deficit in the absence of NO_3^- and O_2. External inputs in TOPAZ2 include soluble iron (Fe; Fan et al. 2006) and river nitrogen (Seitzinger et al. 2005). River inputs of DIC, alkalinity, and lithogenic material balance present-day burial of $CaCO_3$ and lithogenic material (Dunne et al. 2007) with the runoff fluxes calculated every time step to allow for variability in fluxes associated with fixed DIC, alkalinity and NO_3^- concentrations.

Sediment $CaCO_3$ initial conditions are supplied by bottom water conditions and fluxes from the Dunne et al. (2012a) $CaCO_3$ box model optimized to accelerate the long-term surface sediment $CaCO_3$ burial. Since the time scales of bottom water sediment $CaCO_3$ burial are very long (~100 kyr), GFDL-ESM2G output, such as CO_3^{2-} concentration, $CaCO_3$ saturation state, and surface sediment $CaCO_3$ burial fluxes, were

used to drive the offline $CaCO_3$ box model (Dunne et al. 2012a) to obtain surface sediment $CaCO_3$ long-term (<500 kyr) burial flux estimates for the CAS idealized experiments.

This model was chosen in part for its horizontal grid discretization capability to simulate realistic flows through very narrow channels (Hallberg 1995), an important characteristic in simulating the flow through the seaway as it is constricted to a narrow, 109-km width channel. The ability of GFDL-ESM2G to simulate flow through a single grid-point-wide meridional channel accommodating the representation of unidirectional flow is a key feature unique to this particular ESM at GFDL and cannot be achieved with the current GFDL-ESM2M model which uses a slightly different ocean formulation, or climate models simulating the open CAS to date (Table 1.2), to my knowledge, and allows the narrow seaway experimental design to be possible. GFDL-ESM2G was also chosen for this experimental design for its relatively high spatial resolution in the ocean component compared to the ocean component spatial resolution in climate models simulating the open CAS (Table 1.2), its realistic representation of preindustrial climate, especially ENSO, compared to various observational estimates (Section 2.2), and its coupled, interactive carbon cycle allowing for the simulation of the changes in deep ocean carbon sequestration and atmosphere pCO_2 impacts associated with an open CAS.

2.2 GFDL-ESM2G Strengths and Biases

Dunne et al. (2012b, 2013) evaluated and documented GFDL-ESM2G's strengths and biases in the CMIP5 preindustrial 1860 control simulation, and the relevant

characteristics for this dissertation are summarized. NADW formation and circulation is characterized by realistic southward NADW flow and agrees well with observationally based estimates (Talley 2003; Ganachaud and Wunsch 2003) for the streamfunction depth scale (Dunne et al. 2012b). There is a high salinity and warm bias from strong deep Pacific ventilation (16 Sv) and the maximum overturning (22 Sv at 24°N) is higher and shallower than observationally based estimates (17.2-19.8 Sv; Talley 2003; Ganachaud and Wunsch 2003). In the Atlantic, Antarctic Bottom Water (AABW) upwells to a depth of ~3 km before flowing southward out of the basin. The ventilation/flushing time scales, as determined by the ideal age tracer in the model, compares well with radiocarbon-based estimates (Krasting et al. 2016). Globally, GFDL-ESM2G agrees well with observational estimates of OHT (Dunne et al. 2012b). Atlantic meridional OHT at 26.5°N (1.14 PW) is within the range of estimates from the Rapid Climate Change program, RAPID (1.33 ± 0.40 PW; Johns et al. 2011).

GFDL-ESM2G simulated SST patterns are comparable ($r^2 = 0.98$) to present-day observations (Locarnini et al. 2006), with biases similar to those in GFDL-CM2.1 and other models in that class (Delworth et al. 2006; Wittenberg et al. 2006; Randall et al. 2007, supporting material; Richter et al. 2012; Dunne et al. 2012b). These biases include a cold bias partly due to an interior cold drift in the model that persists over the long, millennial time-scale spin-up and the 1860 radiative initialization technique (Stouffer et al. 2004), too cold subpolar North Pacific, too warm Southern Ocean, equatorial Pacific cold bias (~1-2 ˚C in the WPWP), and general eastern boundary warm biases (Dunne et al. 2012b) – all common biases among climate models to varying degrees (Griffies et al. 2009). The global thermocline volume (> 8˚C) in the model (131 x 10^{15} m^3) is

comparable to present-day observations (137 x 10^{15} m^3) after accounting for the 0.5˚C warming over the historical period (Levitus et al. 2005), but on the shallow end with less ventilation (Dunne et al. 2012b). The preindustrial control simulation agrees well with present-day observations for top-of-the-atmosphere shortwave albedos, except for local biases in the eastern tropical ocean basins from too little low cloud cover, and the south equatorial Pacific region from too little downward radiation from the common "double ITCZ" problem (Lin 2007; Dunne et al. 2012b). Generally, GFDL-ESM2G reproduces present-day observed precipitation patterns, with a dry bias and low variability in the central equatorial Pacific and the common "dry Amazon" problem (Delworth et al. 2006). The simulated sea ice extent agrees fairly well with 1979-2000 observations from the National Snow and Ice Data Center (Fetterer et al. 2009), but has too much (little) sea ice extent in the NH (SH) winters compared to observations because of the cold NH/warm SH model bias previously discussed (Dunne et al. 2012b).

GFDL-ESM2G simulates a broad spectrum of ENSO variability in agreement with observations for the Niño-3 region (5˚S-5˚N, 150˚-90˚W) with multi-decadal variations in amplitude and frequency, but has slightly weak ENSO variability with little variance in the interannual band relative to the seasonal cycle, and a preference toward cool events, or La Niñas, versus warm events, or El Niños (Dunne et al. 2012b; Fig. 4.8a, right). The strong west Pacific SST gradient in GFDL-ESM2G prevents the eastward spread of convection over Indonesia during El Niño (Dunne et al. 2012b), thus weakening the Bjerknes feedback (the coupling between SST and wind response; Bjerknes 1969), shortening the time for the equatorial thermocline adjustment to the wind anomalies (Kirtman 1997; Wittenberg 2002; Capotondi et al. 2006), and weakening and

shortening the period of El Niño (Dunne et al. 2012b). The strong thermal stratification in the subsurface EEP SST leads to a relatively strong seasonal cycle of Niño-3 SST (Dunne et al. 2012b). Despite these biases in the amplitude and phasing of ENSO, the global atmospheric response (i.e. teleconnections) to SST variability in the tropical Pacific compares well with present-day observations.

In general, the model agrees well with estimates of carbon partitioning between various reservoirs, with ocean biota lower than the observational synthesis and box model analysis (Siegenthaler and Sarmiento 1993), and DIC biases in deep ocean spatial patterns stemming from overly strong Antarctic Bottom Water propagation into the IndoPacific (Sallée et al. 2013). Global mean ocean primary productivity, or NPP, is 68 PgC a^{-1} and within the range of global productivity estimates from comparative analysis (36-78 PgC a^{-1}; Carr et al. 2006) with high productivity regions restricted to ventilation sites. Surface sediment $CaCO_3$ storage is 469 PgC, gaining 0.12 PgC a^{-1} as steady-state is not yet achieved in the long, millennial time-scale preindustrial control simulation due to the long time scales associated with surface sediment $CaCO_3$ deep water burial previously discussed, and is the motivation for using the box model for $CaCO_3$ long-term burial. More than half of the spatial ΔpCO_2 variability is captured by the model, with high biases in the northern and western equatorial Pacific upwelling regions and the Southern Ocean, and low biases in the northwest Pacific (~40°N). Overall, surface nutrients (e.g., NO_3^-, PO_4^{3-}) are represented well in the model, except for a long time-scale NO_3^- inventory loss from the overexpression of tropical eastern Pacific pelagic suboxia which is a common bias in this class of models (Najjar et al. 2007). Most of the regional surface NO_3^- variability is captured (r^2=0.91) but low biases occur in the

subpolar North Pacific and Southern Ocean. Simulated surface PO_4^{3-} patterns agree well with observations (r^2=0.87), while the ocean interior (500 m) has a positive global average bias (0.31μM, r^2=0.64 compared to observations). In the interior, the model captures 69% of the spatial variation of O_2 at 500m, including the lack of O_2 ventilation in the North Pacific in observational estimates, and has a negative global average bias of -32 μM.

On the whole, GFDL-ESM2G's framework (e.g., ocean component spatial resolution, vertical diffusion, horizontal grid discretization) addresses deficiencies in climate models used to simulate the open CAS (Table 1.2), realistically represents preindustrial climate compared to present-day observations, and achieves similar fidelity to the well-documented, state-of-the-art GFDL-CM2.1 model (Delworth et al. 2006) to allow meaningful perturbation studies (Dunne et al. 2012b; Dunne et al. 2013).

2.3 GFDL-ESM2G CAS Idealized Experiments

There is considerable uncertainty in the paleoclimate record regarding the exact details and timing of the CAS shoaling and closure (Section 1.2), and of the climate of the Pliocene. Rather than simulating the realistic comprehensive suite of changes to the Earth system associated with the climate of the Pliocene, the mechanistic role of changing topography associated with the various stages of CAS closure on global ocean circulation is examined through four open/closed CAS idealized experiments (Table 2.1) with all other model forcings (e.g., continental configuration, well-mixed greenhouse

gases, aerosols, solar forcing, orbital parameters) remaining constant and unchanged from the control simulation, hereafter “CLOSED”. This experimental design is important for attribution studies since it isolates the direct impact of the addition of the CAS and its various shoaling stages on the coupled Earth system. The millennial time-scale CLOSED seaway simulation (Fig. 2.1a) is identical to the CMIP5 GFDL-ESM2G preindustrial control simulation previously characterized in Section 2.2 and documented by Dunne et al. (2012b, 2013). Three open seaway experiments were initialized from and are identical to the CLOSED experiment except for varying seaway widths and sill depths representing the various stages of seaway shoaling (Table 2.1) based on paleoclimate proxy indicators discussed in Section 1.2 and paleogeographic reconstructions.

A 109-km wide and 2000-m deep meridionally-oriented seaway was introduced near the border of Central and South America based on the peninsula model paleogeographic reconstruction of Central America for the mid-Miocene (Fig. 2.2b; Whitmore Jr. and Stewart 1965) in the “NARROW” experiment (Fig. 2.1b). This experiment represents the later stages of the CAS evolution and near-closure. The “WIDE” experiment represents the earlier stages of CAS closure with a 1308-km wide and 2000-m deep seaway (Fig. 2.1c), similar to climate model studies discussed in Section 1.4 (Fig. 2.2c). To represent the archipelago paleogeographic reconstruction in which Central America is separated by shallow straits during the mid-Miocene (Fig. 2.2a; Coates and Obando 1996) and to simulate the seaway sill shoaling, the sill depth in “WIDE” was raised to 200 m while the width remained unchanged in the fourth experiment, “WIDESHALLOW” (Fig. 2.1d). Similar to the uncertainty associated with the paleoclimate proxy indicators previously discussed (Section 1.3), the timing and

structure of the paleogeography of southern Central America during the Pliocene remains unclear (Kirby and MacFadden 2005). Thus, this experimental design allows for a sensitivity study of the role of the various stages of CAS shoaling (WIDE/early stages, NARROW/peninsula model, and WIDESHALLOW/archipelago model) on global ocean circulation, climate, and marine biogeochemistry, and provides a framework for reconciliation with available paleoclimate proxy records (Table 1.1) and comparison with climate models (Table 1.2).

Each experiment was initialized from present-day observed (World Ocean Atlas 2005) temperature (Locarnini et al. 2006) and salinity (Antonov et al. 2006), and integrated for at least an additional 1400 model years following the 1000-year preindustrial control simulation towards a "quasi-equilibrium" year 1860 climate state defined by the same comprehensive suite of quantitative metrics defined for the CMIP5 GFDL ESM "piCTRL" simulations (Dunne et al. 2012b) – including (but not limited to) net top-of-the-atmosphere radiative fluxes less than 0.5 W m^{-2}, net atmosphere-land and atmosphere-ocean fluxes less than 0.1 PgC a^{-1} on the multi-centennial average (Table 5.1 and Fig. 2.4). This integration period is longer than the global ocean flushing time scale (~1000 years) and is sufficient to allow for the deep ocean to adjust to the seaway perturbation (Fig. 2.3 and Fig. 3.12). As quasi-equilibrium for the physical climate (e.g., SAT, SST) was established, I chose the final 100 years of the 1400-year spin-up integrations, or model years 1301-1400, as my analysis period. However, the AMOC calculations (Fig. 3.12) and monthly mean ENSO variability analysis included a 500-year time-averaged period, or model years 1001-1500, to capture the long-term climate variability averaging over the strong interdecadal and intercentennial modulation in

ENSO behavior (Wittenberg 2009). Additional 500-year periods analyzed for the AMOC and ENSO analysis yielded similar results highlighting the robustness of this analysis period chosen for these metrics. Due to technical issues related to the concurrent coupling between the atmosphere and ocean, the WIDE and WIDESHALLOW experiments had to be initialized slightly differently with respect to the ocean biogeochemistry component than NARROW and CLOSED and are not fully comparable for the marine biogeochemical analysis (Chapter 5). However, provided the similar spatial patterns of ocean mean ideal age (Fig. 5.3) and nutrient/oxygen change (Section 5.3) among all the open CAS simulations suggest that these wide seaway simulations may yield similar biogeochemical results to those found in the NARROW simulation. To better quantify and understand the impact of the CAS on the Earth system, the analysis is focused on the open seaways (NARROW, WIDESHALLOW, and WIDE) minus the CLOSED seaway, or the control experiment.

Chapter 3

Seaway Impacts on Ocean Physical Mean State and Circulation

3.1 Motivation and Overview

This chapter highlights GFDL-ESM2G results of the global ocean circulation and associated changes in water mass characteristics with the addition of the Central American Seaway (CAS), and its sensitivity to the various topographical representations of the CAS shoaling (Section 2.3). A description of the large-scale, global ocean circulation pattern with the addition of the CAS is provided in Section 3.2. Section 3.3 characterizes the horizontal and vertical inter- and intra-basin water mass transport in the Central American region, and the changes in global mass, heat and salt transports with the open CAS. In Section 3.4, the impacts of these transports from the addition of the CAS on ocean mean climate (e.g., SST, density) are explored. Section 3.5 describes the global ocean overturning and traces the spatial patterns of NADW with the addition of the CAS. Discussion of these model results, comparison with paleoclimate proxy indicators (Section 1.3; Table 1.1) and CAS climate models (Section 1.4; Table 1.2) and their implications is included in Section 3.6.

3.2 Seaway Impacts on Global Ocean Circulation

The presence of the CAS, regardless of whether it is 200- or 2000-m deep, or 109-

or 1308-km wide, affects both the local ocean circulation near Central America and the global ocean circulation throughout the entire depth in the GFDL-ESM2G simulations (Fig. 3.1). As discussed earlier (Section 1.4), climate model studies support the hypothesis that the seaway permits relatively fresh and cool Pacific water to flow into the North Atlantic, affecting buoyancy by adding freshwater to the North Atlantic and weakening the AMOC. These results (Fig. 3.1b-d and Fig. 3.3) show that Antarctic Circumpolar Current (ACC) water flows northward in the South Pacific basin and joins the North Equatorial Countercurrent through the seaway and into the Caribbean, rather than joining the westward flow across the Pacific and into the Indian Ocean via the ITF as in the CLOSED simulation, or preindustrial CAS configuration (Fig. 3.1a). The Pacific water entering the Caribbean through the CAS then flows around South America and enters the South Atlantic, rather than the North Atlantic as found with climate models, and rejoins the ACC. This circulation pattern is present for all open CAS simulations, regardless of the shoaling stage. This suggests that the CAS closure blocked this southern hemisphere global ocean circulation loop. In addition, the larger width of the WIDE and WIDESHALLOW seaways allows the North Equatorial Current (NEC) to continue flowing from the Caribbean into the Pacific through the central (WIDE and WIDESHALLOW) and northern (WIDE) portions of these wide seaways near the surface, while the NARROW seaway orientation lies south of this latitude so there is no Atlantic to Pacific surface water mass transport via the NEC. In addition to this bi-directional horizontal surface water mass transport with the wide seaways, there is also a reversal in the direction of mass transport through the seaway with depth. NADW penetrates into the Pacific for the seaways with a relatively deeper sill – NARROW and

WIDE – and this inter-basin, deep-water mass exchange has implications for global changes in deep-water circulation.

3.3 Seaway Impacts on Inter-basin and Intra-basin Transport

The net horizontal mass transport shows the inter-basin water mass exchange between the Pacific and Atlantic in the CAS region (Fig. 3.4a). There is 20.5 Sv net horizontal mass transport through the NARROW seaway meridionally from the Pacific to the Caribbean through most of the seaway depth driven by the difference in sea surface height anomalies (SSH, Fig. 3.2) between the Pacific and Atlantic, where the Pacific SSH anomalies are ~.1 m higher than those in the Atlantic in the CLOSED simulation (Fig. 3.2a). The net horizontal mass transport is 23.1 and 14.1 Sv for the WIDE and WIDESHALLOW seaways, respectively, with the larger transport for the relatively deeper WIDE seaway. For the WIDE and WIDESHALLOW seaways, the bi-directional horizontal net mass transport (Fig. 3.3) extends through the entire 200-m depth of the WIDESHALLOW seaway and through the upper ~1300 m of the WIDE seaway, below which it reverses direction. This results in similar net mass transports through the NARROW and WIDE seaways despite relatively large differences in the width of the seaways (~1200 km).

The upper 10-m ocean transports only a very small amount of mass through the seaway; 1.7, 4.0, and 2.3% of the net horizontal mass transport for the NARROW, WIDESHALLOW, and WIDE seaways, respectively (Fig. 3.4a). The maximum inter-basin transport through the CAS is in the upper 10-571 m for all CAS configurations and

is largest for the WIDE seaway (15.8 Sv). Most (95%) of the WIDESHALLOW transport occurs between these levels since the sill depth is restricted to 200 m and the upper 10 m transport is relatively small. The NARROW seaway transports the most mass (8.9 Sv) in the intermediate water (571-1469 m). The reversal of inter-basin transport in the deep seaways, where NADW penetrates into the Pacific through the CAS, is evident in the deepest levels (1469-5499 m), with about 12.8% of the net mass transport in the NARROW seaway at this depth interval.

The bi-directional net horizontal mass transport characterizes both the inter-basin and intra-basin exchange with the WIDESHALLOW seaway (Fig. 3.4b). The bi-directional mass transport at depth intervals below the WIDESHALLOW sill depth of 200 m suggests that ~2 Sv is intra-basin mass exchange within the CAS box (Fig. 2.1d) used to calculate the transports. Similar to the net mass transport through the CAS, most of the inter-basin exchange is in the upper levels (10-571 m) and the transport from the Pacific into the Caribbean is about 2 times greater than the transport from the Caribbean into the Pacific with the WIDE and WIDESHALLOW seaways. Vertically integrated mass transport through all CASs is from the Pacific to the Caribbean and suggests that inter-basin heat and salt transports are fundamentally different with the addition of the CAS and its configuration.

The alteration in global ocean circulation with the open CAS described in Section 3.2 is quantified using the vertically integrated inter-basin exchanges of mass, heat, and salt (Fig. 3.5). The preindustrial CLOSED seaway configuration transports 22.3 Sv northward from the ACC in the South Pacific, with the majority (21.1 Sv) transported from the Pacific into the Indian Ocean via the ITF and 0.88 Sv transported northward into

the Arctic Ocean via the Bering Strait (Fig. 3.5a). The presence of a CAS in GFDL-ESM2G draws another 1.0-4.9 Sv of ACC water northward into the South Pacific with most of the total transport going through the CAS and towards the Caribbean, driven by the SSH anomaly difference across the CAS (Fig. 3.2), rather than through the ITF. This decreases the ITF mass transports by 82% for the WIDE and NARROW deep sill seaways and 59% for the WIDESHALLOW seaway, and reroutes 15.7-19.7 Sv of ACC water through the CAS rather than through Drake Passage. The ocean circulation with the addition of the CAS also decreases mass transport into the Arctic Ocean via the Bering Strait and southward mass transport into the North Atlantic from the Arctic by about 36 to 55%. Additionally, Pacific water rerouted through the CAS into the Caribbean increases southward mass transport in the South Atlantic by a similar magnitude as the CAS transport rejoins the eastward flowing ACC.

Opening the CAS also results in different ocean heat transports (OHTs) on a large spatial scale. The northward flowing southern sourced water from the ACC in the South Pacific is only slightly (~4 to 8%) warmer with the open CAS compared to CLOSED. However, the water warms in the tropics as it is transported through the CAS, transporting 0.73, 0.71 and 0.56 PW from the Pacific into the Caribbean for the NARROW, WIDE and WIDESHALLOW seaways, respectively (Fig. 3.5b). Northward OHT in the North Atlantic decreases by 10.6-13.3% as heat is transported southward with the open CAS into the South Atlantic. In fact, opening the CAS results in a reversal in OHT direction in the South Atlantic; from 0.53 PW northward in CLOSED, to 0.34, 0.15, and 0.36 PW southward in NARROW, WIDESHALLOW, and WIDE, respectively. This change in OHT direction with the addition of the CAS substantially warms the entire SH

ocean as the water warms in the tropics as it goes through the CAS and rejoins the ACC, thereby, making the ACC relatively warmer with the open CAS than in CLOSED, and increasing OHT in the ACC. Less heat (about half) is transported from the Pacific into the Indian Ocean through the ITF with an open CAS, probably because the reduced water mass transport through the ITF transports less heat into the Indian Ocean. The changes in water mass and salt transports represent a redistribution of these properties with the open CAS, while the changes in OHT with the open CAS are non-linear (i.e., they are influenced by additional forcing factors, such as radiative processes, in response to changes in climate with a CAS).

The vertically integrated inter-basin salt transport patterns are similar to the water mass and heat transport patterns with the open CAS (Fig. 3.5c). Instead of transporting 719.2 x 10^6 kg s^{-1} of salt through the ITF in CLOSED, the CAS permits this salt transport into the Caribbean; 705.7 x 10^6, 486.2 x 10^6, and 795.3 x 10^6 kg s^{-1} for the NARROW, WIDESHALLOW, and WIDE seaways, respectively. This results in decreased salt transports in the Indian Ocean by about 58% (WIDESHALLOW) to 82% (NARROW and WIDE). There is also decreased salt transport into the Arctic Ocean via the Bering Strait and North Atlantic by about 36% to 55% resulting in a freshening of the Arctic. With the addition of the CAS, the main pathway for salt transport is through the CAS and into the South Atlantic, where salt transports increase substantially; 720.8 x 10^6, 499.5 x 10^6, and 805.3 x10^6 kg s^{-1}, for the NARROW, WIDESHALLOW, and WIDE seaways, respectively. Thus, opening the CAS results in increased mass, salt, and heat transports in the South Atlantic compared to CLOSED.

Annual zonally integrated northward OHT decreases by ~5 to 7% at 30ºN and 8 to

21% at 30ºS with an open CAS (Table 3.1). The annual, zonally integrated northward salt transports with an open CAS are reduced by a factor of 2-8 at 30ºN and 3-27 at 30ºS (Table 3.1). While all open CAS configurations result in decreases in zonally integrated northward OHT and salt transport (Fig. 3.6), they are largest in the SH and with the WIDE and WIDESHALLOW seaways (Table 3.1). The WIDE seaway has the largest difference in northward salt transport compared to the CLOSED simulation, especially in the SH, suggesting that earlier stages of CAS closure may have had a larger impact on salt transport than later stages (Fig. 3.6b). Two regions where the open CAS increases northward salt transport are the Southern Ocean and the NH extratropics.

3.4 Seaway Impacts on Ocean Physical Mean State

The changes in ocean heat and salt transport with an added CAS affect the global mean ocean state in several important ways, only some of which are sensitive to its topographic structure. Southward OHT with the addition of the CAS leads to a meridionally asymmetric annual average SST response with a similar spatial pattern among all open CAS configurations (Fig. 3.7, left). Opening the CAS in WIDE and WIDESHALLOW results in annual average SST warming up to ~4°C in the SH and cooling up to ~3°C in the NH. The spatial pattern of SSTs in NARROW is similar, but the magnitude of changes is slightly smaller. The bipolar SST response to the presence of the CAS is asymmetric with more SH warming than NH cooling, resulting in global annual average SST warming of 0.32, 0.54, and 0.56°C for NARROW, WIDESHALLOW, and WIDE, respectively (Table 3.1). The addition of the CAS has a

strong local effect on SSTs in the Central American region, cooling both sides of the seaway up to ~2°C for all open CAS configurations and decreasing the western Caribbean-Pacific SST gradient. With the WIDE and WIDESHALLOW seaways, there is an anomalous warming region (~1°C) west of the seaway in the tropical central Pacific. Overall, the seaway transports ocean heat southward, warming the SH ocean, and is largest with the WIDE and WIDESHALLOW seaways.

The open CAS redistributes global SSS similarly and is largely independent of the various CAS configurations in the model (Fig. 3.7, right). Local to the open CAS, the inter-basin water mass transport (Section 3.3) and atmosphere hydrological response (Fig. 3.8) contribute a ~2-psu surface freshening in the western Caribbean and ~3-psu surface salinification in the Eastern Pacific. These local changes decrease and reverse the direction of the western Caribbean-Pacific salinity gradient in this region. In general, the Atlantic and Pacific Ocean basins are saltier at the surface with an open CAS, while the Arctic and North Atlantic high latitudes are fresher from the reduced salt transport. Other regions of SSS decrease include the tropical West Pacific and North Atlantic. However, the Labrador Sea, an area of deep-water formation, is ~0.6 psu saltier with a seaway. Globally averaged annual SSS is 0.43, 0.40, and 0.48 psu (or ~1%) higher in NARROW, WIDESHALLOW, and WIDE, respectively (Table 3.1). This suggests that the earlier stages of CAS closure may have a larger impact on SSS and salt transport than the later stages of CAS closure, but the largest effect is with the open CAS compared to the CLOSED seaway.

The large-scale changes in ocean heat and salinity with a CAS change the global upper (100-m) ocean density with similar spatial patterns among the various open CAS

configurations (Fig. 3.9, left). Global annual average upper ocean density increases globally with an open CAS; 0.25, 0.17, and 0.22 kg m^{-3} for NARROW, WIDESHALLOW, and WIDE, respectively (Table 3.1), and are ~2 times larger than the long-term centennial-scale variability in upper ocean density. The spatial pattern of upper ocean density with the addition of the CAS correlates more with changes in salinity (Fig. 3.9, middle) than changes in temperature (Fig. 3.9, right) on density. Therefore, the spatial pattern of upper ocean density with the addition of the CAS is more closely related to the spatial pattern of SSS with the open CAS with two exceptions; the surface cooling region to the east of the CAS in the Caribbean with upper ocean density increases despite surface freshening, and the anomalous SST warming to the west of the CAS in the tropical central Pacific Ocean with upper ocean density decreases despite increased salinity. The overall offsetting density effects from salinity imply that the impact of the open CAS on salinity is the main driver for changing upper ocean density, and the open CAS alters the vertical structure of these properties as well.

With the CAS, the annual average upper (100-m) ocean is denser in the Atlantic, Pacific, Southern and Indian Ocean basins; below this level it is less dense (Fig. 3.10, left). There is an increase in the upper ocean salinity in these basins (Fig. 3.10, middle), contributing to the increased upper ocean density despite Southern and Indian Ocean upper warming (Fig. 3.10, left). Below 100 m, the Atlantic, Pacific, Southern, and Indian Oceans freshen, contributing to reduced density along with warming in these basins that extends to the bottom. Therefore, while opening the CAS results in an increase in global annual average SSS, below 100 m the ocean freshens as the CAS redistributes ocean salinity horizontally and vertically over large spatial scales.

3.5 Seaway Impacts on Global Overturning Circulation

These physical water mass characteristics with the addition of the CAS drive only moderate changes in circulation in these simulations (Fig. 3.11). While the overall vertical and horizontal structure of the global meridional overturning circulation (MOC) is similar with and without a CAS, there are noted differences. First, the northward extent of AABW in the Atlantic originating from the southern source region is suppressed with an open CAS due to SH warming (Fig. 3.11, left). In CLOSED, AABW extends northward to ~42°N. The addition of the CAS suppresses the northern edge of AABW to ~20°N for all open CAS configurations. The depth of NADW increases by ~500 m north of 20°N at the expense of AABW and there is a slight deepening of the maximum AMOC for all open CAS configurations (Fig. 3.11, right). Overall, there is a similarly slightly stronger overturning among the various open CAS configurations; ~2 Sv or 9% stronger with the deep seaways, and ~1 Sv or 4.5% stronger with WIDESHALLOW (Fig. 3.12), in contrast to previous climate model results which found a weakening of AMOC with an open CAS (Section 1.4).

While there are only small changes to the structure of NADW, the seaway has a large impact on global water mass distributions. At a given model grid box (x), the relative contribution of NADW to AABW at Drake Passage – representing a well-mixed water mass – characterized by salinity (S) was calculated by the equation of Oppo and Fairbanks (1987):

$$\%NADW = \left(\frac{S_x - S_{AABW}}{S_{NADW} - S_{AABW}}\right) \times 100 \qquad (1)$$

where S_x is the average salinity from 1469-5499 m, S_{AABW} is the average salinity from 1469-5499 m at Drake Passage (70°W), and S_{NADW} is the average salinity from 1469-

5499 m in the North Atlantic (20°-80°N; 30°-50°W). Overall, the Indian and South Pacific Oceans become more Atlantic-like with respect to NADW salinity characteristics (i.e., increased salinity) with a CAS (Fig. 3.13) as a result of the ocean circulation and salt transport (Section 3.3). The pattern is similar among all open CAS configurations, although there are some differences. The deep seaways (NARROW and WIDE) show the invasion of NADW into the Pacific through the CAS (Fig. 3.13b and Fig. 3.13c) as indicated by the higher salinity characteristics in this region. There is an absence of NADW Pacific invasion with WIDESHALLOW since its sill depth (200 m) lies above the level of NADW (Fig. 3.13d). However, the overall spatial pattern of NADW relative contribution to AABW is similar among all open CAS configurations and suggests that there were changes in large-scale, global deep water with the presence of the CAS, regardless of the shoaling stage.

3.6 Comparison with Proxy Records, Climate Models, and Implications

Similar patterns among the various stages of CAS shoaling suggest that the evolution of the CAS did not have a large overall impact on the global ocean physical mean state and circulation until absolute closure. These results suggest that the circulation pathway established by the presence of the CAS, and not any particular CAS configuration, determined the changes in transport that drove changes in mean ocean state and deep-water circulation. These results also have important physical and biogeochemical implications for comparing model and proxy records in constraining the CAS shoaling.

These idealized experiment results are consistent with proxy records suggesting

decreased SST and SSS gradients between the Pacific and Caribbean when the CAS was present (Keigwin 1982; Maier-Reimer et al. 1990; Haug and Tiedemann 1998; Haug et al. 2001; Groeneveld et al. 2008). The model SST gradient calculated between ODP site 999 in the western Caribbean (Haug and Tiedemann 1998; Table 1.1) and ODP site 851 in the eastern Pacific (Cannariato and Ravelo 1997; Table 1.1) decreases from 2.28°C without a CAS to 0.34, 0.92, and 1.17°C with the NARROW, WIDESHALLOW, and WIDE seaways, respectively. The model SSS difference calculated between sites 999 and 851 also decreases, from 1.84 psu without a CAS to -0.28, -0.76, and -0.08 psu with the NARROW, WIDESHALLOW, and WIDE seaways, respectively. In particular, Haug et al. (2001) suggested that if due to salinity alone, the Pacific-Caribbean δ^{18}O gradient decrease of ~0.5‰ corresponds to a decrease of ~1 psu with an open CAS. My GFDL-ESM2G results at the same ODP locations in the eastern Pacific and western Caribbean show that the early stage of shoaling (i.e., WIDE) has the largest decrease in Pacific-western Caribbean SSS gradient relative to CLOSED, although these results have a lower inter-basin gradient decrease with an open CAS.

I also find a sharp Caribbean intra-basin gradient in SSS as a local response to the presence of the CAS; the western Caribbean (ODP site 999; Table 1.1) is fresher and the eastern Caribbean is saltier. This model SSS gradient response may be an underestimate given its known Atlantic high SSS bias due to tropical Atlantic inter-basin moisture export over-estimation (Harrison et al. 2014). These model results imply that the local CAS SSS response is not representative of the changes to the entire Caribbean or Atlantic basin SSS and caution should be used when inferring Pacific-Caribbean SSS gradients and changes to the gradient with the CAS shoaling from proxy records obtained from the

western Caribbean ODP sites (Table 1.1). Perhaps, at those sites the proxy records capture the local CAS response and not the changes to the entire basin. If this hypothesis holds, then our understanding of the changes in global ocean physical mean state from changes in upper water exchange inferred from proxy records is incomplete and should be verified with more extensive sampling.

In contrast to previous model results that simulate transport through the CAS into the North Atlantic and weakening the AMOC, GFDL-ESM2G simulates CAS transport into the South Atlantic and only a marginal increase (~1-2 Sv) in the AMOC. Therefore, the mechanism by which my AMOC changes is through changing deep-water circulation in the SH, rather than changing buoyancy in the NH in response to upper-water exchange between the Pacific and Atlantic, or the "Panama Closure Hypothesis" (Keigwin 1982; Haug and Tiedemann 1998). My deep-water circulation results are consistent with more recent proxy records obtained by additional South Atlantic ODP sites (Bell et al. 2015; Table 1.1) showing significant and frequently stronger deep-water circulation with a CAS (Fig. 1.1b), micropaleontological results suggesting reduced influence of southern component sourced water in the North Atlantic before 2.9 Ma (Ishman 1996), and isotope proxy records (Woodruff and Savin 1989; Raymo et al. 1990, 1992; Raymo 1997) and sediment age mass distributions (Wold et al. 1994) both suggesting strong NADW formation during the Pliocene (Section 1.3). In fact, these proxy records refute the assumption of no previous NADW formation by which Nof and Van Gorder (2003) based their "island rule" calculation of Atlantic to Pacific net mass transport through the CAS, a direction not simulated by most climate models (Section 1.4) including GFDL-ESM2G. The recent South Atlantic proxy records from Bell et al. (2015) is in contrast to

proxy records that suggest reduced deep-water formation with the CAS and are based on limited data from only the western Caribbean and deep equatorial Western Atlantic (Burton et al. 1997; Haug and Tiedemann 1998; Driscoll and Haug 1998; Billups et al. 1998; Haug et al. 2001; Frenz et al. 2006; Steph et al. 2010; Osborne et al. 2014). Again, this suggests that proxy records from those sites may not be representative of changes in the large-scale or global ocean associated with the open CAS.

There may be model-dependent factors that account for the differences between my results and previous studies using climate models, such as model physics, horizontal grid discretization, numerics, and/or ocean horizontal and vertical spatial resolution. Yang et al. (2013) used a relatively coarse resolution version of GFDL-ESM2G with a different ocean formulation (CM2Mc) and simulated changes in transport through various global transects similar to my results. Conversely, with an open CAS they found a 3.7 Sv weakening in the AMOC and no significant changes in deep-ocean circulation structure except for a slightly smaller suppression of AABW northward extent compared to my results. Any of a suite of differences between CM2Mc and ESM2G, such as ocean grid horizontal resolution (3° in CM2Mc, 1° in GFDL-ESM2G), ocean physics, parameterizations, and ocean vertical frameworks (MOM-based z-coordinate in CM2Mc, GOLD-based isopycnal vertical coordinate in GFDL-ESM2G) may contribute to the difference in the AMOC with the open CAS between my results and Yang et al. (2013). Of these various mechanisms, GFDL-ESM2G tends to maintain the density of deep water when it is formed and, thus, has much deeper and more realistic AMOC than GFDL-ESM2M and CM2Mc (Dunne et al., 2012), allowing for more AMOC to penetrate below the 2000 m sill depth.

This research highlights the need for additional model experiments with more complex and higher resolution climate models, as well as additional/improved spatial resolution proxy records in the North Pacific, South Atlantic, and Southern Ocean to better constrain the mechanisms involved in global deep-water circulation and its impact on climate. While this dissertation isolates the role of the open CAS on ocean circulation changes, other tectonic changes occurred around the time of the CAS shoaling that are not considered in this idealized experiment design. In particular, the reorganization of the Indonesian Gateway between 4 and 3 Ma changed the source waters feeding the ITF, leading to a subsurface freshening and cooling of ~4°C and thermocline shoaling in the tropical Indian Ocean (Karas et al. 2009). They suggest that tectonic changes to the Indonesian Archipelago possibly contributed to the present-day equatorial eastern Pacific cold tongue development, while Lawrence et al. (2006) suggest that the earlier CAS shoaling preconditioned the cooling. These and other such paleo-reorganizations of ocean choke points could prove intriguing foci for future work akin to this study.

Chapter 4

Sensitivity in Climate Mean State and Interannual Variability to the Seaway

4.1 Motivation and Overview

The ocean circulation with the addition of the Central American Seaway (CAS) described in Chapter 3 drives regional and global scale responses in the time-mean climate and interannual tropical Pacific (e.g., ENSO) variability in the GFDL-ESM2G simulations described in this chapter. Section 4.2 describes the response of the global and inter-hemispheric time-mean climate to the presence of the CAS and its various shoaling stages. Section 4.3 focuses on the sensitivity of the tropical ocean temperature and thermocline to the presence and varying CAS configurations. Section 4.4 examines the impact of the open CAS on various modes of interannual variability, with a primary focus on ENSO. These results and their implications are discussed and compared to paleoclimate proxy indicators (Section 1.3; Table 1.1) and CAS climate models (Section 1.4; Table 1.2) in Section 4.5.

4.2 Sensitivity in Global and Inter-hemispheric Time-Mean Climate to the Seaway

Opening the seaway in GFDL-ESM2G provided a shortcut for southern sourced ACC water in the South Pacific to flow into the South Atlantic (Fig. 3.1), thereby altering the global ocean physical mean state via direct impacts on global ocean mass, heat, and

salt transports (Fig. 3.5), and resulting in a reversal in direction (from northward to southward) of the net OHT in the South Atlantic as discussed in Chapter 3 (Fig. 3.5 and Fig. 4.1b). To maintain planetary radiative equilibrium, this results in increased northward atmospheric heat transport to compensate for the net southward OHT (Fig. 4.1b) with the addition of the CAS. There is more total (atmosphere plus ocean) heat diverging from 0-45°S and converging between 0-45°N, resulting in more heat being carried away from the tropics in the atmosphere with the open CAS and relative convergence of heat in the ocean. Therefore, opening the seaway results in a bipolar, asymmetrical SAT response with a similar spatial pattern to the SST response (Fig. 3.7) and among all the CAS shoaling stages (Fig. 4.2, left), and leads to average SH SAT warming of 0.9-1.3°C and NH cooling of 0-0.2°C (Table 4.1). The largest sensitivity of SAT to an open CAS is for the earlier stage, or WIDE seaway, where there is NH maximum cooling of ~2°C in the northwest Pacific and maximum SH warming of ~8°C near the Ross Sea (Fig. 4.2d, left). Opening the seaway leads to zonal average SAT cooling north of ~20°N and warming south of ~20°N with a maximum at ~70°S (Fig. 4.4b), resulting in a global mean SAT warming of 0.4-0.7°C with the open CAS (Table 4.1), in contrast to previous results (Section 1.4). This suggests that SAT is sensitive to the presence of a CAS - with the largest sensitivity to the WIDESHALLOW and WIDE seaways - and is not directly related to the 14.1-23.1 Sv of net water mass transport through the open CAS (Section 3.3), since the wider seaways span this range in transports (Table 2.1). The SAT sensitivity to the open CAS is non-linear as it is influenced by additional forcing factors (e.g., radiative processes) similar to the sensitivity of OHT to the open CAS (Section 3.3).

The global mean warming with addition of the CAS results in an enhanced hydrological cycle and asymmetrically impacts the strength of the zonal average near-surface (2 m) winds. Global mean precipitation rates increase slightly (~1%) with an open CAS; .02 mm day^{-1} for the NARROW and .04 mm day^{-1} for the WIDESHALLOW and WIDE seaways, compared to CLOSED (Table 4.1). The global mean precipitation rate increases for WIDESHALLOW and WIDE – where the wide seaway precipitation rates are ~2 greater than those for NARROW. The bipolar, asymmetric SAT response causes the ITCZ to shift southward slightly into the SH (Fig. 4.2, right; Fig. 4.4a) towards the warmer hemisphere (Manabe and Stouffer 1980; Broccoli et al. 2006) for all open CAS configurations and is most prominent in the Atlantic and Indian Oceans (Fig. 4.2b-d). Average precipitation rates increase in the SH and decrease in the NH (Table 4.1) consistent with the SAT response to the open seaway, and zonal average total cloud amount increases south of the equator and decreases north of the equator (Fig. 4.4c) consistent with the ITCZ shift and spatial pattern of precipitation. Despite minimal changes in NH and SH extratropical zonal average precipitation rates with the open CAS (Fig. 4.4a), extratropical zonal average total cloud amount is more sensitive to the open CAS (Fig. 4.4c). In particular, opening the CAS leads to a decrease of ~3% total cloud amount averaged over the SH extratropics (Fig. 4.4c), consistent with the region of largest SAT warming (Fig. 4.4b), reflecting the SH radiative response to the open CAS. The different spatial patterns of surface heating in response to the CAS alters the tropical east-west pressure gradient, thereby weakening the surface northeasterly trade winds and strengthening the southeasterly trade winds by ~7-10% (Fig. 4.4d), and weakening the SH westerlies by ~3-6%. The seaway also impacts local precipitation rates (Fig. 4.2,

right) through (a) regional drying around the Central American region, especially to the west of the CAS with the wider seaways, (b) a northward shift in the central tropical Pacific precipitation rate, also most prominent with the wider seaways, and (c) the South Pacific Convergence Zone northeast shift related to changes in tropical Pacific mean climate (Section 4.3) and ENSO variability (Section 4.4; Trenberth 1976).

Mean climate in the SH extratropics (30-90°S) is the region most sensitive to the open CAS, consistent with the region where the largest impacts in ocean water mass, heat, and salinity transports (Fig. 3.5) occur. Increased southward OHT with the open CAS warms the SH extratropical surface air and ocean 1.2-1.8°C and 1.3-1.9°C, respectively (Table 4.2), thereby decreasing annual average SH extratropical sea ice cover from 5.4% (CLOSED) to 1.6% (WIDE seaway; Table 4.2). In the SH extratropics, low cloud cover also decreases by 2-3% (Table 4.1) which contributes to the warming in the SH with the open CAS. However, there are no changes in middle and high clouds with the open CAS (not shown). While the SH extratropical radiative and hydrological fluxes (e.g., P-E) only have minimal changes (Fig. 3.8) with the open CAS, increased SST, reduced sea ice and reduced low clouds combine for an overall decrease in the outgoing surface shortwave flux in the SH extratropics by 2-2.6 W m^{-2} (~9-11%; Table 4.2) .

4.3 Sensitivity in Tropical Time-Mean Climate to the Seaway

Tropical (20°N-20°S) mean climate response to the evolution of the CAS is of particular interest because this is a primary region for coupled ocean-atmosphere interactions (e.g., ENSO) and has been the subject of considerable debate in the literature

(Section 1.3 and Section 1.4). Opening the CAS leads to warmer tropical SST; 0.3°C, 0.4°C, and 0.5°C, in NARROW, WIDESHALLOW, and WIDE, respectively (Table 4.3). There is also warming in the upper 300 m with the open CAS, much larger than the 2-m surface warming; 0.4°C, 0.5°C, and 0.8°C for NARROW, WIDESHALLOW, and WIDE, respectively (Table 4.3). Similar to the global mean climate response to the open CAS, the WIDE seaway results in the largest tropical surface and upper ocean warming compared to CLOSED.

The spatial pattern of tropical Pacific (20°N-20°S, 140°E-90°W) sea surface and upper ocean temperatures are sensitive to the presence of the CAS; the relatively warmer west and central Pacific warms, while the relatively cooler east Pacific cools, enhancing the zonal SST gradient (Fig. 4.5, left and middle). This temperature response appears as a dipole pattern with maximum warming in the central tropical Pacific and maximum cooling in the tropical northeast Pacific (Fig. 4.5, left and middle), with the largest response in temperature to the WIDE seaway (Fig. 4.5d, left and middle). Furthermore, this spatial pattern extends into the Niño-3 region – an area commonly used for ENSO variability analysis – and is similar for all open CAS configurations. For example, SSTs warm 0.5°C in the western and cool 0.5°C in the eastern portion of this region for the WIDE seaway relative to CLOSED (Fig. 4.5d, left). This spatial pattern also extends through the upper ocean in the Niño-3 region, although the spatial extent of the eastern cooling is limited at this depth (Fig. 4.5, middle). The mean spatial pattern of changes in precipitation and SAT in the tropical Pacific is consistent with the changes in ocean temperature with the open CAS; increased precipitation and warmer SAT in the central Pacific, and decreased precipitation and cooler SATs in the east Pacific, again most

pronounced with the WIDE seaway (Fig. 4.2). This indicates a response in the coupled ocean-atmosphere dynamics to the open CAS in the tropical Pacific, and is the motivation for using the Niño-3 region for ENSO variability analysis in this dissertation.

In the tropical Pacific, the upper ocean warming in response to the CAS deepens the average thermocline by 4.5-10% or 5-11 m (Table 4.3), as represented by the depth of the 20°C isotherm in GFDL-ESM2G. Similar to the changes in ocean temperature, the greatest thermocline deepening (11 m) occurs with the WIDE seaway, followed by WIDESHALLOW (8 m) and NARROW (5 m) (Fig. 4.5, right). While these global scale increases in thermocline depth are relatively small, they are associated with relatively large local changes (~5 to 12 times larger) in thermocline depth in the CAS region in both the tropical Pacific and Atlantic. The thermocline deepens to the west of the CAS in the Pacific and shoals to the east of the CAS in the Atlantic by ~60 m (Fig. 4.5, right). While the main changes in surface and upper ocean temperature extend into the Niño-3 region, the largest changes in thermocline depth lie north of the Niño-3 region (Fig. 4.5) within the region where the SST dipole spatial pattern appears as previously described.

In response to the addition of the CAS, changes in mean tropical Pacific ocean state alter the meridional (north-south) and zonal (east-west) SST and thermocline gradients in this region. Changes in the meridional equatorial (2°N-2°S) average Pacific SSTs across 140°E-90°W are minimal in the EEP with the wider seaways compared to CLOSED. However, all open CAS simulations are warmer at the sea surface than CLOSED in the west Pacific (Fig. 4.6a and Fig. 4.7a). This warming is consistent with reduced OHT in the ITF as water mass transport decreases through the ITF and is instead transported through the CAS into the Atlantic (Fig. 3.3 and Fig. 3.5). In the EEP, minimum SSTs for

the wider seaways are similar to CLOSED, except for a slight eastward shift from ~110°W to 105°W (Fig. 4.6a and Fig. 4.7a) from the advection of cooler surface water into this region (Fig. 4.5c-d, left; Fig. 3.7). Thus, the equatorial Pacific east-west SST gradient increases in the east predominantly with the wider seaways, but does not change very much with the NARROW seaway.

Throughout most of the equatorial Pacific (i.e., west of ~95°W), the NARROW seaway is ~1°C warmer than CLOSED (Fig. 4.6a and Fig. 4.7a). However, east of ~95°W the advection of cooler surface water in NARROW decreases SSTs to values comparable to CLOSED (Fig. 4.7a). The north-south asymmetry in zonal equatorial (2°N-2°S) Pacific SSTs at 110°W is decreased with the CAS (Fig. 4.6b and Fig. 4.7b). 0-2°N average SSTs are 0.34°C warmer in NARROW, and 0.05°C and 0.1°C colder in WIDESHALLOW and WIDE, respectively, than CLOSED (Table 4.4). 0-2°S average SSTs are warmer than CLOSED for all CAS shoaling stages; 0.46°C, 0.27°C, and 0.34°C warmer for NARROW, WIDESHALLOW, and WIDE, respectively (Fig. 4.7b). The reduced north-south asymmetry in zonal equatorial Pacific SSTs at 110°W with the CAS is consistent with the spatial pattern of changes in SSTs previously discussed (Fig. 4.5, left). The EEP annual SST cycle is driven by ocean-atmosphere interactions (Xie 1994) and the cross-equatorial SST asymmetry with the open CAS changes periodicity in the annual, semi-annual and ENSO cycles (Section 4.4).

To avoid possible biases by using the 20°C isotherm depth under different mean climates and to more dynamically represent the thermocline depth (Yang and Wang 2008), I compute the depth of the maximum vertical temperature gradient (dT/dz) for examination of the spatially averaged tropical equatorial Pacific thermocline depth.

Comparison of these two metrics for the thermocline depth yielded similar results. The thermocline deepens with the open CAS for most of the tropical equatorial (2°N-2°S average) Pacific. However, it shoals in the west Pacific in NARROW despite warmer average SSTs than CLOSED (Fig. 4.6c and Fig. 4.7c). To assess the sensitivity of the thermocline slope to the CAS, I define a thermocline slope index as the difference between the average thermocline depth in the west Pacific (140°E-155°W) and east Pacific (155-90°W) averaged from 2°N-2°S to capture the equatorial waveguide and represent the region where SSTs are sensitive to the thermocline depth from the narrow equatorial upwelling. The thermocline slope index progressively increases with the wide seaways; 58.4, and 59.8 m for WIDESHALLOW and WIDE, respectively, compared to 56.1 m for CLOSED (Table 4.4). In NARROW, the thermocline slope index decreases slightly (55.4 m) compared to CLOSED. Therefore, the thermocline gradient increase with the open CAS is sensitive to the relatively wider seaways. In the equatorial (2°N-2°S) east Pacific (specifically, 110°W), the thermocline is deeper than CLOSED for all open CASs (Fig. 4.6d and Fig. 4.7d), as *dT/dz* increases both south (0-2°S) and north (0-2°N) of the equator. In NARROW and WIDE, the north-south thermocline asymmetry is altered. The average depth of the north-south *dT/dz* difference decreases in NARROW (-3.3 m) and WIDE (-2.0 m) compared to CLOSED (zero north-south difference; Table 4.4). There is also zero north-south difference in *dT/dz* in WIDESHALLOW. These changes in north-south *dT/dz* difference in NARROW and WIDE reduce the north-south asymmetry with the addition of the seaway (i.e., the north-south *dT/dz* differences decrease relative to CLOSED). Overall, the tropical Pacific mean climate is sensitive to an open CAS and is most sensitive to the WIDE CAS, or the earlier stage of shoaling,

consistent with the sensitivity of the global mean climate, previously discussed.

4.4 Sensitivity in Interannual Climate Variability to the Seaway

In addition to a different tropical Pacific mean state, I also find differences in ENSO variability from analysis of monthly mean SST anomalies in the Niño-3 region. There is an increase in ENSO amplitude (i.e., grand maximum minus grand minimum SST anomalies) with the open CAS compared to CLOSED, and the amplitude is greatest in WIDE (Fig. 4.8; Table 4.3), suggesting that the amplitude of ENSO was largest during the relatively earlier CAS shoaling stage. The amplitude increases from 8.46°C in CLOSED, to 9.52°C, 9.07°C, and 10.55°C in NARROW, WIDESHALLOW, and WIDE, respectively (Table 4.3). Furthermore, SST anomalies are skewed (Fig. 4.8, grey lines) more toward negative values or cold events with an open CAS; -0.30°C, -0.66°C, -0.50°C, and -0.60°C, for CLOSED, NARROW, WIDESHALLOW, and WIDE, respectively (Table 4.3). This together with the ocean cooling pattern in the tropical eastern Pacific (Fig. 4.5, left and middle) suggests that there were more La Niñas, or cold events, with the open CAS compared to preindustrial interannual tropical Pacific variability.

The presence of the CAS alters the spectrum of SST variability in the Niño-3 region. The annual cycle weakens and the semi-annual (0.5-year) and interannual (2-4-year) cycles intensify with the open CAS (Fig. 4.9). This is most pronounced with the wider seaways, where the annual cycle weakens 3-fold. The intensification in the semi-annual cycle is driven by the decreased north-south asymmetry in zonal equatorial (2°N-2°S) Pacific SSTs at 110°W with the open CAS (Fig. 4.7b; Section 4.3). Similarly, there is a

decrease in the north-south thermocline gradient (2°N-2°S average at 110°W) with the open CAS (Fig. 4.7d; Section 4.3). The intensification of the interannual cycle demonstrates that the coupled ocean-atmosphere dynamics in the tropical Pacific basin are sensitive to the presence of the CAS.

The time evolution of El Niño and La Niña is also noticeably different with the open CAS. The CLOSED preindustrial simulation agrees well with the Hadley Centre Sea Ice and Sea Surface Temperature data set (Rayner et al. 2003) for the time evolution of SST anomalies zonally averaged for the region 3°N-3°S, 85°E-150°W (Fig. 4.10). Zonal averages were used for the time evolution analysis of ENSO variability to avoid influences from model spatial structure biases in the tropical Pacific discussed in Section 2.2. The magnitude of SST anomalies for the time evolution of El Niño and La Niña is larger with the open CAS, regardless of the CAS configuration, consistent with the intensification of ENSO amplitude (Fig. 4.8; Table 4.3). Furthermore, the peak in SST anomalies occurs in August - ~3 months earlier than the November peak in CLOSED - for both El Niños (warm events) and La Niñas (cold events) with the open CAS. Thus, the development of ENSO warm and cold events is a full season earlier with the open CAS. For the deeper seaways (e.g., NARROW and WIDE), strong El Niños are generally followed by strong La Niñas, a pattern that is not present with the WIDESHALLOW seaway but is consistent with the delayed oscillator theory of Suarez and Schopf (1988).

ENSO variability in the tropical Pacific causes a variety of changes in global mean climate via impacts on atmospheric teleconnection patterns. The CLOSED simulation captures the far-field impacts of ENSO variability (e.g., SAT, SST) well (Fig. 4.11b) compared to observational data and reanalysis products (Fig. 4.11a). With the open CAS,

the simulated spatial patterns are generally similar to CLOSED and observations, but the magnitudes are larger with the open CAS (Fig. 4.11). Also, there is increased spatial extent and larger magnitude of North American cooling with the open CAS. The stronger teleconnection impacts are consistent with strengthened ENSO variability with an open CAS. However, other patterns differ from CLOSED with the open CAS, such as cooling over northern Asia in NARROW and WIDE compared to warming in CLOSED and observations. There is increased spatial variability in the North Pacific in additional interannual modes, in particular, the Pacific North American Pattern, Pacific Decadal Oscillation, Northern Annual Mode, and North Atlantic Oscillation (not shown). However, there is no change in variability in the SH interannual modes (not shown). Overall, these results show that both mean climate and ENSO variability respond to the presence and shoaling of the CAS, and the resulting global teleconnection impacts may help identify key regions to sample for testing model simulations against paleoclimate proxy indicators.

4.5 Comparison with Proxy Records, Climate Models, and Implications

Global climate is sensitive to the evolution of the CAS, with the largest response to the WIDE seaway. GFDL-ESM2G is the first climate model to simulate a global mean warming (0.4-0.7°C) with an open CAS, regardless of its configuration, whereas previous climate models have simulated a global mean cooling (0.2-0.28°C). Compared to Lunt et al. (2008), who simulated a CAS configuration most similar to WIDESHALLOW, I find a global mean SAT warming of 0.7°C in WIDESHALLOW and a large bipolar SAT

response characterized by maximum SH warming of ~8°C near the Ross Sea and maximum NH cooling of ~2°C in the northwest Pacific, consistent with a response to the reorganization of the ocean circulation as described in Chapter 3 with the open CAS (Lunt et al. 2008). However, Lunt et al. (2008) simulates a global mean cooling of 0.25°C with a similar inter-hemispheric, asymmetrical response although the cooling in the NH dominates the overall mean. Their SH warming maximum was only ~3°C while their NH maximum cooling was ~7°C, much larger than GFDL-ESM2G. This is most likely because of the different mechanisms driving the climate response to the open CAS, such as GFDL-ESM2G's deep and cold AMOC and associated robust OHT to the open CAS. After ~500 integration years, Lunt et al. (2008) simulated an AMOC weakening from 20 Sv to 10 Sv attributed to reduced North Atlantic buoyancy in response to a freshening with the open CAS. In contrast, after 1400 integration years, changes in deep-water circulation in the SH drove minimal changes in AMOC (~2Sv strengthening) in GFDL-ESM2G because the heat and salt transport from the open CAS rejoined the ACC in the South Atlantic rather than the North Atlantic (Chapter 3). In addition, opening the CAS in GFDL-ESM2G results in warmer tropical water than other climate models as less heat leaves the tropics through the ITF and CAS (1.31 PW in NARROW compared to 1.34 PW in CLOSED, Fig. 3.5b), possibly due to model-to-model differences in simulating transports, especially through narrow straits such as the ITF. Furthermore, reduced SH sea ice extent in GFDL-ESM2G is consistent with recent Ross Sea and Antarctic proxy record reconstructions indicating reduced sea ice extent and duration before 3.3 Ma, after which AMOC weakening began and preconditioned the NH for continental glaciation (McKay et al. 2012). GFDL-ESM2G does not simulate ice sheets; therefore, the role of

the open CAS on NHG is outside the scope of this experimental design. While my results robustly show that global climate is sensitive to the presence and evolution of the CAS, the presence of the WIDE seaway was likely not the dominant factor influencing relatively high East African precipitation during the Pliocene as simulated by Naiman et al. (2017b).

In the tropical Pacific, proxy records suggest that the east-west SST gradient increased with the CAS closure. That is, the EEP gradually cooled from the Pliocene to present-day while the WPWP SSTs did not change much (Steph et al. 2010; Fedorov et al. 2013). My results show that the tropical Pacific east-west SST gradient decreases with the CLOSED seaway, or preindustrial, mainly from SST warming in the west Pacific from reduced OHT through the ITF with the wider seaways. The EEP minimum SSTs are similar to preindustrial but shifted eastward (~5° longitude) from the advection of cooler surface water and the bi-directional horizontal mass transport through the wider seaways. For the NARROW simulation, tropical Pacific SSTs are warmer than preindustrial but the east-west SST gradient is similar to preindustrial generally, except east of ~95°W. Fedorov et al. (2013) simulate an east-west SST gradient in the tropical Pacific similar to preindustrial with an 1100 m-deep CAS. Climate model differences between GFDL-ESM2G and their model (CESM4; Gent et al. 2011) may account for these differences, such as the relatively higher ocean spatial resolution in GFDL-ESM2G capable of resolving smaller-scale physical processes or differing model physics. The Pliocene tropical Pacific physical mean state is not well-constrained by the various proxy record reconstructions of the east-west SST gradient (Fedorov et al. 2006; Steph et al. 2010; Zhang et al. 2014). Surface temperature proxy records suffer from sparse geographical

sites leading to low spatial resolution, biases arising from seasonality and a lack of high enough temporal resolution, and the validity of assumptions in the underlying proxy methods (Masson-Delmotte et al. 2013). Recognizing these limitations, Zhang et al. (2014) used new biomarker-SST records (Fig. 1.2) and reconstructed a tropical Pacific east-west SST gradient of ~3°C that persisted throughout the Miocene (12-5.3 Ma) and increased later in the Plio-Pleistocene. Furthermore, additional proxy record sources (e.g., marine production) suggest that modern tropical Pacific conditions (e.g., EEP upwelling in the Miocene) existed earlier than the Pliocene (Kamikuri et al. 2009; LaRiviere et al. 2012). Comparison among these climate models and proxy records suggest that the CAS contributed to the increase in east-west SST gradient from the Pliocene to preindustrial.

Proxy records obtained from ODP sites (Table 1.1) for the Pliocene suggests that the tropical Pacific thermocline was deeper than present-day (Wara et al. 2005; Lawrence et al. 2006; Steph et al. 2010), consistent with the GFDL-ESM2G simulated deepening with the open CAS. Steph et al. (2010) simulated a deepening in tropical Pacific thermocline in response to both AMOC weakening with the CAS and AMOC collapse from hosing and attributed the thermocline response to AMOC weakening. GFDL-ESM2G simulates a similar spatial pattern of tropical Pacific thermocline deepening as Steph et al. (2010) but simulates a marginal strengthening (~2 Sv) in AMOC (Section 3.5) with the open CAS. This suggests that there is another mechanism(s), other than changes in AMOC associated with the open CAS, driving changes in tropical Pacific thermocline in my simulations, such as the strengthening of the westerlies in response to the southern shift in the ITCZ.

As discussed in Chapter 1, proxy records both support (Molnar and Cane 2002;

Philander and Fedorov 2003; Wara et al. 2005; Fedorov et al. 2006) and dispute (Scroxton et al. 2011; Watanabe et al. 2011) the hypothesis of a permanent El Niño-like state in the Pliocene. However, ENSO variability in the Pliocene is typically based on characteristics of El Niño inferred from proxy records and climate mean state that may also be influenced by local factors, such as precipitation and salinity. For example, Johnson et al. (2000) found that the EEP has characteristically warm SSTs, a deep thermocline, and increased salinity at depths between the mixed layer and the pycnocline during El Niño events. However, increased precipitation during El Niño tends to reduce SSS in this region (Johnson et al. 2002). Recent proxy records that suggest ENSO variability in the Pliocene was similar to present-day ENSO variability have too low sample size (e.g., 2 corals) and spatial resolution to make an accurate characterization of Pliocene ENSO variability (Watanabe et al. 2011; Fig. 1.3a-c). My results indicate increased ENSO amplitude and weakening of the annual cycle consistent with other recent climate models (Song et al. 2017), and earlier ENSO development with increased La Niña events compared to that of the preindustrial climate. Song et al. (2017) attributes the reduced tropical Pacific equatorial SST asymmetry with the open CAS to the weakening of the annual cycle during the Pliocene, consistent with my results. Furthermore, they speculate that continentality north of the equator or AMOC weakening may drive the changes in tropical Pacific equatorial SST asymmetry. Thus, ENSO variability in the Pliocene and the mechanisms that affect it remain unclear, and additional proxy records and idealized studies help to better understand tropical Pacific interannual variability in the Pliocene by demonstrating the comparative role of these processes in a single, internally consistent dynamical context.

GFDL-ESM2G and other state-of-the-art models in this class have internal model structure biases (Section 2.2). First, GFDL-ESM2G tends to favor La Niñas over El Niños in the CLOSED or preindustrial control simulation (Dunne et al. 2012b). While the increased tendency toward negative SST anomalies or La Niñas in the Niño-3 region with the open CAS may be, in part, attributed to the underlying model bias and be overestimated, it should be noted that the amplitude of ENSO variability and skewness increases with the CAS evolution from CLOSED to NARROW to WIDE. Second, given the model's relatively weak ENSO compared to observations (Fig. 4.9a, right), the enhancement of ENSO variability with the open CAS may be underestimated. Third, given the model's cold bias in the WPWP (Section 2.2), the increased tropical Pacific east-west SST gradient – driven mainly by warming in the WPWP with the open CAS – may also be underestimated. Overall, I find the sensitivity of the global and tropical climate to an open CAS increases as the seaway is gradually opened – or the transition from CLOSED to NARROW to WIDE – and the actual sensitivity may even be larger considering these internal model biases.

Comparison with climate models and proxy records highlights that the tropical climate response to the open CAS and the mechanisms driving this response are as yet unresolved. One factor to consider is the tectonic changes in the Indonesian Archipelago during the Pliocene. While the widening of the Indonesian Seaway decreases ENSO frequency (Jochum et al. 2009) and weakens ENSO strength by ~6% (Song et al. 2017), it did not have a large impact on SSTs in the eastern Pacific (Jochum et al. 2009). Another factor may be the uplift of the Andes since the late Miocene, which played a large role in orographic precipitation and contributed to southeastern tropical Pacific SST

cooling (Takahashi and Battisti 2007), increased tropical Pacific equatorial east-west SST gradient, decreased frequency of ENSO, and the number of strong El Niños (Feng and Poulsen 2014). Using two different GFDL ESMs, including GFDL-ESM2G, Naiman et al. (2017a) found that ENSO had stronger amplitude, lower frequency, and increased regularity compared to preindustrial in response to flattening the mountains globally. Perhaps, additional idealized studies considering the open CAS in conjunction with other factors such as those resolved in the present study may reveal important interactions among mechanisms driving climate change in the past and future. Rustic et al. (2015) suggest that the global warming slowdown or "hiatus" of the past ~15 years is due, in part, to the mechanisms driving cooling in the EEP, such as strengthened Pacific trade winds (England et al. 2014) and La Niña-like interannual variability (Kosaka and Xie 2013), emphasizing the need for a better understanding of the tropical Pacific mean climate and variability in past climates. My results indicate that the open CAS made a significant contribution to changes in global mean climate. The direct impact of the relatively wider seaways leads to global mean warming of 0.7°C, similar to the both the historical warming from preindustrial to present day of 0.65-1.06°C (IPCC AR5 SPM) and the additional global mean warming (0.8°C) from future projections with increased greenhouse gas emissions and resulting in a net radiative forcing of +2.6 W m^{-2} by year 2100 relative to present day (i.e., the GFDL-ESM2G CMIP5 Radiation Concentration Pathway 2.6 experiment, RCP 2.6; van Vuuren et al. 2011; Table 4.1). This demonstrates that different forcing mechanisms, either naturally forced by geologically-driven changes such as the open CAS or anthropogenically forced by human-driven changes such as elevated emissions, can result in a similar global mean climate (Table 4.1) but strikingly

different spatial fingerprints (Figs. 4.2 and 4.3). This provides a reference for improved understanding how natural and anthropogenic forcings and their underlying mechanisms drive changes in climate, and a point of caution when using paleoclimate proxy indicators as a reference for anthropogenic future changes in climate.

.

Chapter 5

Ocean Biogeochemical Impacts and Atmosphere pCO_2 Implications

5.1 Motivation and Overview

In response to the ocean circulation with the addition of the Central American Seaway (CAS) described in Chapter 3, global ocean biogeochemistry is impacted through changes in deep ocean ventilation as presented in this chapter. The ocean biogeochemical analysis focuses on comparison of the CLOSED and NARROW seaways since the wide seaways had to be initialized differently with respect to the ocean biogeochemistry (Section 2.3). Section 5.2 presents an overview of the global ocean biogeochemical impacts with the NARROW seaway. Section 5.3 focuses on the impact on macro-nutrient (e.g., NO_3^- and PO_4^{3-}) and micro-nutrient (e.g., iron) concentrations, their preformed and remineralized partitioning, and NPP. Model results and estimates of the short time-scale (< 500 kyr) global and inter-basin biogeochemical impacts are presented in Section 5.4. The NARROW seaway impacts on air-sea CO_2 fluxes and short-term atmosphere pCO_2 concentrations – in the absence of chemical weathering and volcanism – are examined in Section 5.5. Discussion of these model results, comparison with paleoclimate proxy indicators (Section 1.3; Table 1.1) and CAS climate models (Section 1.4; Table 1.2), and their implications is included in Section 5.6.

5.2 Seaway Impacts on Global Ocean Biogeochemistry

Global time series illustrate the long time scales associated with the global ocean biogeochemical response to a perturbation, in this case, the addition of the CAS, and the coupled ocean-atmosphere carbon response (Fig. 5.1). In GFLD-ESM2G, the NARROW seaway is not in equilibrium with the $CaCO_3$ in the surface sediments (Fig. 5.1g and Fig. 5.1h) because of the long equilibrium time scales (~10 kyr). Ideal age is a tracer that is set to zero at the ocean surface and accumulates with time in the ocean interior as a diagnostic of the time since surface ventilation (Thiele and Sarmiento, 1990). With a NARROW CAS, the global mean ocean is 47.7 years younger (Fig. 5.1a and Table 5.1) in response to the ocean circulation changes (Chapter 3) and this increased surface-to-deep water response time results in increased mixing with the open CAS after 1400 integration years of spin up (Table 5.1). After 3000 integration years, NARROW is ~125 years younger than CLOSED. The initial increase in ocean age with NARROW in the first ~500 years is a result of the initial, large weakening (~12 Sv) in AMOC (Fig. 3.12; Section 3.5) from the introduction of the seaway. The AMOC time series shows ~1000 year recovery time from this initial perturbation, which is consistent with the ocean age recovery time scale with the open CAS. The increased ideal ocean age in the North Pacific in NARROW reflects the changes in ventilation in this region from a reduction in Ekman transport/Sverdrup balance circulation associated with the slight southward shift of the ITCZ.

The presence of the NARROW seaway alters the ocean mixing time scale and ventilation reflected in the mixed-layer depths and the model's ocean ideal age tracer, and

has implications for changes in nutrient concentrations and productivity (Section 5.3) and carbonate chemical disequilibrium (Section 5.4). The global mean maximum mixed-layer depth, representing the deepest winter mixed layers, deepens ~6% or 2.9 m in NARROW (Table 5.1), suggesting reduced stable density stratification with an open CAS. The largest change occurs in the austral winter (e.g., July and August) when the global average mixed layer deepens by ~3 m in NARROW (Fig. 5.2a) due to decreased density stratification from the increased southward salt transport in the SH (Section 3.3). There is also a marginal (~1 m) deepening of the global average mixed-layer depth in boreal winter (e.g., January and February; Fig. 5.2a), from reduced northward OHT in the NH (Section 3.3). The largest increase in annual zonal average mixed-layer depth (~30 m) occurs in the Southern Ocean between ~60º-70ºS (Fig. 5.2b) and reflects the increased ventilation seen in the ideal age tracer (Fig. 5.3c and 5.3d) and the Atlantic meridional overturning with the closed cell near Antarctica (Fig. 3.11b, left) that arises from increased surface salinities in the Southern Ocean and indicates reduced stratification.

The spatial patterns of inter-basin (Pacific and Atlantic) differences in ocean ideal age, alkalinity, and DIC are similar with the NARROW seaway. In the preindustrial CLOSED simulation, the basin average Pacific is ~450 years older than the Atlantic (Fig. 5.3a, Table 5.3). Opening the seaway results in younger ocean ages in both basins (Table 5.3) where the influx of relatively young Atlantic water penetrates the Pacific reflected in the younger ideal age directly to west of the CAS at 2049 m (Fig. 5.3b, right), and the increased mixed layer depths in the SH and the associated ventilation changes with NARROW are reflected in younger South Atlantic water at 500 m (Fig. 5.3b, left). The mean ocean ideal age at 500 m indicates the penetration of older, Pacific water into the

Caribbean in NARROW (Fig. 5.3b, left), consistent with the net horizontal mass transports at this depth discussed in Section 3.3. The spatial patterns of ocean mean ideal age with the NARROW seaway are similar to those of WIDE and WIDESHALLOW (Figs. 5.3e-h) that are not included in this biogeochemical analysis because of the different model initialization (Section 2.3). However, the open CAS impacts ventilation and mixing (reflective in the ideal age tracer) that drives the ocean biogeochemical impacts described here, and the similar ideal age patterns among all the open CAS configurations imply that the wide seaways may have similar biogeochemical impacts as NARROW (Section 2.3).

5.3 Seaway Impacts on Global Ocean Nutrients and Primary Productivity

As discussed in Section 2.1, GFDL-ESM2G resolves an open nitrogen cycle with inputs from rivers, atmospheric deposition, and nitrogen, and losses by water column and sediment denitrification. Total global NO_3^- inventory increases by 63.1 PgN in response to changes in ocean mixing and ideal age in NARROW compared to CLOSED (442.7 PgC; Fig. 5.1b and Table 5.2). The relatively long time scales associated with NO_3^- equilibrium is reflected in the increasing trend in NARROW compared to CLOSED. At the surface (upper 100 m), global total NO_3^- concentrations are 0.22 PgN higher than CLOSED (2.92 PgN). The largest surface NO_3^- concentrations in the preindustrial control (e.g., CLOSED) are in the Southern Ocean where nutrient-rich deep waters are brought to the surface via intense mixing and upwelling (Fig. 5.4a, left). In NARROW, surface NO_3^- concentrations increase in the Southern Ocean, primarily in the extreme southern regions,

where concentrations increase up to 50% in the Weddell Sea (Fig. 5.4b, left). Other regions of increased surface NO_3^- concentrations in NARROW include the North Pacific and North Atlantic, specifically, about a doubling in the North Pacific and Greenland-Iceland-Norwegian (GIN) Seas and a three-fold increase in the Labrador Sea (Fig. 5.4b). While surface NO_3^- concentrations in the Southern Ocean increase with an open CAS, total surface NPP in this region does not change very much (Fig. 5.4b, right). Deep mixing in the high surface NO_3^- concentration regions of the Southern Ocean (e.g., 60º-70ºS), represented by the deeper mixed layer (Fig. 5.2b) and younger ideal ocean age (Fig. 5.3), and the biological pump operating at maximum efficiency relative to the supply of iron (which is fixed in GFDL-ESM2G) may contribute to the negligible changes in NPP in this region since there is no increase in productivity from dissolved iron upwelling (Fig. 5.8b). In fact, the only areas with increased total surface NPP is the Caribbean, directly east of the CAS, where productivity is approximately doubled, and also portions of the North Atlantic (Fig. 5.4b). However, these regions of increased NPP are offset by decreases elsewhere as the global total NPP decreases with an open CAS. Despite increased surface NO_3^- concentrations in the North Pacific, total surface NPP decreases (Fig. 5.4b). Globally, vertically integrated productivity from NO_3^- decreases by 3.9 PgC a^{-1} with a NARROW seaway compared to CLOSED, 72.4 PgC a^{-1} (Table 5.2). Furthermore, the introduction of a NARROW seaway in my experiments does not significantly change opal in the North Pacific, as proxy records indicate (Section 1.3).

Below 100 m, global NO_3^- inventory increases by 65 PgN in NARROW compared to CLOSED, 439.6 PgN (Table 5.2). At 2049 m, below the NARROW sill depth, NO_3^- concentrations increase the most (up to ~36 μmol kg^{-1}) in the EEP (Fig. 5.5b,

left). The EEP is a region with the lowest NO_3^- concentrations in CLOSED (Fig. 5.5a, left). There is also an increase in subsurface NO_3^- concentrations in the Atlantic (~2-6 μmol kg^{-1}) with an open CAS, although this increase is not as large as the increase in the EEP with an open CAS (Fig. 5.5b, left). The Atlantic and EEP are also regions where surface NO_3^- concentrations increase with an open CAS. At 2049 m, particulate organic nitrogen (PON) sinking flux increases mainly east of seaway in the Caribbean and in parts of the North Atlantic, with a similar spatial pattern as NPP in the upper 100 m (Fig. 5.4b, right).

Globally, total phosphorus is conserved in these simulations and vertically integrated PO_4^{3-} concentrations do not change much with a NARROW seaway (89.3 PgP) compared to CLOSED (89.2 PgP; Table 5.2). Overall, the spatial patterns of surface PO_4^{3-} concentrations are similar to the spatial patterns of surface NO_3^- at the surface, but are an an order of magnitude smaller as expected from the Redfield ratio (Fig. 5.6). The largest decrease (~0.6-1.0 μmol kg^{-1}) in surface PO_4^{3-} concentrations are in the EEP in NARROW. Similar to the decrease in productivity from NO_3^-, global total productivity from PO_4^{3-} decreases by 5.9 PgC a^{-1} in NARROW compared to CLOSED (71.2 PgC a^{-1}). The spatial pattern of NPP from PO_4^{3-} in NARROW is also similar to the spatial pattern of NPP from NO_3^- with increased productivity mainly east of the CAS in the Caribbean and North Atlantic, and decreases in the Pacific, Indian and South Atlantic (Fig. 5.7). In contrast to NO_3^- concentrations at 2049 m, PO_4^{3-} concentrations are a maximum in the EEP and the largest decreases occur in this region with an open CAS (up to ~3.2 μmol kg^{-1}). There are also increases in PO_4^{3-} concentrations in the Pacific (outside the EEP region), Indian and Southern Oceans in NARROW.

Oxygen minimum zones (OMZ), such as off the west coast of Africa and the EEP, are evident in the 200-1000 m minimum dissolved O_2 in CLOSED (Fig. 5.9a). In NARROW, there is a global increase in dissolved O_2 (Fig. 5.9b). The largest change in dissolved O_2 is in the EEP with increases up to a maximum of ~100 μmol kg^{-1}, suggesting a large reduction in the EEP OMZ with an open CAS. In general, the only decrease in dissolved O_2 is in the North Atlantic (Fig. 5.6b) with an open CAS. The Pacific dissolved O_2 inventory increases by 413 PgO_2 with the NARROW seaway compared to CLOSED (1747 PgO_2), while the Atlantic dissolved O_2 inventory decreases by 45 PgO_2 in NARROW compared to the CLOSED inventory of 1242 PgO_2 (Table 5.3). Global average dissolved O_2 concentrations increase with a CAS throughout the entire depth of the ocean (Fig. 5.10a). Opening the CAS reduces global average PO_4^{3-} concentrations down to ~2000 m, below which it increases as performed PO_4^{3-} increases (Fig. 5.10b) – the fraction that is subducted and transported (Broecker 1974; Broecker and Peng 1982; Broecker et al. 1985; Toggweiler et al. 2003; Sigman and Haug 2003). With the open CAS, vertically averaged global preformed PO_4^{3-} increases 0.14 μM from 1.74 μM in CLOSED, indicating a decrease in regenerated PO_4^{3-} from decreased global respiration consistent with the overall ocean age decrease (Fig. 5.3). Apparent oxygen utilization (AOU) is a measure used to infer changes in dissolved O_2 concentration from physical processes and respiration. By calculating AOU from the difference between dissolved O_2 at saturation (assuming 100% saturation with the overlying atmosphere; Garcia and Gordon 1992) and in situ dissolved O_2 concentrations, the changes in dissolved O_2 concentrations resulting from only the physical ocean properties (e.g., temperature, salinity) can be isolated. Global mean AOU decreases throughout the water

column with an open seaway (Fig. 5.10c). Considering nutrient stoichiometry of Anderson (1995), global total remineralized DIC (i.e., carbon organic matter and dissolution of $CaCO_3$; Schmittner et al. 2013) decreases ~32% or 241 PgC with the open seaway, consistent with a global reduction in the sequestration efficiency of the biological pump consistent with the decrease in ocean mean ideal age tracer.

5.4 Seaway Impacts on Global and Inter-basin Carbonate Chemistry

The Atlantic surface sediment $CaCO_3$ inventory decreases by 16.5 PgC in NARROW compared to CLOSED (230.9 PgC; Table 5.3), while the CLOSED Pacific surface sediment $CaCO_3$ inventory (224.4. PgC) decreases only by 5.9 PgC in NARROW after 4000 integration years (Table 5.3). Using the offline $CaCO_3$ box model, the inter-basin difference in average long-term (~100 kyr) surface sediment $CaCO_3$ burial flux is estimated in CLOSED; 0.049 PgC a^{-1} in the Pacific and 0.061 PgC a^{-1} in the Atlantic. Opening the NARROW CAS increases $CaCO_3$ long-term burial flux in the Pacific to 0.061 PgC a^{-1} and decreases it in the Atlantic to 0.057 PgC a^{-1} (Table 5.3). Comparing point locations of the box model long-term $CaCO_3$ burial flux to paleoclimate proxy data (Section 1.3) at ODP locations in the EEP and Caribbean, I find a similar inter-basin $CaCO_3$ long-term burial flux shift with the addition of the NARROW CAS; increase from 0 to 0.51 gC a^{-1} in the EEP (ODP site 846, Table 1.1; Table 5.3) and decrease from 1.25 to 0.63 gC a^{-1} in the Caribbean (ODP site 999, Table 1.1; Table 5.3). The largest inter-basin changes in NARROW are in the Pacific consistent with the location of the largest ocean mean ideal age changes, indicative of the impact of ventilation changes on long-

term $CaCO_3$ preservation. The shifting patterns of long-term $CaCO_3$ burial flux with a NARROW CAS result in a transient decrease in the global alkalinity inventory until $CaCO_3$ burial in the Atlantic ceases since it is also being preserved in the Pacific. Upon closure of the CAS, there is a net migration of surface sediment $CaCO_3$ – or the difference in the spatial distribution of $CaCO_3$ in the active layer of 10 cm surface sediment by which the model needs to come to re-equilibrium – on the order of ~150 PgC and provides an upper limit on the increase in ocean alkalinity (~300 PgC) associated with this migration. Therefore, the largest impact of the open CAS on the carbonate chemistry is in the long-term shifting spatial patterns, rather than the global changes, of $CaCO_3$ and its effect on alkalinity.

The inter-basin differences in alkalinity and DIC show a general increase in the Atlantic and a decrease in the Pacific (Fig. 5.11b) with a similar spatial pattern as the ventilation changes inferred from the ideal ocean age at the same depth (Fig. 5.3b, left). Basin average DIC and alkalinity values in NARROW are 85 and 27 PgC greater in the Atlantic and 268 and 27 PgC less in the Pacific, respectively (Table 5.3), compared to CLOSED. The largest values of alkalinity and DIC at 2049 m (e.g., below the NARROW sill depth) are in the Pacific, specifically, the EEP in CLOSED (Fig. 5.11a; Table 5.3). This is a primary region of upwelling of cooler water with increased solubility of CO_2 and low biological productivity. This is also the region with the largest decreases in alkalinity and DIC in NARROW; alkalinity decreases by ~4%, DIC by ~8% (Fig. 5.11b, left and right, respectively), with implications for changes in biological productivity. Alkalinity and DIC decrease globally with a seaway (Fig. 5.1c and Fig. 5.1d). In addition to the spatial pattern of changes in $CaCO_3$ burial flux, the reduction in alkalinity is also

due, in part, to the reduction in water column denitrification as reflected in the increase in total NO_3^- inventory (Fig. 5.1b).

Ocean alkalinity (Fig. 5.1c) and DIC inventories (Fig. 5.1d) decrease with a CAS in a 2:1 ratio (Table 5.1). While the preindustrial global ocean DIC is in quasi-equilibrium with 36894.7 PgC, it is reduced by 210.1 PgC in NARROW (Table 5.1). This is an upper bound on the carbon storage decrease as the DIC inventory has a long-term decreasing trend of ~0.1 PgC a^{-1} through the end of the 4000 year NARROW simulation (Fig. 5.1d). This trend is assumed to be steady-state since it follows the alkalinity long-term decrease associated with trending bottom water saturation state from the long-term sediment $CaCO_3$ equilibration time scales, as previously discussed (Section 2.1). There is also a long-term (over 4000 integration years) increasing trend of ~200 PgC in the surface sediment $CaCO_3$ inventory in the CLOSED simulation (Fig. 5.1h). However, the CLOSED long-term "permanent" burial fluxes of surface sediment $CaCO_3$ (Fig. 5.1g) are roughly in balance with the river fluxes of alkalinity and DIC at steady-state (Fig. 5.1g, dashed lines). The rate of increase in long-term burial flux of surface sediment $CaCO_3$ is faster in NARROW than CLOSED, showing the long equilibrium time scales (Fig. 5.1g). Combining GFDL-ESM2G output with the offline $CaCO_3$ box model (Dunne et al. 2012a), the long-term burial fluxes of surface sediment $CaCO_3$ are computed; 0.1604 PgC a^{-1} in NARROW compared to 0.1589 PgC a^{-1} in CLOSED (Table 5.1). While this increase may seem relatively small (~1%) compared to the inter-basin changes previously discussed, it has implications for large changes in the surface sediment $CaCO_3$ pool, especially over the very long time scales of $CaCO_3$ burial (~10^5 years). For example, after 4000 years of integration (e.g., not yet steady-state), the surface sediment $CaCO_3$ pool

has an additional 47.8 PgC in NARROW compared to CLOSED (Fig. 5.1h).

5.5 Seaway Impacts on Short Time Scale Ocean-Atmosphere Carbon Fluxes and Atmosphere pCO_2 Concentrations

Zonally averaged, the pattern of changes in the annual average flux of CO_2 out of the ocean with a CAS is similar to the pattern of changes in the annual average atmosphere pCO_2 flux (from the land plus ocean) with a NARROW CAS (Fig. 5.12). In the SH extratropics (~40-70ºS), Southern Ocean CO_2 outgassing (Figs. 5.12b and 5.13) decreases with an open seaway and reduces the atmosphere net CO_2 flux (Fig. 5.12a). There is a slight southward shift in the peaks of net ocean and atmosphere CO_2 fluxes in the SH extratropics (Fig 5.12a) with an open CAS. Opening the CAS reduces the CO_2 outgassing by the ocean in the EEP region (Fig. 5.13). In the NH extratropics (~40-70ºN) and ~20ºS, ocean CO_2 uptake decreases in NARROW (Fig. 5.12b) which increases the CO_2 flux to the atmosphere from the land and ocean to near-zero values (Fig. 5.12a). In the North Atlantic, the ocean switches from a net uptake to a net outgassing of CO_2 with an open CAS (Fig. 5.13), as is also reflected in the zonal average atmosphere net CO_2 flux (Fig. 5.12). This is indicative of an increase in remineralized DIC and the sequestration efficiency of the biological pump from increased ocean ideal age above 2000 m (Fig 5.3d). Reduced (0.4 Sv) southward mass transport in this region (Fig. 3.5a) prevents the southward transport of CO_2 from the bottom water out of this region, resulting in an increase in the northward transport of CO_2 flux (Fig. 5.12c) with an open CAS.

The changes in the oceanic alkalinity and DIC inventory with an open CAS impact the time-integrated air-sea CO_2 fluxes (Fig. 5.1f); opening the CAS results in an increase in ocean CO_2 outgassing (Fig. 5.1e). The quasi-equilibrium air-sea CO_2 exchange contributes 0.012 PgC a^{-1} to the atmosphere in CLOSED (Table 5.1). An additional 0.187 PgC a^{-1} is outgassed by the ocean in NARROW (Table 5.1). After 1400 integration years, there is an additional 251.7 PgC released to the atmosphere with an open seaway (Fig. 5.1f); much larger than the long-term trend in CLOSED (an outgassing of ~50 PgC over 4000 integration years), and competitive with the expected volcanism and weathering rates. After 4000 years, there is an increase in atmosphere pCO_2 of 506.8 PgC or 237.9 ppmv in NARROW compared to CLOSED. This long time scale ocean CO_2 outgassing and release of 506.8 PgC to the atmosphere with the NARROW seaway can be used to compute the relative change in temperature using the transient climate response to cumulative carbon emissions (TCRE) obtained from analysis of 15 CMIP5 models and constrained by observations (Gillett et al. 2013). TCRE is a useful indicator of the ratio of warming to cumulative CO_2 emissions because it is time- and emission scenario-independent. Using the range of TCRE estimated by Gillett et al. (2013), 0.7-2.0 K EgC^{-1}, and the cumulative CO_2 emissions from ocean outgassing after 4000 integration years (506.8 PgC), the warming from the NARROW seaway is estimated, 0.4-1.0 K. Since carbon in the deep ocean in NARROW is not in steady-state at this point in the integration and the ocean does not serve as a carbon sink in this case, this elevated atmosphere pCO_2 concentration in NARROW seaway is an underestimate. Over the historical period, the ocean is estimated to have taken up ~25% of the CO_2 emissions. Therefore, the effective emissions would be ~1/0.75 fold the ocean emissions over the

multi-decadal time scale, resulting in an even larger TCRE, up to ~1.1K with an open CAS.

Taken forward in time over the Pliocene, these results suggest that the closure of the CAS resulted in a blockage of the main ventilation pathway of the deep Pacific, thus both (a) directly sequestering hundreds of PgC more remineralized CO_2 in the deep Pacific on centennial to millennial timescales, and (b) making those waters increasingly corrosive to $CaCO_3$ preservation serving to prevent $CaCO_3$ burial of sinking and dissolving previously buried $CaCO_3$, releasing hundreds of PgC-equivalents alkalinity over centennial to 100 kyr timescales. This drives down atmospheric CO_2 and combining with the direct climate cooling (Chapter 4) associated with the CAS closure circulation changes results in an overall cooling of up to nearly 2K.

5.6 Comparison with Proxy Records, Climate Models, and Implications

Opening the CAS increases ventilation of the deep ocean which reduces the sequestration efficiency of the biological pump and allows respired CO_2 to escape up to the atmosphere. The loss of DIC (with no loss of alkalinity) increases the deep ocean CO_3^{2-} leading to a short-term (< 500 kyr) increase in $CaCO_3$ burial of 0.002 PgC a^{-1} corresponding to large increases in the global sediment $CaCO_3$ pool (~200 PgC over 10^5 years) in which alkalinity and DIC are removed in a 2:1 ratio. The removal of alkalinity and DIC continues until the deep CO_3^{2-} falls back to its original level and the burial of $CaCO_3$ comes back into balance with the river input. The enhanced burial of $CaCO_3$ during this interval leads to an additional release of 237.9 ppmv (506.8 PgC) to the

atmosphere from the partitioning of CO_2. Dunne et al. (2012a) found that changes in ventilation in the North Atlantic during glacial periods results in more corrosive water invading the North Atlantic and an increase in total alkalinity. As bottom water $CaCO_3$ saturation state increased in the Atlantic in response to the ventilation changes, it decreased in the Pacific leading to increased $CaCO_3$ burial in the Pacific. My results in this dissertation are similar to Dunne et al. (2012a) in that both studies demonstrate that changing deep-water circulation affects long time scale $CaCO_3$ sequestration and, ultimately, atmosphere pCO_2 concentrations, with varying regional patterns. This mechanism is important since observations of surface warming associated with increasing anthropogenic CO_2 concentrations since 1970 indicate an increase in surface stratification and inhibited ventilation (Rhein et al. 2013).

Using the offline $CaCO_3$ box model of Dunne et al. (2012a), I find decreases in point locations in the Caribbean and increases in the EEP surface sediment $CaCO_3$ permanent burial with an open CAS. Haug and Tiedemann (1998) suggest that sand fraction carbonate mass accumulation rates, from the same Caribbean and EEP ODP locations as the surface sediment $CaCO_3$ long-term burial fluxes I estimated with GFDL-ESM2G converged around the time of CAS closure (Fig. 1.4). This is consistent with GFDL-ESM2G results indicating a decrease in Caribbean-EEP difference in $CaCO_3$ permanent burial flux from 1.25 gC a^{-1} in CLOSED to 0.63 gC a^{-1} with the NARROW seaway (Table 5.3). The decrease in Caribbean $CaCO_3$ sedimentation in my results is also consistent with their proxy records obtained from ODP site 999 (Table 1.1). However, the GFDL-ESM2G EEP surface sediment $CaCO_3$ permanent burial flux increases with the NARROW seaway (from 0 to 0.51 gC a^{-1}), while they found no significant change. My

results are consistent with the mechanism involved in driving changes in $CaCO_3$ burial simulated by the model, such as the presence of the seaway altering ventilation and sequestration time scales. The differences between my results and Haug and Tiedemann (1998) may be due to differences in sampling considering their ODP proxy records (Table 1.1) represent only one point-location in the Caribbean, and this may not be representative of the regional EEP carbonate burial flux changes during the Pliocene. Furthermore, the increase in EEP $CaCO_3$ preservation in my results is consistent with proxy records indicating an increase and eastward shift in $CaCO_3$ mass accumulation rates (Lyle 2003) and opal (Farrell et al. 1995), from 100º to 110ºW ~6 Ma towards South America (80º-90ºW), and decreases in ^{13}C from benthic foraminifera in this region ~3 Ma (Mix et al. 1995).

This idealized climate modeling study provides a mechanism, the open CAS, for increased short time scale (< 500 kyr) atmosphere pCO_2 concentrations and warming in the Pliocene, before the atmosphere pCO_2 concentrations return to their original values from the long time scale effects of chemical weathering and volcanism. My estimate of global average atmosphere pCO_2 concentrations (~524 ppmv) from the ocean release of CO_2 to the atmosphere with the NARROW seaway lies just outside the high range of estimates (~200-500 ppmv) from Fedorov et al. (2013) for the Pliocene, which have a large range in uncertainty from the various biogeochemical methods they are based on. While their ESM results suggest that the CAS was not a mechanism of Pliocene warmth, they were unable to simulate the coupled atmosphere pCO_2 impacts with the CAS, which I found to be substantial and contribute to a global average warming ~1.1K when considering the cumulative emissions. While the increased atmosphere pCO_2 in my

results is short term relative to the geological time scales of the evolution of the CAS, there is considerable uncertainty in the evolution of the CAS from paleoclimate proxy indicators (Section 1.3).

Schneider and Schmittner (2006) hypothesized that increased deep water formation and marine NPP following the CAS closure may have increased CO_2-drawdown from the atmosphere by the ocean and lead to cooling, but their unpublished results did not show a large change in atmosphere pCO_2. However, their experiments used a coarse spatial resolution ESM of intermediate complexity with an Energy Balance Model (EBM) atmosphere and may not represent many of the interactions and feedbacks in the climate-carbon cycle between the atmosphere and ocean. An alternative hypothesis for Pliocene warmth is that the shoaling of the EEP thermocline since the Miocene due to changing ocean gateways (e.g., CAS) increased ocean SST and atmosphere pCO_2 coupling, thereby increasing climate sensitivity to pCO_2 forcing during the Pliocene (LaRiviere et al. 2012). To test this hypothesis, I performed additional idealized open/closed CAS sensitivity experiments with GFDL-ESM2G where atmosphere pCO_2 was increased by 1% per year to a doubling of preindustrial concentrations (e.g., 572 ppmv) for the CLOSED, NARROW, and WIDE simulations. The transient climate sensitivity – or SAT anomaly at the time of CO_2 doubling – is 1.21 K for CLOSED but does not show any significant change with the presence of a CAS (1.15-1.27 K) and does not support the hypothesis of LaRiviere et al. (2012).

My results also indicate that an increase in nutrient-rich (e.g., NO_3^-) surface Pacific water into the Caribbean with the open CAS increases NPP in this region. Surface nutrient concentrations increase in the North Atlantic with an open CAS from the influx

of relatively high nutrient Pacific water. Productivity increases in response to increased nutrient sequestration time scales and dissolved O_2 decreases in response to increased respiration. Opening the CAS leads to the nutrient-rich EEP becoming depleted of surface NO_3^- concentrations with the advection of Atlantic surface water through the CAS into the Pacific and productivity in this region decreases consistent with increased dissolved O_2 concentrations from reduced respiration. Furthermore, with the open CAS global total productivity decreases 5%. My results of the spatial patterns of surface NO_3^- concentrations and productivity with an open CAS are consistent with results from the Schneider and Schmittner (2006) ocean ecosystem model with an EBM atmosphere with varying seaway sill depths (130, 700, and 2000 m) over a ~450-km wide seaway. They also found a decrease in global productivity with an open CAS, although their 20-25% decrease is larger than the GFDL-ESM2G results. The increase in productivity in the North Atlantic in my results is also consistent with proxy records indicating higher productivity species in the North Atlantic during the Pliocene (Bartoli et al. 2005), compared to the approximate time of CAS closure.

Comparison of the CLOSED and NARROW biogeochemical time series demonstrates the relatively long time scales associated with ocean biogeochemical equilibrium, and the GFDL-ESM2G results in this analysis are not in sediment equilibrium although they are converging on a water mass quasi-equilibrium state as previously discussed (Section 2.3). While the surface sediment $CaCO_3$ storage is increasing in CLOSED from trending bottom water $CaCO_3$ saturation state, the permanent burial of $CaCO_3$ is roughly in balance with the river supply of DIC and alkalinity as reflected in the DIC and alkalinity equilibrium in CLOSED. This analysis also does not

consider short time scales associated with the terrestrial biosphere response to the changes in climate from the CAS. This research may be expanded in the future by examining the short time-scale impacts on land carbon (e.g., vegetation biomass, soil carbon). The asymmetric, bipolar SAT response with an open CAS described in Chapter 4 may result in shifting temperate forest/taiga boundary in the NH as it cools and southward shifts in tropical terrestrial biomass and grasslands, at the expense of deserts, in response to the slight southward shift in the ITCZ. Changes in soil carbon respiration and global terrestrial biomass may impact the terrestrial carbon stores and fluxes and atmosphere pCO_2 concentrations on relatively short time scales (~100 years). However, the relatively longer time-scale analysis of the ocean biogeochemical impacts examined in this chapter imply that changing deep-water circulation can have large-scale impacts on marine ecosystems and atmosphere pCO_2 concentrations with associated feedbacks on global mean climate, and are important to consider especially in the context of tipping points.

Chapter 6

Summary and Concluding Remarks

6.1 Summary of the Dissertation

The presence of the Central American Seaway (CAS) in GFDL-ESM2G, largely independent of the stage of shoaling, had a significant effect on the horizontal and vertical global ocean circulation by altering and redistributing water mass properties through changing inter-basin transport throughout the full depth of the ocean. The additional circulation pathway available with the introduction of the seaway transported water mass and its characteristics through the CAS rather than through the ITF, and continued in a global, zonal band throughout the SH. The water is warmed in the tropics after traveling through the CAS, and flows into the South Atlantic. The increased southward OHT results in an asymmetric, bipolar SST response with global average warming dominated by the SH and extends throughout the depth of the ocean. The increased southward salt transport increases annual average global salinity from the surface to the upper 100 m and decreases global salinity below this level to the bottom. Top 100-m global ocean density increases with a seaway and is directly attributed to changes in salinity, rather than changes in temperature, with the CAS. The CAS changes deep-water circulation by suppressing the northward extent of AABW in the Atlantic and allowing NADW to penetrate deeper and slightly strengthen. The dispersion of Atlantic Ocean water mass characteristics from the circulation pathway established with the open CAS changes the Indo-Pacific deep-water circulation.

Global mean climate and interannual variability in the tropical Pacific are

substantially different before and after the CAS closed at the end of the Pliocene era. The ocean mass and heat transports with an open CAS decrease poleward heat transport in the NH and increase it in the SH. This results in a similar bipolar, asymmetrical SAT pattern of SH warming and NH cooling for all shoaling stages of the open CAS, with the largest sensitivity in SAT patterns to the earlier stage of CAS shoaling. The ITCZ shifts slightly southward from this differential inter-hemispheric heating, and global precipitation rates intensify (almost double) with the earlier, WIDE CAS compared to the later, NARROW CAS. The largest changes in ocean transport driving the mean climate response occur along the SH extratropical circulation pathway established by the open CAS, where sea ice and low cloud cover is reduced affecting the atmospheric radiative properties in this region. Opening the CAS leads to intensification of the surface southeasterly trade wind strength at the expense of reduced trade wind strength in the NH. With the open CAS, the tropical Pacific upper 300 m warms more than the surface, deepening the thermocline with a large local response in the CAS region, and the east-west SST gradient increases mainly from the warming in the west/central Pacific from reduced OHT through the ITF. In the EEP, the advection of cooler surface water from the bi-directional net horizontal mass transport through the wider seaways shifts the minimum SSTs slightly eastward. With the CAS, north-south SST asymmetry on either side of the equator in the east Pacific decreases and leads to an enhancement of the semi-annual cycle of ENSO variability and a reduction in the cross-equatorial thermocline asymmetry in the east Pacific. The east-west tropical Pacific thermocline gradient increases, with the largest response to the wider seaways due to the bi-directional horizontal water mass transport and temperature advection. There is an increase in ENSO amplitude, largest with the

earlier CAS, more cold events (La Niña) consistent with the cooling in the EEP, a weakened annual and strengthened semi-annual (driven by the decreased north-south SST asymmetry in the east Pacific) and interannual cycles, earlier El Niño and La Niña development, and stronger atmospheric global impacts with the open CAS. This research implies that coupled ocean-atmosphere dynamics are sensitive to changes in ocean mass, heat, and salt transport in response to changing ocean circulation and have far-reaching, global impacts. These changes in climate from geologically-driven changes associated with a SAT warming of 0.4-0.7°C represent a starkly different set of regional climate fingerprints than those from anthropogenic-driven changes associated with greenhouse gas warming (e.g., RCP2.6), such as tropical warming and polar amplification, expansion of the Hadley circulation, reduction in AMOC). This provides an important reference point of caution when applying paleoclimate proxy records to climate changes under future warming conditions, and an alternative perspective on how starkly different climate change patterns might look if drivers other than an increase in greenhouse gases where dominating that change.

The global ocean circulation with the addition of the NARROW seaway altered ocean ventilation and the sequestration time scales of the global biological pump, thereby, impacting atmosphere pCO_2 concentrations. These results indicate that global NO_3^- inventory increases by 63.1 PgN from a reduction in water column denitrification but NPP decreases 3.9 PgC a^{-1} with a single grid point channel representation of the CAS. The largest increase in surface NO_3^- concentrations are in the Southern Ocean with increases up to ~50% in the Weddell Sea, North Pacific, and North Atlantic. However, productivity changes in the Southern Ocean do not change very much most likely

because the biological pump is operating at maximum efficiency relative to the supply of iron, which is fixed in this model. Productivity doubles in magnitude directly to the east of the CAS in the Caribbean, with increases also in the North Atlantic. Subsurface (below 100 m) global NO_3^- inventory increases by 65 PgN. The largest increases in vertically integrated subsurface NO_3^- (up to ~36 μmol kg^{-1}) occur in the EEP and Atlantic, where PON sinking flux increases suggesting that productivity in these regions is from larger phytoplankton. Overall, the spatial patterns of PO_4^{3-} concentrations are similar to NO_3^-, except for the EEP where the largest decreases occur (up to ~3.2 μmol kg^{-1}). Overall, increased ventilation reduces OMZs, especially in the EEP with increases up to ~100 μmol kg^{-1}, except for the west coast of Africa where dissolved O_2 concentrations decrease with an open CAS.

Opening the CAS increases ventilation of the deep ocean which reduces the sequestration efficiency of the biological pump which simultaneously reduces the corrosiveness of Pacific waters to $CaCO_3$ burial and allows respired CO_2 to escape up to the atmosphere. The loss of DIC (with no loss of alkalinity) increases the deep ocean CO_3^{2-} leading to a short-term – relative to geological time scales – increase in $CaCO_3$ burial and a net migration of ~150 PgC from the spatial distribution of $CaCO_3$ in the active layer of 10 cm surface sediment, which provides the upper limit on the decrease in ocean alkalinity (~300 PgC) associated with this migration in which alkalinity and DIC are removed in a 2:1 ratio. The removal of alkalinity and DIC continues until the deep CO_3^{2-} falls back to its original level and the burial of $CaCO_3$ comes back into balance with the river input. The enhanced burial of $CaCO_3$ during this interval leads to an additional release of 237.9 ppmv (506.8 PgC) to the atmosphere from the partitioning of

carbon species after 4000 integration years with an open, narrow seaway, and a warming of 0.4-1.0 K from the cumulative carbon emissions during the Pliocene. In summary, the presence of the CAS in GFDL-ESM2G had a significant effect on global ocean circulation which drove changes in mean climate, ENSO, and marine biogeochemistry that are consistent with paleoclimate proxy indicators.

6.2 Concluding Remarks

This dissertation concentrates on how the presence of a single perturbation, the open CAS, impacts the Earth system. This particular framework is valuable for attribution studies and, thus, allows for the evaluation of how various processes, interactions, and feedbacks in the Earth system are altered holistically, without any other changes to the system. Therefore, the underlying motivation for this work was to better understand the Earth system sensitivity to a perturbation. For this objective, I chose a known perturbation in Earth's history for comparison with available paleoclimate proxy indicators and CAS climate models. I also showed that the spatial fingerprints of responses to external forcing can be strikingly different. The novelty of this work was made possible using the state-of-the-art GFDL-ESM2G model and an offline $CaCO_3$ box model. Climate models found that the buoyancy changes in the North Atlantic and the weakening of the AMOC in response to the open CAS drove changes in climate. I presented differences between my results and those from other climate models (e.g., AMOC strength, meridional OHT direction, global mean SAT spatial pattern) and large-scale similarities (e.g., tropical Pacific thermocline deepening, tropical Pacific SST increase, ENSO magnitude and variability, nutrient concentration spatial patterns). In

conclusion, it is the large-scale ocean circulation changes – and not changes in AMOC which has been the prime focus of previous studies – that drive changes in climate and ocean biogeochemistry with the addition of the CAS. A significant and probably the most surprising finding is that the very narrow opening of the CAS can invoke significant climate impacts, such as 0.4-1K global mean SAT warming which is comparable to the warming in future climate projections under increased greenhouse gas emissions, and an ~238 ppmv increase in atmosphere pCO_2.

There are several implications of this dissertation that broadly apply to the current state of climate science. First, regional perturbations in Central American topography have far-reaching effects on deep-ocean circulation and is important for understanding global impacts associated with possible future analogs, such as ice sheet collapse and freshwater input in response to climate change. Second, this paleoclimate application simulates a warmer global mean climate and has implications for understanding how various mechanisms (tropical equatorial SSTs, tropical Pacific upper ocean dT/dz, y-asymmetry of the SST about the equator and of the zonal wind stress about the equator, trade wind strength, global mean precipitation and precipitation variability in the central Pacific associated with ENSO) respond to future climate warming under elevated atmosphere pCO_2 concentrations. While the global mean response to different external forcings may be similar, the spatial fingerprint can be dramatically different, and caution should be taken when using global mean warming as a single metric for assessing climate impacts. Finally, changes in ocean circulation in response to a perturbation can affect ocean ventilation/flushing and have large-scale, long-term impacts on ocean biogeochemical properties, ocean ecosystems, and atmosphere pCO_2 concentrations.

On the whole, this dissertation focuses on assessing the broad impact on the coupled Earth system to a paleoclimate application representing a perturbation to the system. While I find the paleoclimate record full of fascinating events, my primary motivation for pursuing this particular dissertation topic is broader. To study the Earth system impacts from various forcings, it is important to understand how all the components interact. In conclusion, this dissertation allowed me to better understand these interactions, as well as ocean biogeochemistry and ENSO variability, and was a valuable learning experience to enable me to better pursue my research interests in studying climate and carbon cycle interactions and feedbacks on a variety of time scales using ESMs.

References

Anderson, L. A., 1995: On the hydrogen and oxygen content of marine phytoplankton. *Deep-Sea Res. I*, **42**, 1675–1680.

Anderson M. A., and F. M. M. Morel, 1982: The influence of aqueous iron chemistry on the uptake of iron by the coastal diatom *Thalassiosira weissflogii*. *Limnology and Oceanography*, **27**, doi: 10.4319/lo.1982.27.5.0789.

Anderson, J. L., and Coauthors, 2004: The New GFDL Global Atmosphere and Land Model AM2–LM2: Evaluation with Prescribed SST Simulations, *J. Climate*, **17**, 4641–4673, https://doi.org/10.1175/JCLI-3223.1.

Antonov, J. I., R. A. Locarnini, T. P. Boyer, A. V. Mishonov, and H. E. Garcia, 2006: Salinity. *World Ocean Atlas 2005*, Vol. 2, NOAA Atlas NESDIS 62, 182 pp.

Bartoli G., M. Sarnthein, M. Weinelt, H. Erlenkeuser, D. Garbe-Schonberg, and W. Lea, 2005: Final closure of Panama and the onset of Northern Hemisphere glaciation. *Earth Planet. Sci. Lett*., **237**, 33–44.

Bell D. B., S. J. A. Jung, D. Kroon, L. J. Lourens, and D. A. Hodell, 2014: Local and regional trends in Plio-Pleistocene $\delta^{18}O$ records from benthic foraminifera. *Geochemistry, Geophys. Geosystems*., **15**, 3304–3321, 10.1002/2014GC005297

——, ——, ——, D. A. Hodell, L. J. Lourens, and M. E. Raymo, 2015: Atlantic Deep-water Response to the Early Pliocene Shoaling of the Central American Seaway. *Sci. Rep*., **5**, 12252, https://doi.org/10.1038/srep12252.

Bjerknes, J., 1969: Atmospheric teleconnections from the equatorial Pacific. *Mon. Wea. Rev.*, **97**(3), 163–172, doi:10.1175/1520-0493(1969)097<0163:ATFTEP>2.3.CO;2.

Billups, K., A. Ravelo, and J. C. Zachos, 1998: Early Pliocene deep water circulation in the western equatorial Atlantic: Implications for high-latitude climate change. *Paleoceanography*, **13**, 84–95.

Broccoli, A. J., K. A. Dahl, and R. J. Stouffer, 2006: Response of the ITCZ to Northern Hemisphere cooling. *Geophys. Res. Lett*., **33**(1), L01702, doi:10.1029/2005GL024546.

Broecker, W. S., 1974: "NO" A conservative water-mass tracer. *Earth Planet. Sci. Lett.*, **23**, 100 –107.

——, 1998: Paleocean circulation during the last deglaciation: A bipolar seesaw? Paleoceanography, 13(2), 119–121.

——, and T. H. Peng. 1982: Tracers in the Sea, Eldigio Press, Palisades, NY, 690 pp.

——, T. Takahashi, and T. Takahashi, 1985: Sources and flow patterns of deep ocean waters as deduced from potential temperature, salinity, and initial phosphate concentration. *J. Geophys. Res*., **90**, 6925– 6939.

Bryan, F., 1986: High-latitude salinity effects and interhemispheric thermohaline circulations. *Nature*, **323**, 301–304.

Burton, K. W., H.-F. Ling, and K. O'Nions, 1997: Closure of the Central American Isthmus and its effect on deep-water formation in the North Atlantic. *Nature*, **386**, 382–385.

Butzin, M., G. Lohmann, and T. Bickert, 2011: Miocene ocean circulation inferred from marine carbon cycle modeling combined with benthic isotope records. *Paleoceanography*, **26**, PA1203, doi:10.1029/2009PA001901.

Cane, M. A., and E.S. Sarachik, 1979: Forced baroclinic ocean motions, III: The equatorial basin case. *J. Marine Res*., **37**, 355-398.

Cannariato, K. G. and A. C. Ravelo, 1997: Pliocene-Pleistocene evolution of the eastern Pacific surface water circulation and thermocline depth. *Paleoceanography*, **12**, 805–820.

Capotondi, A., A. Wittenberg, and S. Masina, 2006: Spatial and temporal structure of tropical Pacific interannual variability in 20th century coupled simulations. *Ocean Modell*., **15**, 274–298.

Carr, M. -E., and Coauthors, 2006: A comparison of global estimates of primary production from ocean color. *Deep-Sea Res. II*, **53**, 741–770.

Chaisson, W. P., and R. M. Leckie: 1993: High-resolution Neogene planktonic foraminifer biostratigraphy of Site 806, Ontong Java Plateau (western equatorial Pacific). *Proc. ODP, Sci Results*, W. H. Berger, L. W. Kroenke, L. A. Mayer, Eds., Ocean Drilling Program, College Station, TX, vol. 130, pp. 137-178.

——, and A. C. Ravelo, 2000: Pliocene development of the east–west hydrographic gradient in the equatorial Pacific. *Paleoceanography*, **15**, 497–505, doi:10.1029/1999PA000442.

Coates, A. G. and J. A. Obando, 1996: The geologic evolution of the central American Isthmus, *Evolution and Environment in Tropical America*, Jackson, J. B. C., A. F. Budd, and A. G. Coates, Eds., Univ. Chicago Press, Chicago, 21 – 56.

Coates, A. G., L. S. Collins, M. -P. Aubry, and W. A. Berggren, 2004: The Geology of the Darien, Panama, and the late Miocene-Pliocene collision of the Panama arc with northwestern South America. *Geol. Soc. Amer. Bull*., **116**, 1327-1344.

Collier, M. A., and P. Durack, 2006: CSIRO netCDF version of the NODC World Ocean Atlas 2005. Commonwealth Scientific and Industrial Research Organisation Marine and Atmospheric Research Paper 15, 45 pp.

Collins, L. S., A. G. Coates, J. B. C. Jackson, and J. A. Obando, 1995: Timing and rates of emergence of the Limón and Bocas del Toro basins: Caribbean effects of Cocos Ridge subduction? *Geologic and tectonic development of the Caribbean plate boundary in southern Central America*, P. Mann, Ed., Spec. Pap. Geol. Soc. Amer., **295**, 263-289.

Compo, G. P., and Coauthors, 2009: NOAA CIRES Twentieth Century Global Reanalysis Version 2. Research Data Archive at the National Center for Atmospheric Research, Computational and Information Systems Laboratory. http://dx.doi.org/10.5065/D6QR4V37. Accessed 17 JUL 2016.

Corrigan, J., P. Mann, and J. C. Ingle Jr., 1990: Forearc response to subduction of the Cocos Ridge, Panama-Costa Rica. *Geol. Soc. Amer. Bull*., **102**, 628–652.

de Boer, J. Z., M. S. Drummond, M. J. Bordelon, M. J. Defant, H. Bellon, and R. C. Maury, 1995: Cenozoic magmatic phases of the Costa Rican island arc (Cordillera de Talamanca). *Geologic and Tectonic Development of the Caribbean Plate Boundary in Southern Central America*, P. Mann, Ed., Spec. Pap. Geol. Soc. Amer., **295**, 35– 55.

Dekens, P. S., A. C. Ravelo, and M.D. McCarthy, 2007: Warm upwelling regions in the Pliocene warm period. *Paleoceanography*, **22**, PA3211.

Delworth, T. L., and M. E. Mann, 2000: Observed and simulated multidecadal variability in the Northern Hemisphere. *Climate Dyn.*, **16**, 661–676, doi:10.1007/s003820000075.

——. and F. Zeng, 2016: The impact of the North Atlantic Oscillation on climate through its influence on the Atlantic Meridional Overturning Circulation. *J. Climate*, **29**(3), 941-962.

——, and Coauthors, 2006: GFDL's CM2 Global Coupled Climate Models. Part I: Formulation and Simulation Characteristics. *J. Climate*, **19**(5), doi:10.1175/JCLI3629.1.

Dong B., and R. T. Sutton, 2007: Enhancement of ENSO variability by a weakened Atlantic thermohaline circulation in a coupled GCM. *J. Climate*, **20**, 4920–4939.

Dowsett, H. J., and Coauthors, 2012: Assessing confidence in Pliocene sea surface temperatures to evaluate predictive models. *Nat. Climate Change*, **2**, 365–371.

Driscoll, N. W. and G. H. Haug, 1998: A Short Circuit in Thermohaline Circulation: A Cause for Northern Hemisphere Glaciation? *Science*, **282**, 436–438.

Dunne, J. P., R. A. Armstrong, A. Gnanadesikan, and J. L. Sarmiento, 2005: Empirical and mechanistic models for particle export ratio. *Global Biogeochem. Cycles*, **19**, GB4026, doi:10.1029/2004GB002390.

——, J. L. Sarmiento, and A. Gnanadesikan, 2007: A synthesis of global particle export from the surface ocean and cycling through the ocean interior and on the seafloor. *Global Biogeochem. Cycles*, **21**, GB4006, doi:10.1029/2006GB002907.

——, A. Gnanadesikan, J. L. Sarmiento, and R. D. Slater, 2010: Technical description of the prototype version (v0) of Tracers of Phytoplankton with Allometric Zooplankton (TOPAZ) ocean biogeochemical model as used in the Princeton IFMIP model. *Biogeosciences*, **7** (Suppl.), 3593, doi:10.5194/bg-7-3593-2010.

——, J. R. Toggweiler, and B. Hales, 2012a: Global calcite cycling constrained by sediment preservation controls. *Global Biogeochem. Cycles*, **26**, GB3023, doi:10.1029/2010GB003935.

——, and Coauthors, 2012b: GFDL's ESM2 global coupled climate-carbon Earth System Models Part I: Physical formulation and baseline simulation characteristics. *J. Climate*, **25**(19), doi:10.1175/JCLI-D-11-00560.1.

——, and Coauthors, 2013: GFDL's ESM2 global coupled climate-carbon Earth System Models Part II: Carbon system formulation and baseline simulation characteristics. *J. Climate*, **26**(7), doi:10.1175/JCLI-D-12-00150.1.

Duque-Caro, H., 1990: Neogene stratigraphy, palaeoceanography and palaeobiogeography in northwest South America and the evolution of the Panama Seaway. *Palaeogeogr. Palaeoc. Palaeoecol*., **77**, 203-234.

England M. H., S. McGregor, P. Spence, G. A. Meehl, A. Timmermann, W. Cai, A. S. Gupta, M. J. McPhaden, A. Purich, and A. Santoso, 2014: Recent intensification of wind-driven circulation in the Pacific and the ongoing warming hiatus. *Nat. Climate Change*, **4**(3), 222–227.

Fedorov, A. V., P. S. Dekens, M. McCarthy, A. C. Ravelo, P. B. deMenocal, M. Barreiro, R. C. Pacanowski, and S. G. Philander, 2006: The Pliocene Paradox (Mechanisms for a Permanent El Niño). *Science*, **9**, 312 (5779), 1485-1489, doi:10.1126/science.1122666.

——, C. M. Brierley, K. T. Lawrence, Z. Liu, P. S. Dekens, and A. C. Ravelo, 2013: Patterns and mechanisms of early Pliocene warmth. *Nature*, **496**, 43-49, doi:10.1038/nature12003.

Falkowski P. G., R. T. Barber, and V. Smetacek, 1998: Biogeochemical controls and feedbacks on ocean primary production. *Science*, **281**, 200–6.

Fan, S.-M., W. J. Moxim, and H. Levy II, 2006: Aeolian input of bioavailable iron to the ocean. *Geophys. Res. Lett*., **33**, L07602, doi:10.1029/2005GL024852.

Farrell, J. W., and Coauthors, 1995: Late Neogene sedimentation patterns in the eastern equatorial Pacific Ocean. *Proceedings of the Ocean Drilling Program*, N. G. Pisias, L. A. Mayer, T. R. Palmer-Julson, T. H. van Andel, Eds., 138, ODP, 717–756.

Feng, R., and C. J. Poulsen, 2014: Andean elevation control on tropical Pacific climate and ENSO. *Paleoceanography*, **29**, 795–809, doi:10.1002/2014PA002640.

Fetterer, F., K. Knowles, W. Meier, and M. Savoie, 2009: Sea ice index. National Snow and Ice Data Center, Boulder, CO, digital media. [Available online at http://nsidc.org/data/g02135.html] Accessed 17 JUL 2016.

Field, C. B., M. J. Behrenfeld, J. T. Randerson, and P. Falkowski, 1998: Primary production of the biosphere: integrating terrestrial and oceanic components. *Science*, **281**, 237–40.

Fox-Kemper, B., G. Danabasoglu, R. Ferrari, S. M. Griffies, R. W. Hallberg, M. Holland, S. Peacock, and B. Samuels, 2011: Parameterization of mixed layer eddies. III: Implementation and impact in global ocean climate simulations. *Ocean Modell*., **39**, 61–78, doi:10.1016/j.ocemod.2010.09.002.

Frenz, M., R. Henrich, and B. Zychla, 2006: Carbonate preservation patterns at the Ceará Rise – Evidence for the Pliocene super conveyor. *Mar. Geol*., **232**, 173–180.

Ganachaud, A. and C. Wunsch, 2003: Large-scale ocean heat and freshwater transports during the World Ocean Circulation Experiment. *J. Climate*, **16**, 696–705.

Garcia, H. E., and L. I. Gordon, 1992: Oxygen solubility in seawater: Better fitting equations. *Limnology and Oceanography*, **37**, doi: 10.4319/lo.1992.37.6.1307.

——, R. A. Locarnini, T. P. Boyer, and J. I. Antonov, 2006a: Dissolved Oxygen, Apparent Oxygen Utilization, and Oxygen Saturation. *Vol. 3, World Ocean Atlas 2005*, S. Levitus, Ed., NOAA Atlas NESDIS 63, 342 pp.

——, ——, ——, and ——, 2006b: Nutrients (Phosphate, Nitrate, Silicate). *Vol. 4, World Ocean Atlas 2005*, S. Levitus, Ed., NOAA Atlas NESDIS 64, 396 pp.

Geider, R. J., H. L. MacIntyre, and T. M. Kana, 1997: A dynamic model of phytoplankton growth and acclimation: Responses of the balanced growth rate and chlorophyll a: Carbon ratio to light, nutrient-limitation and temperature. *Mar. Ecol. Prog. Ser*., **148**, 187–200.

Gent, P. R., and Coauthors, 2011: The Community Climate System Model version 4. *J.*

Climate, **24**, 4973–4991.

Gillett, N. P., V. K. Arora, H. D. Matthews, and M. R. Allen, 2013: Constraining the ratio of global warming to cumulative CO_2 emissions using CMIP5 simulations. *J. Climate*., **26**, 6844–6858.

Godfrey, J. S., 1989: A Sverdrup model of the depth-integrated flow for the World Ocean allowing for island circulations. *Geophys. Astrophys*. Fluid Dyn., **45**, 89–112.

Griffies, S. M., and Coauthors, 2009: Coordinated Ocean-ice Reference Experiments (COREs), *Ocean Model*., **26**, 1–46, doi:10.1016/j.ocemod.2008.08.007.

Groeneveld J., D. Nurnberg, S. Steph, R. Tiedemann, G. -J. Reichart, L. Reuning, D. Crudeli, 2008: The Pliocene Mg/Ca SST increase in the Caribbean: Western Atlantic Warm Pool formation, salinity influence or diagenetic overprint? *Geochem. Geophys. Geosyst.*, **9**(1), doi:10.1029/2006GC001564.

Guilyardi, E., 2006: El Niño–mean state–seasonal cycle interactions in a multi-model ensemble. *Climate Dyn.*, **26**, 329–348, doi:10.1007/s00382-005-0084-6.

Guilyardi, E., W. Cai, M. Collins, A. Fedorov, F. -F. Jin, A. Kumar, D. -Z. Sun, and A. Wittenberg, 2012: New strategies for evaluating ENSO processes in climate models. *Bull. Amer. Meteor. Soc*., **93**, 235–238, doi:https://doi.org/10.1175/BAMS-D-11-00106.1.

Hallberg, R., 1995: Some aspects of the circulation in ocean basins with isopycnals intersecting the sloping boundaries. Ph.D. thesis, University of Washington, 244 pp. [Available from University Microfilms, 1490 Eisenhower Place, P.O. Box 975, Ann Arbor, MI 48106.]

——, 2000: Time integration of diapycnal diffusion and Richardson number–dependent mixing in isopycnal coordinate ocean models. *Mon. Wea. Rev.*, **128**, 1402–1419.

——, 2003: The suitability of large-scale ocean models for adapting parameterizations of boundary mixing and a description of a refined bulk mixed layer model, Near-Boundary Processes and Their Parameterization: Proc. ʻAha Hulikoʻa Hawaiian Winter Workshop, Honolulu, HI, University of Hawaii at Manoa, 187–203.

Harrison, M. J. and R. W. Hallberg, 2008: Pacific subtropical cell response to reduced equatorial dissipation. *J. Phys. Oceanogr*., **38**, 1894–1912.

——, A. Adcroft, and R. Hallberg, 2014: Atlantic watermass and circulation response to persistent freshwater forcing in two coupled general circulation models. *Climate Dyn*., **42**(1-2), doi:10.1007/s00382-013-1798-5.

Haywood, A. M., P. J. Valdes, and V. L. Peck, 2007: A permanent El Niño–like state

during the Pliocene? *Paleoceanography*, **22**, PA1213, doi:10.1029/2006PA001323.

Haug, G. H. and R. Tiedemann, 1998: Effect of the formation of the Isthmus of Panama on Atlantic Ocean thermohaline circulation. *Nature*, **393**, 673-676, doi:10.1038/31447.

——, D. Sigman, R. Tiedemann, T. F. Pedersen, M. Sarnthein, 1999: Onset of permanent stratification in the subarctic Pacific Ocean. *Nature*, **401**, 779–782.

——, and L. D. Keigwin, 2004: How the Isthmus of Panama put ice in the Arctic. *Oceanus Magazine*, **42**(2), http://www.oceanusmag.whoi.edu.

——, R. Tiedemann, R. Zahn, and A. C. Ravelo, 2001: Role of Panama uplift on oceanic freshwater balance. *Geology*, **29**(3), 207-210, doi:10.1130/0091-7613.

Henson, S. A., J. P. Dunne, and J. L. Sarmiento, 2009: Decadal variability in North Atlantic phytoplankton blooms. *J. Geophys. Res*., **114**, C04013, doi:10.1029/2008JC005139.

Hodell D. A., and K. A. Venz-Curtis, 2006: Late Neogene history of deepwater ventilation in the Southern Ocean. *Geochemistry Geophys*. *Geosystems,* **7**, 1–16.

Hodell D. A., and K. A. Venz, 2013: Toward a high-resolution stable isotopic record of the Southern Ocean during the Pliocene-Pleistocene (4.8 to 0.8 Ma). *Antarct. Res. Ser*., **56**, 265–310.

Huang B., and Coauthors, 2015: Extended Reconstructed Sea Surface Temperature (ERSST), Version 4. NOAA National Centers for Environmental Information, doi:10.7289/V5KD1VVF [June 2017].

IPCC, 2013: Summary for Policymakers. *Climate Change 2013: The Physical Science Basis. Contribution of Working Group I to the Fifth Assessment Report of the Intergovernmental Panel on Climate Change*, Stocker, T. F., et al., Eds., Cambridge University Press, Cambridge, United Kingdom and New York, NY, USA, pp. 1–30, doi:10.1017/CBO9781107415324.004.

Ishman, S. E., 1996: A benthic foraminiferal record of middle to late Pliocene (3.15–2.85 Ma) deep water change in the North Atlantic. *Mar. Micropal*., **27**, 1656–1800, 1996.

Jochum, M., B. Fox Kemper, P. H. Molnar, and C. Shields, 2009: Differences in the Indonesian seaway in a coupled climate model and their relevance to Pliocene climate and El Niño. *Paleoceanography*, **24**, PA1212, doi:10.1029/2008PA001678.

Johns, W. E., and Coauthors, 2011: Continuous, array-based estimates of Atlantic Ocean heat transport at 26.5°N. *J. Climate*, **24**, 2429–2449.

Johnson, G. C., M. J. McPhaden, G. D. Rowe, and K. E. McTaggart, 2000: Upper equatorial Pacific Ocean current and salinity variability during the 1996– 1998 El Niño-La Niña cycle. *J. Geophys. Res*., **105**(C1), 1037– 1053.

——, B. M. Sloyan, W. S. Kessler, and K. E. McTaggart, 2002: Direct measurements of upper ocean currents and water properties across the tropical Pacific Ocean during the 1990s. *Prog. Oceanogr.*, **52**, 3 – 61.

Kamikuri, S. -I., I. Motoyama, H. Nishi, and M. Iwai, 2009: Evolution of Eastern Pacific Warm Pool and upwelling processes since the middle Miocene based on analysis of radiolarian assemblages: Response to Indonesian and Central American Seaways. *Palaeogeogr. Palaeoclimatol. Palaeoecol.*, **280**(3–4), 469–479, doi:10.1016/j.palaeo.2009.06.034.

Kamykowski, D., and S. J. Zentara, 1990: Hypoxia in the world ocean as recorded in the historical data set, Deep Sea Research Part A. *Oceanographic Research Papers*, **37**(12), 1861-1874.

Karas, C., D. Nürnberg, A. K. Gupta, R. Tiedemann, K. Mohan, and T. Bickert, 2009: Mid-Pliocene climate change amplified by a switch in Indonesian subsurface Throughflow. *Nat. Geosci*., **2**, 434–438, doi:10.1038/ngeo520.

Keigwin, L. D., 1982: Isotopic paleoceanography of the Caribbean and east Pacific: Role of Panama uplift in late Neogene time. *Science*, **217**, 350-353.

Key, R. M., and Coauthors, 2004: A global ocean carbon climatology: Results from Global Data Analysis Project (GLODAP). *Global Biogeochem. Cycles*, **18**, GB4031, doi:10.1029/2004GB002247.

Kirby, M.X. and B. MacFadden, 2005: Was southern Central America an archipelago or a peninsula in the middle Miocene? A test using land-mammal body size. *Palaeogeogr. Palaeoclimatol. Palaeoecol.*, **228**, 3–4, 193–202, doi:10.1016/j.palaeo.2005.06.002.

Kirtman, B. P., 1997: Oceanic Rossby wave dynamics and the ENSO period in a coupled model. *J. Climate*, **10**, 1690–1704.

Kirtman, B., and Coauthors, 2013: Near-term Climate Change: Projections and Predictability. *Climate Change 2013: The Physical Science Basis. Contribution of Working Group I to the Fifth Assessment Report of the Intergovernmental Panel on Climate Change*, Stocker, T.F. et al., Eds., Cambridge University Press, Cambridge, United Kingdom and New York, NY, USA, 953–1028, doi:10.1017/CBO9781107415324.023.

Klocker, A., M. Prange, and M. Schulz, 2005: Testing the influence of the Central American Seaway on orbitally forced Northern Hemisphere glaciation, *Geophys. Res. Lett*., **32**, L03703.

Knight, J. R., R. J. Allan, C. K. Folland, M. Vellinga, and M. E. Mann, 2005: A signature of persistent natural thermohaline circulation cycles in observed climate. *Geophys. Res. Lett*., **32**, L20708, doi:10.1029/2005GL024233.

Kosaka, Y., and S.- P. Xie, 2013: Recent global-warming hiatus tied to equatorial Pacific surface cooling. *Nature*, **501**, 403–407, doi:10.1038/nature12534 pmid:23995690.

Krasting, J. P., J. P. Dunne, R. J. Stouffer, and R. Hallberg, 2016: Enhanced Atlantic sea-level rise relative to the Pacific under high carbon emission rates. *Nat. Geosci*., **9**(3), doi:10.1038/ngeo2641.

Kuhnt, W., A. Holbourn, R. Hall, M. Žuvela, and R. Käse, 2004: Neogene history of the Indonesian Throughflow, in Continent-Ocean Interactions Within East Asia Marginal Seas. *Geophys. Monogr. Ser*., P. Clift, et al., Ed., AGU, Washington, D. C., vol. 149, pp. 299– 320,

Kushnir, Y., 1994: Interdecadal variations in North Atlantic sea surface temperature and associated atmospheric conditions. *J. Climate*, **7**, 141–157, doi:10.1175/1520-0442(1994)007,0141: IVINAS.2.0.CO;2.

LaRiviere, J. P., A. C. Ravelo, A. Crimmins, P. S. Dekens, H. L. Ford, M. Lyle, and M. W. Wara, 2012: Late Miocene decoupling of oceanic warmth and atmospheric carbon dioxide forcing. *Nature*, **486**(7401), 97–100, doi:10.1038/nature11200.

Lawrence, K. T., Z. Liu, and T. D. Herbert, 2006: Evolution of the eastern tropical Pacific through Plio-Pleistocene glaciation. *Science*, **312**, 79–83.

Levin, L. A., 2003: Oxygen minimum zone benthos: adaptation and community response to hypoxia. *Oceanogr. Mar. Biol., Annu. Rev*., **41**, 1-45.

Levitus, S., J. Antonov, and T. Boyer, 2005: Warming of the world ocean, 1955–2003. *Geophys. Res. Lett*., **32**, L02604, doi:10.1029/2004GL021592.

Lin, J. L., 2007: The double-ITCZ problem in IPCC AR4 coupled GCMs: Ocean–atmosphere feedback analysis. *J. Climate*, **20**, 4497–4525.

Lisiecki, L. E., and M. E. Raymo, 2005: A Pliocene-Pleistocene stack of 57 globally distributed benthic $\delta^{18}O$ records. *Paleoceanography*, **20**, PA1003.

Locarnini, R. A., A. V. Mishonov, J. I. Antonov, T. P. Boyer, and H. E. Garcia, 2006:

Temperature. *World Ocean Atlas 2005*, Vol. 1, NOAA Atlas NESDIS 61, 182 pp.

Lonsdale, P., and K. D. Klitgord, 1978: Structure and tectonic history of the eastern Panama Basin. *Geol. Soc. Amer. Bull.*, **89**, 981– 999.

Lunt, D. J., P. J. Valdes, A. Haywood, I. C. Rutt, 2008: Closure of the Panama Seaway during the Pliocene: implications for climate and Northern Hemisphere glaciation, *Climate Dyn.*, **30**(1), 1-18.

Lyle, M., 2003: Neogene carbonate burial in the Pacific Ocean, *Paleoceanography*, **18**(3), doi:10.1029/2002PA000777.

McKay R., and Coauthors, 2012: Antarctic and Southern Ocean influences on Late Pliocene global cooling. *Proc. Natl. Acad. Sci. USA*, **109**(17), 6423–6428.

Maier-Reimer, E., U. Mikolajewicz, and T. Crowley, 1990: Ocean general circulation model sensitivity experiment with an open Central American Isthmus. *Paleoceanography*, **5**(3), 349–366.

Manabe, S., and R. J. Stouffer, 1980: Sensitivity of a global climate model to an increase of CO_2 concentration in the atmosphere. *J. Geophys. Res*., **85**, 5529–5554.

——, and ——, 1988: Two stable equilibria of a coupled ocean-atmosphere model. *J. Climate,* **1**, 841-66.

Manucharyan, G., and A. Fedorov, 2014: Robust ENSO across climates with a wide range of mean east-west SST gradients. *J. Climate*, **27**, 5836–5850, doi:10.1175/JCLI-D-13-00759.1.

Marshall, L. G., 1985: Geochronology and land mammal biochronology of the transamerican faunal interchange. *The Great American Biotic Interchange*, F. G. Stehli and S. D. Webb, Eds., pp. 49–85, Springer, New York.

Masson-Delmotte, and Coauthors, 2013: Information from paleoclimate archives. *Climate Change 2013: The Physical Science Basis. Contribution of Working Group I to the Fifth Assessment Report of the Intergovernmental Panel on Climate Change*. T. F. Stocker et al., Eds., Cambridge University Press, 383-464, doi:10.1017/CBO9781107415324.013.

Mikolajewicz U., and E. Maier-Reimer, 1994: Mixed boundary conditions in ocean general circulation models and their influence on the stability of the models conveyor-belt. *J. Geophys. Res*., **99**, 22633–22644.

——, and T. Crowley, 1997: Response of a coupled ocean/energy balance model to restricted flow through the central American isthmus. *Paleoceanography*, **12**(3),

429–441.

——, E. Maier-Reimer, and T. Crowley, 1993: Effect of Drake Passage and Panamian gateways on the circulation of an ocean model. *Paleoceanography*, **8**, 409–426.

Milly, P. C. D., and Coauthors, 2014: An enhanced model of land water and energy for global hydrologic and earth-system studies. *J. Hydrometeor*., **15**(5), doi:10.1175/JHM-D-13-0162.1.

Mix A. C., N. G. Pisias, W. Rugh, J. Wilson, A. Morey, and T. K. Hagelberg, 1995: Benthic foraminifer stable isotope record from site 849 (0–5 Ma): local and global climate changes. *Proceedings of the Ocean Drilling Program*, N. G. Pisias, L. A. Mayer, T. R. Palmer-Julson, T. H. van Andel, Eds., **138**, ODP, 371–412.

Molnar, P., 2008: Closing of the Central American Seaway and the Ice Age: A critical review. *Paleoceanography*, **23**, PA2201, doi:10.1029/2007PA001574.

——, and M. A. Cane, 2002: El Niño's tropical climate and teleconnections as a blueprint for pre-Ice-Age climates. *Paleoceanography*, **17**(2), doi:10.1029/2001PA000663.

Montes, C., and Coauthors, 2012a: Arc-Continent Collision and Orocline Formation: Closing of the Central American Seaway. *J. Geophys. Res*., **117**, B04105, doi:10.1029/2011JB008959.

——, and Coauthors, 2012b: Evidence for middle Eocene and younger land emergence in central Panama: Implications for Isthmus closure. *Geol. Soc. Amer. Bull*., **124**(5–6), 780–799.

Moore, D. W. and S. G. H. Philander, 1977: Modeling the equatorial oceanic circulation. *The Sea*, Vol. VI, Wiley Interscience, New York, 319-361.

Morel, F. M. M., and R. J. M. Hudson, 1985: The geobiological cycles of trace elements in aquatic systems: Redfield revisited. *Chemical processes in lakes*, W. Stumm, Ed., 251-281. New York: Wiley-Interscience.

Motoi, T.,W. -L. Chan, S. Minobe, and H. Sumata, 2005: North Pacific halocline and cold climate induced by Panamanian Gateway closure in a coupled ocean-atmosphere GCM. *Geophys. Res. Lett.*, **32**, L10618, doi:10.1029/2005GL022844.

Mudelsee, M., and M. E. Raymo, 2005: Slow dynamics of the Northern Hemisphere glaciation. *Paleoceanography*, **20**, PA4022.

Murdock T., A. Weaver, A. Fanning, 1997: Paleoclimatic response of the closing of the Isthmus of Panama in a coupled ocean–atmosphere model. *Geophys. Res. Lett*.,

24(3), 253–256.

Naiman Z., P. J. Goodman, J. P. Krasting, S. L. Malyshev, J. L. Russell, R. J. Stouffer, and A. T. Wittenberg, 2017a: Impact of Mountains on Tropical Circulation in Two Earth System Models. *J. Climate*, **30**(11), 4149-4163.

——, A. S. Cohen, P. J. Goodman, J. P. Krasting, S. L. Malyshev, J. L. Russell, L. T. Sentman, R. J. Stouffer, and J. Yin, 2017b: Response of East African climate to global climate changes in a family of Earth System Models. [Manuscript in preparation.]

Najjar, R., and J. C. Orr, 1998: Design of OCMIP-2 simulations of chlorofluorocarbons, the solubility pump and common biogeochemistry. LSCE/CEA Saclay Internal OCMIP Rep., 25 pp.

——, and Coauthors, 2007: Impact of circulation on export production, dissolved organic matter and dissolved oxygen in the ocean: Results from Phase II of the Ocean Carbon-cycle Model Intercomparison Project (OCMIP-2). *Global Biogeochem. Cycles*, **21**, GB3007, doi:10.1029/2006GB002857.

Nathan, S. A., and R. M. Leckie, 2003: *Proc. ODP, Sci. Results*, W. L. Prell, P. Wang, P. Blum, D. K. Rea, S. C. Clemens, Eds., Ocean Drilling Program, College Station, TX, vol. 184, pp. 1-43.

——, and ——, 2009: Early history of the Western Pacific Warm Pool during the middle to late Miocene (~13.2-5.8 Ma): Role of sea-level change and implications for equatorial circulation. *Palaeogeogr. Palaeoclimatol. Palaeoecol*., **274**, 140.

Nisancioglu, K. H., M. E. Raymo, and P. H. Stone, 2003: Reorganization of Miocene deep water circulation in response to the shoaling of the Central American Seaway. *Paleoceanography*, **18**(1), 1006, doi:10.1029/2002PA000767.

Nof, D., 2000: Does the wind control the import and export of the South Atlantic? *J. Phys. Oceanogr.*, **30**, 2650–2667.

——, 2002: Is there a meridional overturning cell in the Pacific and Indian Oceans? *J. Phys. Oceanogr.*, **32**, 1947–1959.

——, and S. Van Gorder, 2003: Did an open Panama Isthmus correspond to an invasion of Pacific water into the Atlantic? *J. Phys. Oceanogr*., **33**, 1324–1336.

Oppo, D. W. and R. G. Fairbanks, 1987: Variability in the deep and intermediate water circulation of the Atlantic Ocean during the past 25,000 years: Northern Hemisphere modulation of the Southern Ocean. *Earth and Planet. Sci. Lett*., **86**, 1-15.

O'Reilly, C. H., M. Huber, T. Woollings, and L. Zanna, 2016: The signature of low-frequency oceanic forcing in the Atlantic Multidecadal Oscillation. *Geophys. Res. Lett*., **43**, 2810–2818, doi:10.1002/2016GL067925.

Osborne, A. H., D. R. Newkirk, J. Groeneveld, E. E. Martin, R. Tiedemann, and M. Frank, 2014: The seawater neodymium and lead isotope record of the final stages of Central American Seaway closure. *Paleoceanography*, **29**, 715–729, doi:10.1002/2014PA002676.

Philander, S.G. and Fedorov, A., 2003: Is El Niño Sporadic or Cyclic? *Annu. Rev. Earth Pl. Sc*., **31**, 579-594, doi:10.1146/annurev.earth.31.100901.141255.

Prange, M., and M. Schulz, 2004: A coastal upwelling seesaw in the Atlantic Ocean as a result of the closure of the Central American Seaway. *Geophys. Res. Lett*., **31**, L17207, doi:10.1029/2004GL020073.

Rahmstorf, S., 1995: Bifurcations of the Atlantic thermohaline circulation in response to changes in the hydrological cycle. *Climate Change*, **378**, 145–149.

——, 2002: Ocean circulation and climate during the past 120,000 years. *Nature*, **419**, 207-214.

Randall, D. A., and Coauthors, 2007: Climate models and their evaluation. *Climate Change 2007: The Physical Science Basis*. S. Solomon et al., Eds., Cambridge University Press, 589–662.

Ravelo, A. C., D. H. Andreasen, M. Lyle, A. O. Lyle, and M. W. Wara, 2004: Regional climate shifts caused by gradual global cooling in the Pliocene epoch. *Nature*, **429**, 263–267, doi:10.1038/nature02567.

Raymo, M. E., 1997: The timing of major climate terminations. *Paleoceanography*, **12**, p. 577-585.

——, W. F. Ruddiman, N. J. Shackleton, and D. Oppo, 1990: Evolution of Atlantic-Pacific $d^{13}C$ gradients over the last 2.5 m.y. *Earth and Planetary Science Letters*, **97**, p. 353-368.

——, D. Hodell, and E. Jansen, 1992: Response of deep ocean circulation to the initiation of northern hemisphere glaciation (3-2 M.Y.). *Paleoceanography*, **7**, p. 645-672.

Rayner, N. A., D. E. Parker, E. B. Horton, C. K. Folland, L. V. Alexander, D. P. Rowell, E. C. Kent, and A. Kaplan, 2003: Global analyses of sea surface temperature, sea ice, and night marine air temperature since the late nineteenth century. *J. Geophys. Res*., **108**, 4407, doi:10.1029/2002JD002670, D14.

Rhein, M., and Coauthors, 2013: Observations: Ocean. *Climate Change 2013: The*

Physical Science Basis. Contribution of Working Group I to the Fifth Assessment Report of the Intergovernmental Panel on Climate Change, Stocker, T. F., et al., Eds., Cambridge University Press, Cambridge, United Kingdom and New York, NY, USA.

Richter, I., S. -P. Xie, A. T. Wittenberg, and Y. Masumoto, 2012: Tropical Atlantic biases and their relation to surface wind stress and terrestrial precipitation. *Climate Dyn*., **38**, 985–1001, doi:10.1007/s00382-011-1038-9.

Rogers, A. D., 2000: The role of the oceanic oxygen minima in generating biodiversity in the deep-sea. *Deep-Sea Res*., **47**(1–2), 119–148, 2000.

Rousselle, G., C. Beltran, M. -A. Sicre, I. Raffi, and M. De Rafelis, 2013: Changes in sea-surface conditions in the Equatorial Pacific during the middle Miocene–Pliocene as inferred from coccolith geochemistry. *Earth Planet. Sci. Lett.* **361**, 412–421.

Rustic G. T., A. Koutavas, T. M. Marchitto, B. K. Linsley, 2015: Dynamical excitation of the tropical Pacific Ocean and ENSO variability by Little Ice Age cooling. *Science*, **350**(6267), 1537-1541, doi:10.1126/science.aac9937.

Sallée, J.B., E. Shuckburgh, N. Bruneau, A. J. Meijers, T. J. Bracegirdle, Z. Wang, and T. Roy, 2013: Assessment of Southern Ocean water mass circulation and characteristics in CMIP5 models: Historical bias and forcing response. *J. Geophys. Res.: Oceans*, **118**(4), 1830-1844.

Schiller, A., U. Mikolajewicz, and R. Voss, 1997: The stability of the North Atlantic thermohaline circulation in a coupled ocean-atmosphere general circulation model. *Climate Dyn*., **13**, 325-347.

Schmidt, D., 2007: *Marrying the Signal from Computer Models and Biological Proxies, Chapter: Deep time perspectives on climate change: an introduction*, Williams M., A. M. Haywood, F. J. Gregory, and D. N. Schmidt, Eds., The Micropalaeontological Society, Special Publications, The Geological Society, London, 1-5, doi:10.1144/TMS2.21.

Schmittner, A., N. Gruber, A. C. Mix, R. M. Key, A. Tagliabue, and T. K. Westberry, 2013: Biology and air–sea gas exchange controls on the distribution of carbon isotope ratios (δ^{13}C) in the ocean. *Biogeosciences*, **10**, 5793-5816, https://doi.org/10.5194/bg-10-5793-2013, 2013.

Schneider, B. and A. Schmittner, 2006: Simulating the impact of the Panamanian seaway closure on ocean circulation, marine productivity and nutrient cycling. *Earth and Planet. Sci. Lett*., **246**, 367–380.

Scroxton, N., S. G. Bonham, R. E. M. Rickaby, S. H. F. Lawrence, M. Hermoso, A. M.

Haywood, 2011: Persistent El Niño-Southern Oscillation variation during the Pliocene epoch. *Paleoceanography*, **26**, PA2215.

Seitzinger, S. P., J. A. Harrison, E. Dumont, A. H. W. Beusen, and A. F. Bouwman, 2005: Sources and delivery of carbon, nitrogen, and phosphorus to the coastal zone: An overview of Global Nutrient Export from Watersheds (NEWS) models and their application. *Global Biogeochem. Cycles*, **19**, GB4S01, doi:10.1029/2005GB002606.

Sepulchre, P., and Coauthors, 2014: Consequences of shoaling of the Central American Seaway determined from modeling Nd isotopes. *Paleoceanography*, **29**, doi:10.1002/2013PA002501.

Shackleton, N. J., S. Crowhurst, T. Hagelberg, N. G. Pisias, D. A. Schneider, 1995: A new late Neogene time scale: application to Leg 138 sites. *Proc. ODP, Sci. Results*, N. G. Pisias, L. A. Mayer, T. Janecek, A. Palmer-Julson, T. H. van Andel, Eds., Ocean Drilling Program, College Station, TX, vol. 138, pp. 73-101.

Shevliakova, E., S. W. Pacala, S. Malyshev, P. C. D. Milly, and L. T. Sentman, 2009: Carbon cycling under 300 years of land use change: Importance of the secondary vegetation sink. *Global Biogeochem. Cycles*, **23**, GB2022, doi:10.1029/2007GB003176.

Shipboard Scientific Party, 1991: Site 806. *Proc. ODP, Init. Repts*., L. W. Kroenke, W. H. Berger, T. Janecek, Eds., Ocean Drilling Program, College Station, TX, vol. 130, pp. 291-367.

——, 1992: Site 850. *Proc. ODP, Init. Repts*., L. Mayer, N. Pisias, T. Janecek, Eds., Ocean Drilling Program, College Station, vol. 138, pp. 809-889.

——, 2000: Site 1143. *Proc. ODP, Init. Repts.*, P. Wang, W. L. Prell, P. Blum, Eds., Ocean Drilling Program, College Station, TX, vol. 184, pp. 1-103.

Shyu, J. -P., D. Merrill, V. Hsu, M. A. Kaminski, C. M. Müller, A. J. Nederbragt, R. P. Scherer, and H. Shibuya, 1991: Biostratigraphic and magnetostratigraphic synthesis of the Celebes and Sulu seas, Leg 124. *Proc. ODP, Sci. Results*, E. A. Silver, C. Rangin, M. T. von Breyman, Eds., Ocean Drilling Program, College Station, TX, 1991, vol. 124, pp. 11-35.

Siegenthaler, U., and J. L. Sarmiento, 1993: Atmospheric carbon dioxide and the ocean. *Nature*, **365**, 119–125.

Sigman, D. M., and G. H. Haug, 2003: The biological pump in the past. *Treatise on Geochemistry*, **6**, 491–528.

Song, Z., M. Latif, W. Park, U. Krebs-Kanzow, and B. Schneider, 2016: Influence of

seaway changes during the Pliocene on tropical Pacific climate in the Kiel climate model: mean state, annual cycle, ENSO, and their interactions. *Climate Dyn*., **48**(11-12), 3725-3740, doi:10.1007/s00382-016-3298-x.

Srinivasan, M. S., D. K. Sinha, 1998: Early Pliocene closing of the Indonesian Seaway: evidence from north-east Indian Ocean and Tropical Pacific deep sea cores. *J. Asian Earth Sci*., **16**(1), 29–44.

Steph, S., R. Tiedemann, M. Prange, J. Groeneveld, D. Nürnberg, L. Reuning, M. Schulz, and G. H. Haug, 2006: Changes in Caribbean surface hydrography during the Pliocene shoaling of the Central American Seaway. *Paleoceanography*, **21**, PA4221, doi:10.1029/2004PA001092.

Steph, S., and Coauthors, 2010: Early Pliocene increase in thermohaline overturning: a precondition for the development of the modern equatorial Pacific cold tongue. *Paleoceanography*, **25**, PA2202, doi:10.1029/2008PA001645.

Stocker, T. F., 1998: The seesaw effect. *Science*, **282**, 61–62.

Stommel, H., 1961: Thermohaline Convection with Two Stable Regimes of Flow. *Tellus*, **13**, 224–230, doi:10.1111/j.2153-3490.1961.tb00079.x.

Stouffer, R. J., A. J. Weaver, and M. Eby, 2004: A method for obtaining pre-twentieth century initial conditions for use in climate change studies. *Climate Dyn*., **23**, 327–339.

Suarez, M. J., and P. S. Schopf, 1988: A delayed action oscillator for ENSO. *J. Atmos. Sci*., **45**, 3283-3287.

Sykes, L. R., W. R. McCann, and A. L. Kafka, 1982: Motion of Caribbean plate during last 7 million years and implications for earlier Cenozoic movements. *J. Geophys. Res*., **87**, 10656-10676.

Takahashi, K., and D. S. Battisti, 2007: Processes Controlling the Mean Tropical Pacific Precipitation Pattern. Part I: The Andes and the Eastern Pacific ITCZ. *J. Climate*, **20**(14), 3434–3451, doi:10.1175/JCLI4198.1.

Talley, L. D., 2003: Shallow, intermediate, and deep overturning components of the global heat budget. *J. Phys. Oceanogr*., **33**, 530–560.

Taylor, K. E., R. J. Stouffer, and G. A. Meehl, 2012: An overview of CMIP5 and the experiment design. *Bull. Amer. Meteor. Soc*., **93**, 485–498.

Teranes, J. L., D. H. Geary, and B. E. Bemis, 1996: The oxygen isotope record of seasonality in Neogene bivalves from the Central American Isthmus. *Evolution and Environment in Tropical America*, J. B. C. Jackson, A. F. Budd, and A. G. Coates, Eds., Univ. of Chicago Press, Chicago, Ill, 105–129.

Thiele, G., and J. L. Sarmiento, 1990: Tracer dating and ocean ventilation. *J. Geophys. Res*., **95** (C6), 9377–9391.

Tian, J., P. X. Wang, X. R. Cheng, Q. Y. Li, 2002: Astronomically tuned Plio-Pleistocene benthic delta O-18 record from South China Sea and Atlantic-Pacific comparison. *Earth Planet. Sci. Lett*., **203**, 1015.

Tiedemann R., and S. O. Franz, 1997: Deep-water circulation, chemistry, and terrigenous sediment supply in the equatorial Atlantic during the Pliocene, 3.3-2.6 Ma and 5-4.5 Ma. *Proc. Ocean Drill. Program, Sci. Results*, 154, 299–318.

Thompson, L., K. A. Kelly, D. Darr, and R. Hallberg, 2003: Buoyancy and mixed-layer effects on the sea surface height response in an isopycnal model of the North Pacific. *J. Phys. Oceanogr*., **32**, 3657–3670.

Timmermann A., S. I. An, U. Krebs, and H. Goosse, 2005: ENSO suppression due to weakening of the North Atlantic thermohaline circulation. *J. Climate*, **18**, 3122–3139.

——, and Coauthors, 2007: The Influence of a weakening of the Atlantic meridional overturning circulation on ENSO. *J. Climate*, **20**, 4899–4919.

Toggweiler, J. R., 2008: Origin of the 100,000-year timescale in Antarctic temperatures and atmospheric CO_2. *Paleoceanography*, **23**, PA2211, doi:10.1029/2006PA001405.

——, S. Carson, and R. Murnane, 2003: Representation of the carbon cycle in box models and GCMS: 2. Organic pump. *Global Biogeochem. Cycles*, **17**, doi:10.1029/2001GB001841.

Trenberth, K. E., 1976: Spatial and temporal variations of the Southern Oscillation. *Quart. J. Roy. Meteor. Soc.*, **102**, 639–653, doi:10.1002/qj.49710243310.

van Vuuren, D. P., J. Edmonds, M. Kainuma, and Coauthors, 2011: The representative concentration pathways: an overview. *Climatic Change*, **109**, 5, https://doi.org/10.1007/s10584-011-0148-z.

Vose, R. S., and Coauthors, 2012: NOAA's Merged Land-Ocean Surface Temperature Analysis. *Bull. Amer. Meteor. Soc*., **93**, 1677–1685, doi:10.1175/BAMS-D-11-00241.1.

Walker, J. C. G., P. B. Hays, and J. F. Kasting, 1981: A negative feedback mechanism for the long-term stabilization of Earth's surface temperature, *J. Geophys. Res*., **86**, 9776 – 9782, doi:10.1029/JC086iC10p09776.

Wara, M. W., A. C. Ravelo, and M. L. Delaney, 2005: Permanent El Niño-like conditions during the Pliocene warm period. *Science*, **309**, 758–761.

Watanabe, T., and Coauthors, 2011: Permanent El Niño during the Pliocene warm period not supported by coral evidence. *Nature*, **471**, 209–211.

Webb, S. D., 1985: Late Cenozoic of mammal dispersals between the Americas. *The Great American Biotic Interchange*, F. G. Stehli and S. D. Webb, Ed., pp. 357–386, Springer, New York.

——, and A. Rancy, 1996: Late Cenozoic evolution of the neotropical mammal fauna. *Evolution and Environment in Tropical America*, J. B. C. Jackson, A. F. Budd, and A. G. Coates, Ed., pp. 335–358, Univ. of Chicago Press, Chicago, Ill.

Whitmore Jr., F. C. and R. H. Stewart, 1965: Miocene mammals and Central American seaways. *Science*, **148**, 180–185.

Winton, M., 2000: A reformulated three-layer sea ice model. *J. Atmos. Oceanic Technol*., **17**, 525–531.

Wittenberg, A. T., 2002: ENSO response to altered climates. Ph.D. thesis, Princeton University, 462 pp.

——, A. Rosati, N. C. Lau, and J. J. Ploshay, 2006: GFDL's CM2 global coupled climate models. Part III: Tropical Pacific climate and ENSO. *J. Climate*, **19**, 698–722, doi:10.1175/JCLI3631.1.

——, 2009: Are historical records sufficient to constrain ENSO simulations? *Geophys. Res. Lett*., **36**, L12702, doi:10.1029/2009GL038710.

——, A. Rosati, N. -C. Lau, and J. J. Ploshay, 2006: GFDL's CM2 global coupled climate models. Part III: Tropical Pacific climate and ENSO. *J. Climate*, **19**, 698–722.

Wold, C. N., 1994: Cenozoic sediment accumulation on drifts in the northern North Atlantic. *Paleoceanography*, **9**(6), 917–941, doi:10.1029/94PA01438.

Woodruff, F. and S. M. Savin, 1989: Miocene deep-water oceanography. *Paleoceanography*, **4**, 87-140.

Xie, S. -P., 1994: On the genesis of the equatorial annual cycle. *J. Climate*, **7**, 2008–2013.

Yang, H. and F. Wang, 2009: Revisiting the Thermocline Depth in the Equatorial Pacific. *J. Climate*, **22**, 3856–3863, https://doi.org/10.1175/2009JCLI2836.1.

Yang, S., E. Galbraith, and J. Palter, 2013: Coupled climate impacts of the Drake Passage

and the Panama Seaway. *Climate Dyn*., **43**(37), doi:10.1007/s00382-013-1809-6.

Yin, J. and R. J. Stouffer, 2007: Comparison of the stability of the Atlantic thermohaline circulation in two coupled atmosphere-ocean general circulation models. *J. Climate*, **20**, 4293-4315.

Zhang, X., and Coauthors, 2012: Changes in equatorial Pacific thermocline depth in response to Panamanian seaway closure: Insights from a multi-model study. *Earth and Planet. Sci. Lett*., **317-318**, 76-84.

Zhang, Y. G., M. Pagani, Z. Liu, 2014: A 12-Million-Year Temperature History of the Tropical Pacific Ocean. *Science*, **344**(6179), 84-87, doi:10.1126/science.1246172.

Table 1.1. Details of paleoclimate proxy indicators from Ocean Drilling Program (ODP) sites referenced in this dissertation

Site	*Lat*	*Lon*	*Location*	*Water Depth (m)*	*References*
607	41°N	33°W	Central North Atlantic	3430	*Hodell and Venz-Curtis 2006*
659	18°N	21°W	Eastern equatorial Atlantic	3070	*Tiedemann et al. 1994*
704	47°S	7°E	Southern Ocean, Atlantic sector	2530	*Hodell and Venz 2013*
769	8°N	121°E	Equatorial Pacific western warm pool	3643	*Shyu et al. 1991*
806	0°	159°E	Equatorial Pacific western warm pool	2520	*Shipboard Scientific Party 1991* *Chaisson and Leckie 1993* *Nathan and Leckie 2009*
846	3°S	90°W	EEP cold tongue	3296	*Lawrence et al. 2006* *Scroxton et al. 2011*
847	0°	95°W	Equatorial Pacific cold tongue	3356	*Dekens et al. 2007* *Wara et al., 2005*
849	0°	110°W	Eastern equatorial Pacific	3851	*Mix et al. 1995*
850	1°N	110°W	Eastern Pacific cold tongue	3786	*Shipboard Scientific Party 1992* *Shackleton et al. 1995*
851	2°N	110°W	tropical eastern pacific	3761	*Cannariato and Ravelo 1997*
925	4°N	43°W	Western equatorial Atlantic	3040	*Billups et al. 1998* *Tiedemann and Franz 1997*
929	6°N	44°W	Western equatorial Atlantic	4370	*Billups et al. 1998* *Tiedemann and Franz 1997*
982	58°N	16°W	Eastern North Atlantic	1145	*Hodell and Venz-Curtis 2006*
999	13°N	79°W	Western Caribbean	2828	*Haug and Tiedemann 1998*
1143	9°N	113°E	Equatorial Pacific western warm pool	2774	*Shipboard Scientific Party 2000* *Nathan and Leckie 2003* *Tian et al. 2002*
1264	29°S	3°E	Southeast Atlantic	2505	*Bell et al. 2014*
U1338[a]	3°N	118°W	Eastern equatorial Pacific	4200	*Rousselle et al. 2013*

[a] Integrated Ocean Drilling Program

Table 1.2. Details of climate model simulations studying the role of the CAS on ocean circulation, climate, and marine biogeochemistry referenced in this dissertation[a]

Reference	*Model*	*Atmos. Res. (lat x lon)*	*Ocean Res. (lat x lon)*	*pCO_2 (ppmv)*	*CAS Width b (km)*	*CAS Depth (m)*	*Carbon Cycle*	*CAS Horizontal Depth-Integrated Net Mass Transport[c] (Sv)*
Maier-Reimer et al. (1990)	Hamburg-OGCM	Prescribed atm forcing	3.5˚x3.5˚ 11 levs	N/A	N/A	2711	No	10
Mikolajewicz et al. (1993)	Hamburg-OGCM	Prescribed atm forcing	3.5˚x3.5˚ 11 levs	N/A	N/A	2700 4100	No	N/A
Mikolajewicz and Crowley (1997)	Hamburg-OGCM	EBM	3.5˚x3.5˚ 22 levs	N/A	Altered frictional drag coefficient[d]		No	2.8-5.5
Murdock et al. (1997)	GFDL-OGCM	EMBM[c]	~1.8˚x1.8˚ 29 levs	N/A	588	3600	No	15.6
Nisancioglu et al. (2003)	MIT-OGCM	EBM	2.8˚x2.8˚ 15 levs	N/A	927	1000 2700	No	-10 17
Prange and Schulz (2004)	ECBILT-CLIOv3	~5.6˚x5.6˚ 3 levs	3.0˚x3.0˚ 20 levs	PI	1000	700	No	14
Motoi et al. (2005)	GFDL-R15	R15 9 levs	4.4˚x3.75˚ 12 levs.	N/A	1775	2559	No	N/A
Klocker et al. (2005)	ECBILT-CLIOv3	~5.6˚x5.6˚ 3 levs	3.0˚x3.0˚ 20 levs	PI	1000	700	No	14
Schneider and Schmittner (2006)	Uvic-ESCM v2.6	EMBM	1.8˚x3.6˚ 19 levs	PI	450	130 700 2000	Ocean only	5 10 10.6
Steph et al. (2006)	NCAR CCSM2.0.1 (paleo release)	3.75˚x3.75˚ 26 levs	3.6˚x1.6˚ 25 levs	PI	200	800	No	12
Lunt et al. (2008)	HadCM3	2.5˚x3.75˚ 19 levs	1.25˚x1.25˚ 20 levs	Pliocene 400	653	370	No	8
Steph et al. (2010)	ECBILT-CLIOv3	~5.6˚x5.6˚ 3 levs	3.0˚x3.0˚ 20 levs	PI	1000	700	No	14
Butzin et al. (2011)	Hamburg Ocean Carbon Cycle Model v2s	EBM	3.5˚ x3.5˚ 22 levs	PI	1143	250 500 1000 3000	Ocean only	6-12
Fedorov et al. (2013)	NCAR CESM	3.75˚x3.75˚	3.0˚x3.0˚ (1˚ at eq.)	PI	~1200	150 1100	No	N/A
Zhang et al. (2012)	CCSM3 KCM ECBILT-CLIOv3	~3˚x3˚, 26 levs ~3˚x3˚, 19 levs ~5.6˚x5.6˚, 3 levs	3.0˚x3.0˚, 25 levs 1.3˚x1.3˚, 31 levs 3.0˚x3.0˚, 20 levs	PI	1225 1633 1000	1475 1200 415	No	11 13 11
Yang et al. (2013)	CM2Mc	3.75˚x3.75˚ 24 levs	2.5˚x2.5˚ (0.6˚ at eq.) 28 levs	PI	~436	2000	Ocean only	17.8
This dissertation	**GFDL- ESM2G**	**2.0˚x2.5˚, 24 levs**	**1.0˚x1.0˚ (0.33˚ at eq.) 63 levs**	PI[e]	**109 1308 1308**	**1308 109 1308**	**Yes**	**20.5 14.1 23.1**

[a] "N/A" denotes details not reported by the study; OGCM-Ocean General Circulation Model; EBM-Energy Balance Model; EMBM-Energy Moisture Balance Model

[b] assuming 1º longitude = 109 km at 12º N

[c] positive values indicate Pacific to Atlantic transport

[d] varied frictional drag coefficient to simulate various CAS throughflow

[e] atmosphere CO_2 tracer restored annual and globally (Section 2.1)

Table 2.1. GFDL-ESM2G CAS experiment design

Simulation	*CAS Depth (m)*	*CAS Width (km)*	*CAS Configuration*	*CAS Net Mass Transport[c] (Sv)*
CLOSED	0	0	Modern/closed	0
NARROW	2000	109	Peninsula[a]	20.5
WIDESHALLOW	200	1308	Archipelago[b]	14.1
WIDE	2000	1308	Early shoaling	23.1

[a] Whitmore Jr. and Stewart (1965)
[b] Coates and Obando (1996)
[c] positive eastward (Pacific to Atlantic); vertically integrated

Table 3.1. GFDL-ESM2G global and hemispheric ocean physical mean state[a]

Simulation	***Meridional OHT at 30°N[b] (PW)***	***Meridional OHT at 30°S[b] (PW)***	***Meridional Salt Transport at 30°N[b] (10^6 kg s^{-1})***	***Meridional Salt Transport at 30°S[b] (10^6 kg s^{-1})***	***Global SST (°C)***	***Global SSS (psu)***	***Global 0-100 m Density (kg m^{-3})***
CLOSED	1.68	-0.52	-0.09	-0.06	17.89	34.13	1024.87
NARROW	1.56	-0.56	-0.20	-0.21	18.21	34.56	1025.12
WIDESHALLOW	1.60	-0.61	-0.51	-0.25	18.43	34.53	1025.05
WIDE	1.56	-0.63	-0.77	-1.64	18.45	34.61	1025.09

[a] 100-year annual average
[b] positive northward, negative southward; vertically integrated

Table 4.1. GFDL-ESM2G global and hemispheric atmosphere mean state[a]

Simulation	*Global SAT (K)*	*NH SAT[b] (K)*	*SH SAT[b] (K)*	*Global Precipitation Rate (mm day^{-1})*	*NH Precipitation Rate[b] (mm day^{-1})*	*SH Precipitation Rate[b] (mm day^{-1})*
CLOSED	286.4	286.4	286.5	2.958	2.946	2.970
NARROW	286.8 (+0.4)	286.2 (-0.2)	287.4 (+0.9)	2.979 (+0.02)	2.877 (-0.07)	3.082 (+0.11)
WIDESHALLOW	287.1 (+0.7)	286.4 (0)	287.7 (+1.2)	2.997 (+0.04)	2.877 (-0.07)	3.116 (+0.15)
WIDE	287.1 (+0.7)	286.3 (-0.1)	287.8 (+1.3)	2.996 (+0.04)	2.858 (-0.09)	3.134 (+0.16)
RCP2.6[c]	+0.8	+1.1	+0.5	+0.03	+0.05	+0.01

[a] 100-year annual average; values in parenthesis indicate difference between the open seaway and CLOSED
[b] Northern Hemisphere (NH; 0-90°N) and Southern Hemisphere (SH; 0-90°S) average
[c] GFDL-ESM2G CMIP5 2006-2100 projection simulation using the RCP2.6 emission scenario (van Vuuren et al. 2011); 20-year annual average differences between the model simulation with RCP2.6 emission scenario and the corresponding preindustrial control

Table 4.2. GFDL-ESM2G Southern Hemisphere extratropical mean climate[a]

Simulation	*SST (°C)*	*Sea ice cover (%)*	*2-m surface air temperature (°C)*	*Outgoing shortwave flux at the surface (W m^{-2})*	*Low cloud cover (%)*
CLOSED	4.9	5.4	4.0	23.2	53
NARROW	6.1	2.7	5.3	21.2	51
WIDESHALLOW	6.6	2.2	5.7	20.9	50
WIDE	6.7	1.6	5.9	20.6	50

[a] 100-year annual 30-90°S average (25% of global area)

Table 4.3. GFDL-ESM2G tropical ocean physical mean state

Simulation	*20ºN-20ºS SST[a] (°C)*	*20ºN-20ºS 0-300 m Temp[a] (°C)*	*20ºN-20ºS Depth of 20°C Isotherm[a] (m)*	*Niño-3 Min. SST[b] (°C)*	*Niño-3 Max. SST[b] (°C)*	*Niño3 SST Skewness[b] (°C)*
CLOSED	25.9 ± 1.69	17.3 ± 2.68	111 ± 48.5	-5.07	3.39	-0.30
NARROW	26.2 ± 1.65	17.7 ± 2.65	116 ± 49.9	-6.16	3.36	-0.66
WIDESHALLOW	26.3 ± 1.66	17.8 ± 2.68	119 ± 50.7	-4.99	4.08	-0.50
WIDE	26.4 ± 1.66	18.1 ± 2.67	122 ± 52.4	-6.30	4.25	-0.60

[a] 100-year monthly 20°N-20°S average
[b] 500-year monthly Niño-3 region (5°N-5°S, 150-90°W) average

Table 4.4. GFDL-ESM2G equatorial Pacific meridional and zonal temperatures

Simulation	*2°N-2°S average*				*110°W slice*			
	WP[a]		EP[a]		0-2°N		0-2°S	
	SST (°C)	Max. *dT/dz* Depth (m)	SST (°C)	Max. *dT/dz* Depth (m)	SST (°C)	Max. *dT/dz* Depth (m)	SST (°C)	Max. *dT/dz* Depth (m)
CLOSED	26.7	158.9	26.8	102.7	22.5	72.2	22.1	72.2
NARROW	27.2	155.7	27.2	100.3	22.8	74.1	22.5	77.4
WIDESHALLOW	27.3	163.4	27.4	103.7	22.4	78.3	22.4	80.3
WIDE	27.2	160.8	27.3	102.4	22.5	80.3	22.4	80.3

[a] 100-year annual West Pacific (WP; 140°E-155°W) and East Pacific (EP; 155-90°W) average

Table 5.1. GFDL-ESM2G global ocean biogeochemical mean state[a]

Simulation	Ave. ideal age (yrs)	Ave. Max. Mixed-Layer Depth (m)	Total Alkalinity (PgC)	Total DIC (PgC)	Surface Sediment $CaCO_3$ Inventory (PgC)	Surface Sediment $CaCO_3$ Burial Flux[b] (PgC a^{-1})	Long-Term Ocean Surface Sediment $CaCO_3$ Burial Flux[b,e] (PgC a^{-1})	Ocean Surface Sediment $CaCO_3$ Inventory[f] (PgC)	Air-sea CO_2 Flux[b] (PgC a^{-1})	Time Integrated Air-sea CO_2 Flux[b,d] (PgC)	Atmos. pCO_2 Flux From Land and Ocean[c] (PgC a^{-1})	Time Integrated Atmos. pCO_2 Flux From Land and Ocean[c,d] (PgC)
CLOSED	524.0	51.6	38909	36895	645.2	0.077	0.1589	791.7	-0.01	3.84	-0.098	-5.32
NARROW	476.3	54.5	38899	36685	611.0	0.076	0.1604	839.5	-0.2	-251.7	0.098	240.7

[a] 100-year annual averages and totals
[b] positive values indicate downward flux
[c] positive values indicate upward flux
[d] integrated total flux after 1400 integration years
[e] long-term (~100 kyr) values obtained from combining GFDL-ESM2G and Dunne et al. (2012a) $CaCO_3$ metamodel
[f] after 4000 GFDL-ESM2G integration years

Table 5.2. GFDL-ESM2G global ocean nutrients and productivity[a]

Simulation	*NO_3^- Inventory (PgN)*	*NO_3^- Inventory 0-100 m (PgN)*	*NO_3^- Inventory Below 100 m (PgN)*	*Total NPP from NO_3^- (PgC a^{-1})*	*Total NPP From NO_3^- 0-100 m (PgC a^{-1})*	*Total NPP From NO_3^- Below 100 m (PgC a^{-1})*	*PO_4^{3-} Inventory (PgP)*	*Total NPP from PO_4^{3-} (PgC a^{-1})*
CLOSED	442.7	2.92	439.6	72.4	67.1	5.36	89.2	71.2
NARROW	505.8	3.14	504.6	68.5	62.6	5.90	89.3	65.3

[a] 100-year annual average; vertically integrated

Table 5.3. GFDL-ESM2G inter-basin carbonate state[a]

Simulation	*Ave. Ocean Ideal Age (yr)*		*O_2 Inventory (PgO_2)*		*DIC Inventory (PgC)*		*Alkalinity Inventory (PgC)*		*Surface Sediment $CaCO_3$ Inventory (PgC)*		*Long-Term Surface Sediment $CaCO_3$ Burial Flux[b] ($PgC\ a^{-1}$)*		*Long-Term Surface Sediment $CaCO_3$ Burial Flux[b,c] ($gC\ m^{-2}a^{-1}$)*	
	ATL	**PAC**	**ATL**	**PAC**	**ATL**	**PAC**	**ATL**	**PAC**	**ATL**	**PAC**	**ATL**	**PAC**	**CAR**	**PAC**
CLOSED	250.0	727.8	1242	1747	8992	19694	9672	20510	230.9	224.4	0.061	0.049	1.25	0
NARROW	234.6	679.1	1197	2160	9077	19426	9699	20460	214.4	218.5	0.056	0.061	0.63	0.51

[a] 100-yr annual average for Atlantic (ATL) and Pacific (PAC) basins

[b] long-term (~100 kyr) values obtained from combining GFDL-ESM2G and Dunne et al. (2012a) $CaCO_3$ box model

[c] Point locations: Caribbean (CAR) calculated from ODP site 999 (12º44'N, 78º44'W, Colombian basin, water depth 2828 m, Table 1.1); PAC calculated from ODP site 846 (3°06'S, 90°49'W, tropical Pacific, 3307 m water depth, Table 1.1)

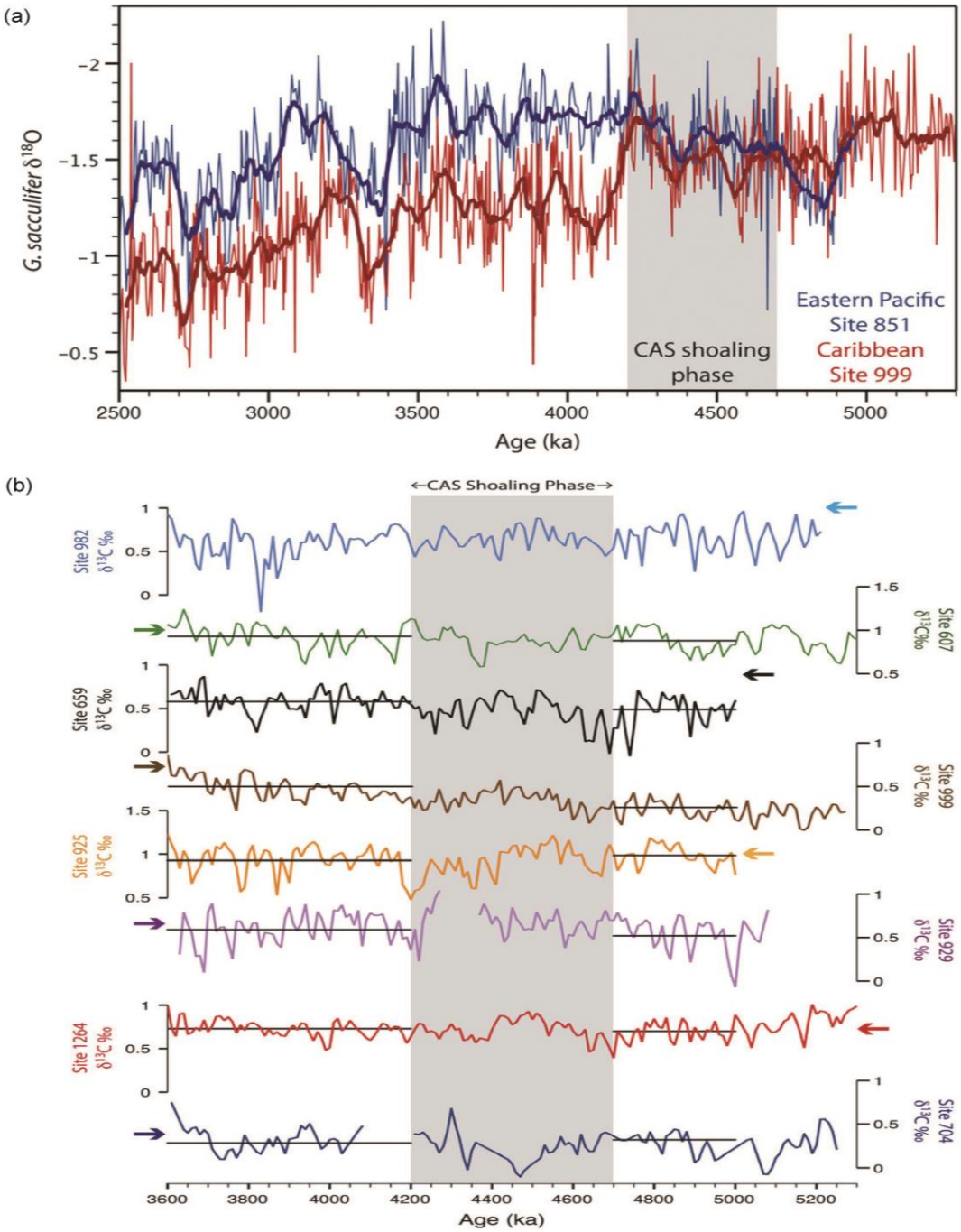

Fig. 1.1. (a) Comparison of surface water (planktic) oxygen isotope records (‰ vs Vienna Pee Dee Belemnite) from the Caribbean (ODP Site 999; Haug and Tiedemann 1998) and the eastern Pacific (ODP site 851; Cannariato and Ravelo 1997) for 2.2-5.3 Ma

showing an increased gradient between ~4.7-4.2 Ma attributed to a major shoaling phase of the CAS (grey shading), reprinted from "Atlantic Deep-water Response to the Early Pliocene Shoaling of the Central American Seaway" by Bell et al. (2015) licensed under *CC-BY-4.0*. Bold lines represent 50 kyr running averages (Haug et al. 2001; Fig. 2A). **(b)** Time series of δ^{13}C data (‰ vs Vienna Pee Dee Belemnite) from various Atlantic ODP sites, reprinted from "Atlantic Deep-water Response to the Early Pliocene Shoaling of the Central American Seaway" by Bell et al. (2015) licensed under *CC-BY-4.0*. Horizontal black lines show average δ^{13}C values for the time slice intervals prior to (5.0-4.7 Ma) and after (4.2-3.6 Ma) CAS shoaling. Arrows indicate approximate modern δ^{13}C values at each site. ODP site details are included in Table 1.1.

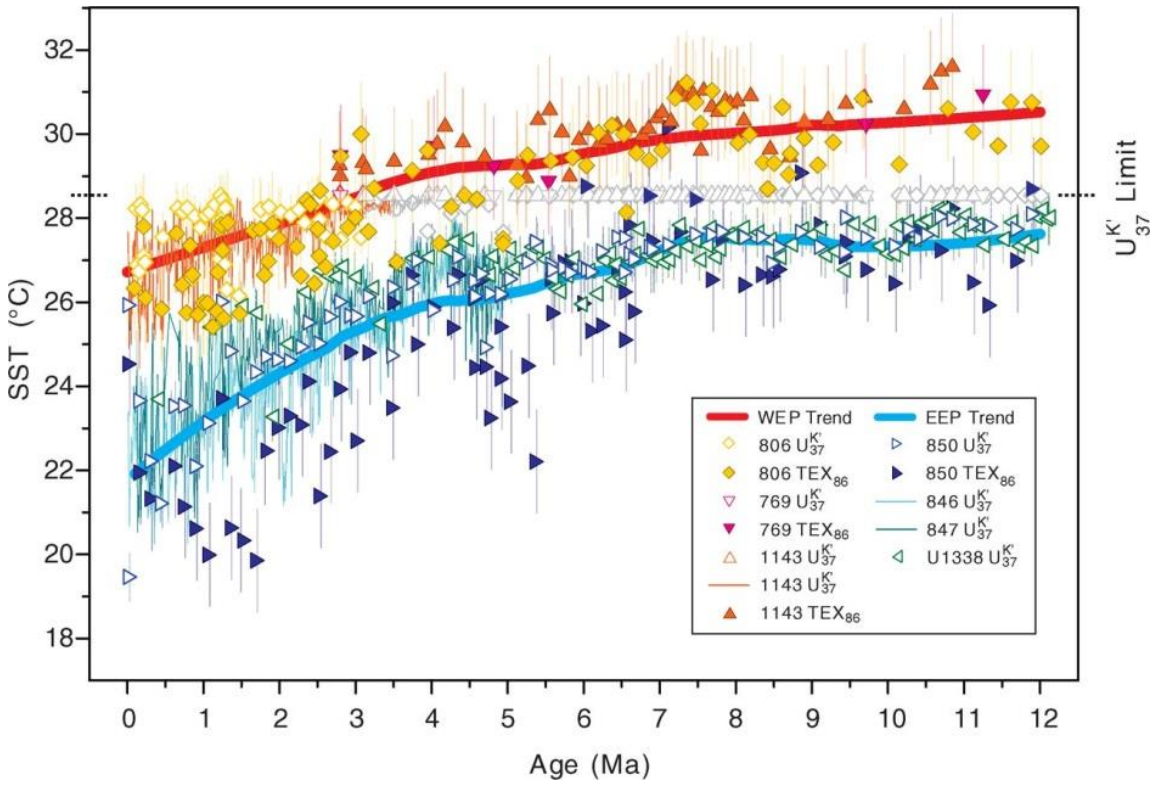

Fig. 1.2. Temperature evolution of the western and eastern equatorial Pacific since 12 Ma. Republished with permission of American Association for the Advancement of Science, from "A 12-Million-Year Temperature History of the Tropical Pacific Ocean", Zhang, Y. G., M. Pagani, and Z. Liu, *Science*, 344(6179), 2014.

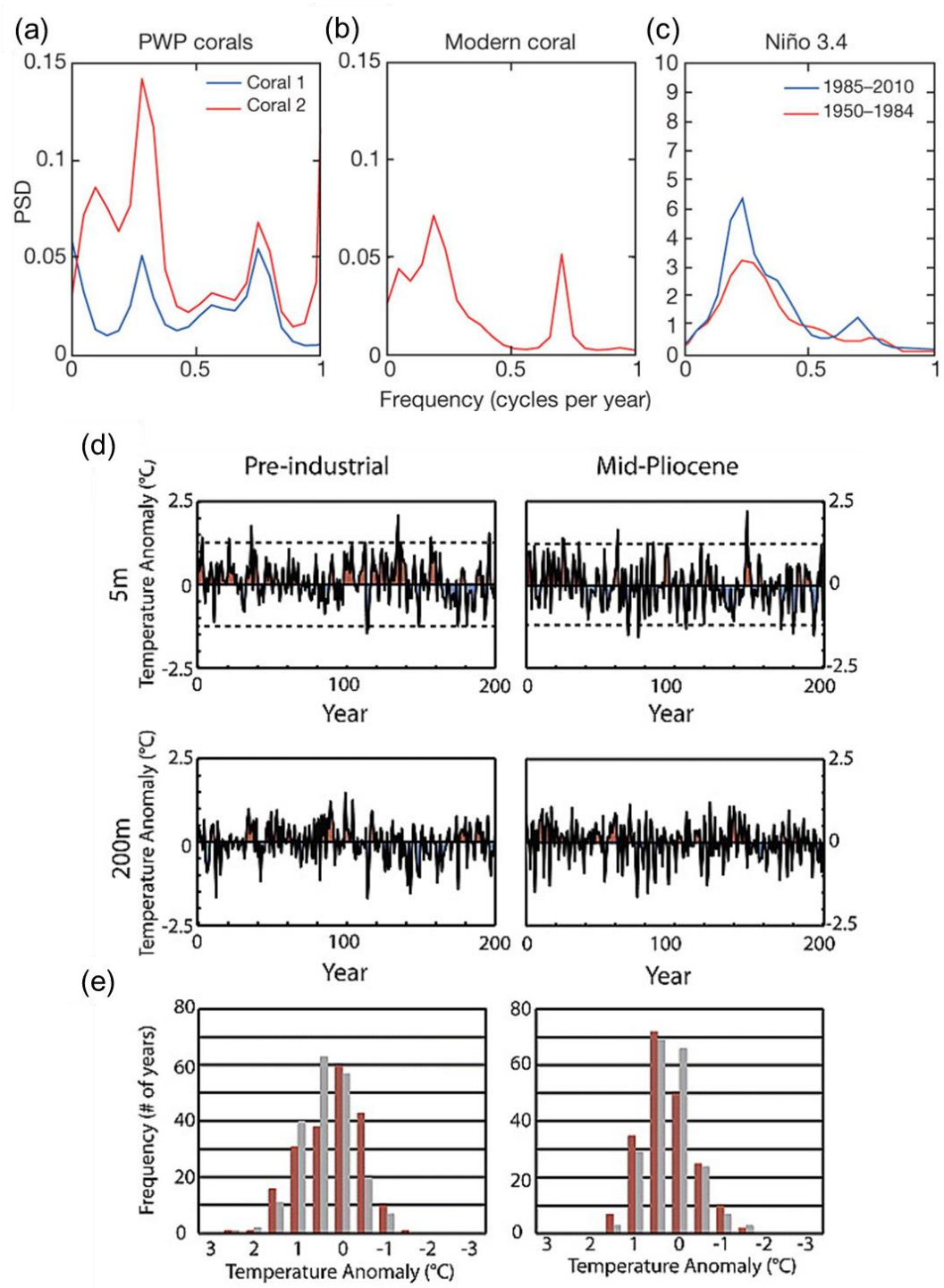

Fig. 1.3. (a) Power spectral densities (PSDs) estimated by the maximum-entropy method for PWP fossil corals (blue, coral 1; red, coral 2; Watanabe et al. 2011[1]), **(b)** modern coral $d^{18}O$ (Watanabe et al. 2011[1]), **(c)** the Niño 3.4 index (red, 1950–1984; blue, 1975–

2010; Scroxton et al. 2011[2]), **(d)** ENSO Index plots for March, April, and May mean (MAM) at ODP site 846 from HadCM3 running (*left*) preindustrial and (*right*) mid-Piacenzian Warm Period (mPWP; PRISM interval 3.264–3.025 Ma) simulations at two different depths, 5 m (*top*) and 200 m (*middle*; Scroxton et al. 2011[2]), and **(e)** frequency of SST anomalies over the 200 year time series at 5 m and 200 m depth (grey, preindustrial; red, mPWP; Scroxton et al. 2011[2]). ODP site details are included in Table 1.1. [1] Reprinted by permission from Macmillan Publishers Ltd: Nature, Watanabe, T., and Coauthors, Permanent El Niño during the Pliocene warm period not supported by coral evidence, 471, 209–211, copyright 2011. [2] Reprinted with permission from "Persistent El Niño-Southern Oscillation variation during the Pliocene Epoch" by Scroxton et al. (2011) licensed under *CC-BY-3.0*.

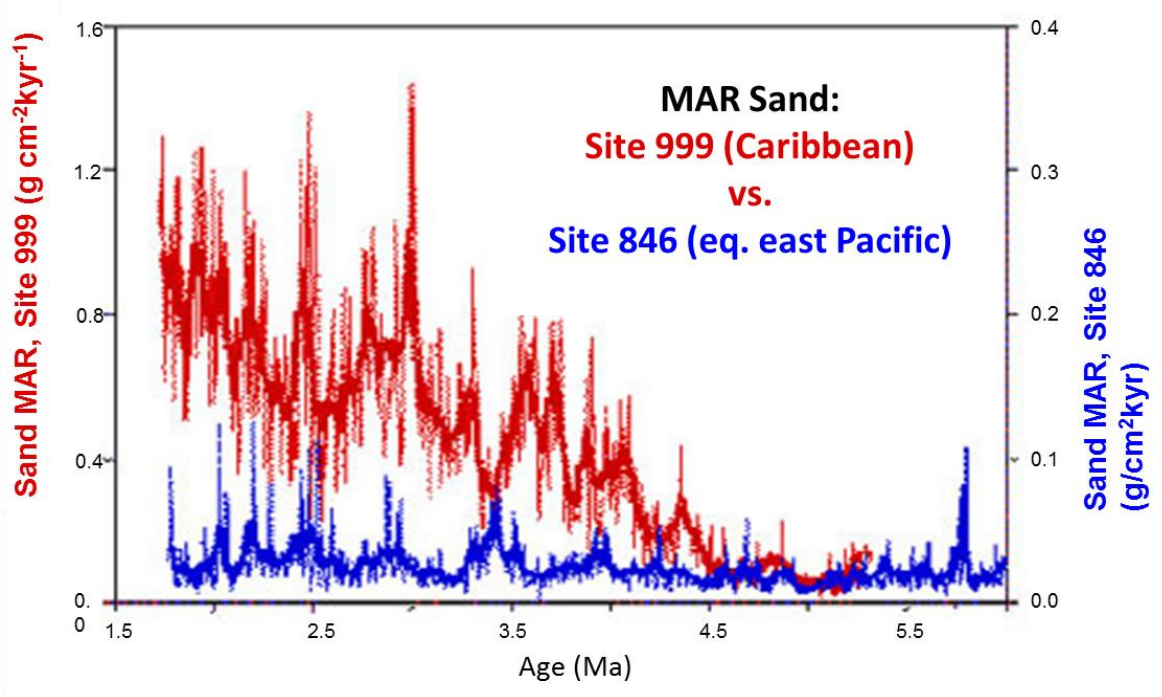

Fig. 1.4. Carbonate sand-fraction mass accumulation rates (sand MAR) at ODP sites 999 (Colombian basin, *left axis*) and 846 (eastern tropical Pacific basin, *right axis*) for 2–5.3 Ma. Reprinted by permission from Macmillan Publishers Ltd.: Nature Publishing Group (Haug and Tiedemann, Nature, 393, 674-676, copyright 1998).

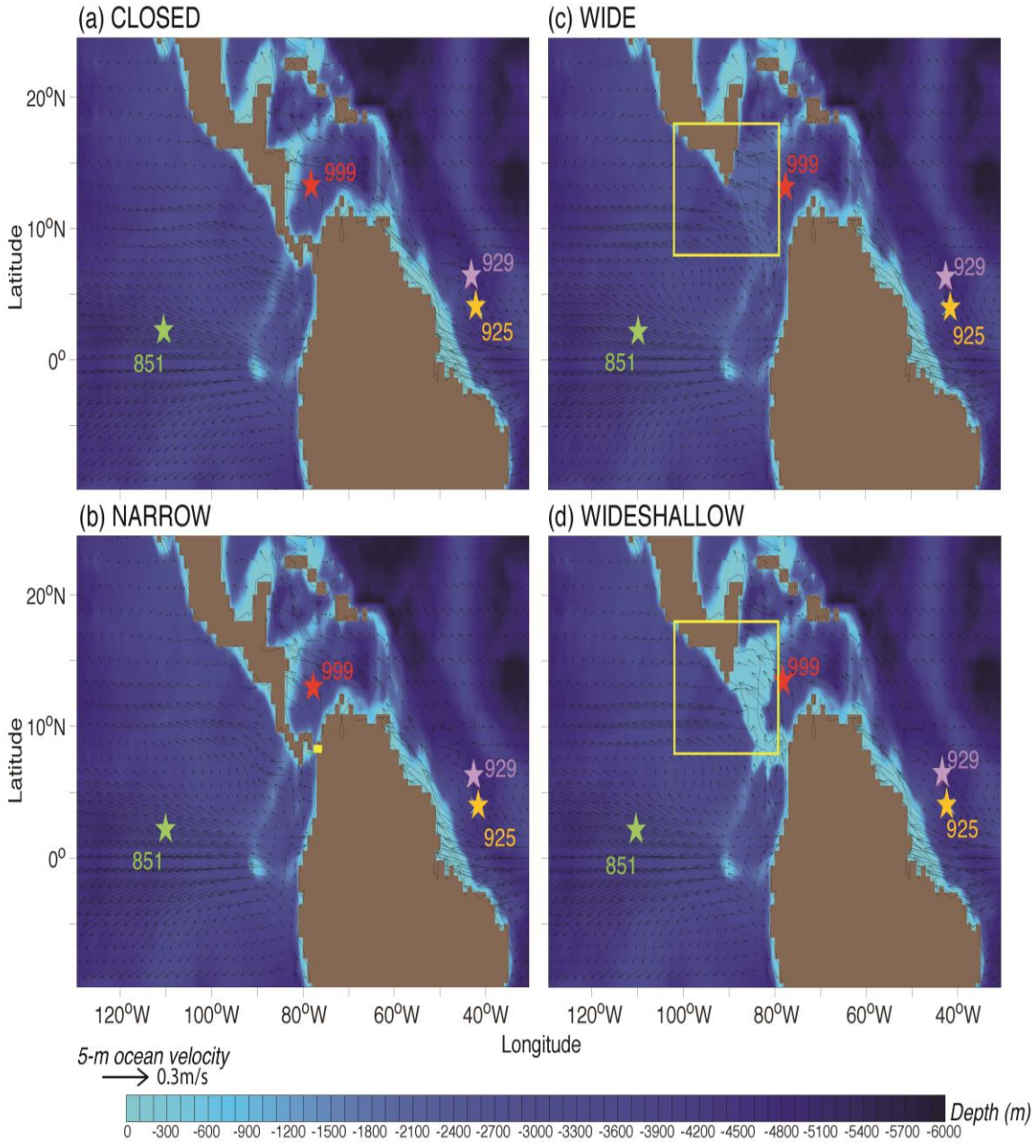

Fig. 2.1. GFDL-ESM2G bathymetry (m; shaded) for **(a)** CLOSED, **(b)** NARROW, **(c)** WIDE, and **(d)** WIDESHALLOW seaway simulations and 5-m ocean velocity (m s^{-1}; vectors). Stars show locations of local ODP drilling sites 999 (red), 851 (green), 929 (purple) and 925 (yellow) referenced in Fig. 1.1 and Fig. 1.4. The yellow boxes (18º-8ºN; 100º-77 ºW) in **(c)** and **(d)** and transect (77.5ºW; 8.2ºN) in **(b)** were used for the

WIDE/WIDESHALLOW and NARROW transport calculations (Section 3.3), respectively. See Table 2.1 for the GFDL-ESM2G CAS experiment widths and depths. ODP site details are included in Table 1.1.

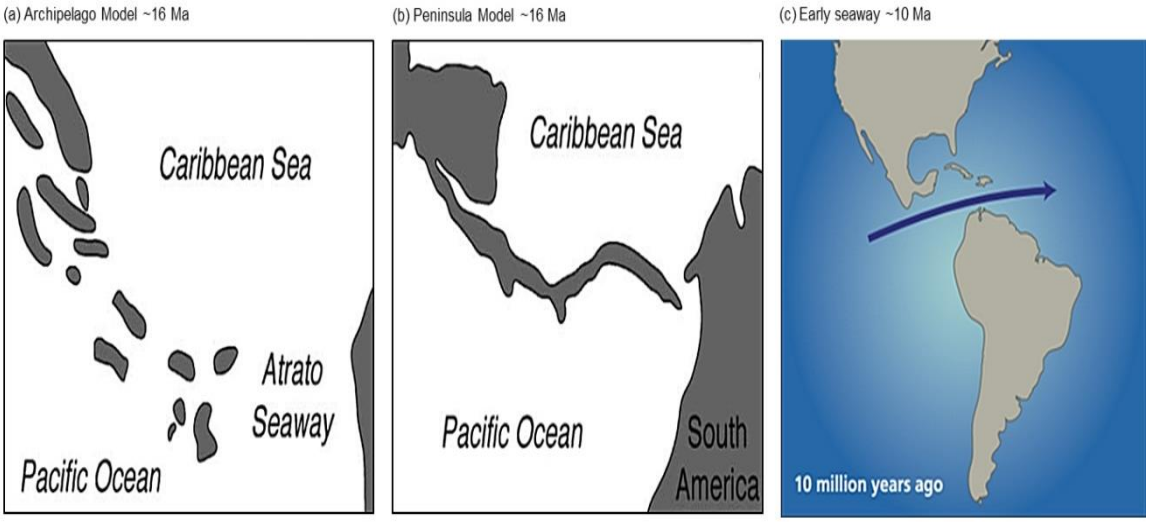

Fig. 2.2. Paleogeography reconstructions of Central America in the mid-Miocene before the Isthmus of Panama; **(a)** archipelago model (Coates and Obando 1996) reprinted from (Kirby and MacFadden 2005) with permission from Elsevier[1], **(b)** peninsula model (Whitmore and Stewart 1965) reprinted from (Kirby and MacFadden 2005) with permission from Elsevier[1], and **(c)** early seaway model similar to climate models (Table 1.2), republished with permission of *Oceanus Magazine*, from "How the Isthmus of Panama put ice in the Arctic", G. H. Haug and L. D. Keigwin, 42, 2, 2004; permission conveyed through Copyright Clearance Center, Inc. Emergent land is represented by gray **(a)** and **(b)** and tan **(c)**. Timing and structure of the paleogeography is uncertain (Kirby and MacFadden 2005). [1]**(a)** and **(b)** reprinted from *Palaeogeogr. Palaeoclimatol. Palaeoecol.*, M.X. Kirby and B. MacFadden. "Was southern Central America an archipelago or a peninsula in the middle Miocene? A test using land-mammal body size", Vol. 228, No. 3-4, p. 193–202, 2005, Copyright Elsevier with permission from Elsevier.

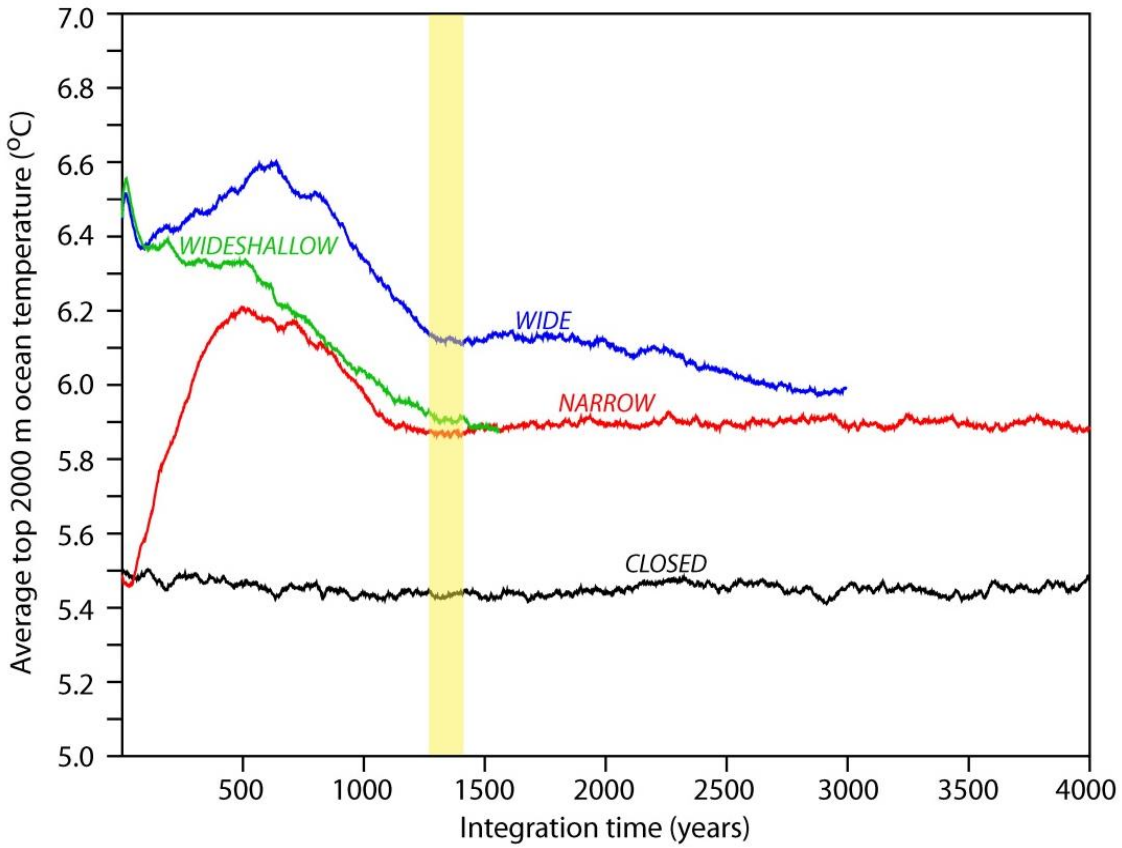

Fig. 2.3. GFDL-ESM2G global average upper 2000-m ocean temperature (°C) for the CLOSED (black), NARROW (red), WIDESHALLOW (green), and WIDE (blue) seaway simulations for model integration years 1-4000. The yellow shading represents the 100-year analysis period (1301-1400) mainly used in this study (except for the maximum Atlantic Meridional Overturning Circulation analysis). The wide seaway experiments (e.g., WIDE and WIDESHALLOW) began with a warmer global integrated ocean and average surface air temperature than the NARROW seaway experiment because more land grid cells were replaced with warm, tropical ocean grid cells than in the NARROW seaway. The global average upper 2000-m ocean temperature for the WIDESHALLOW seaway converges toward the NARROW simulation faster than the WIDE simulation that

was initialized with additional warm ocean grid cells. The NARROW and WIDE simulations were integrated longer than the spin-up and analysis periods to assess the convergence rate. The WIDE simulation converges toward the NARROW simulation at a rate of approximately 0.1˚C / 1000 years, requiring an additional 1000 integration years for near-convergence.

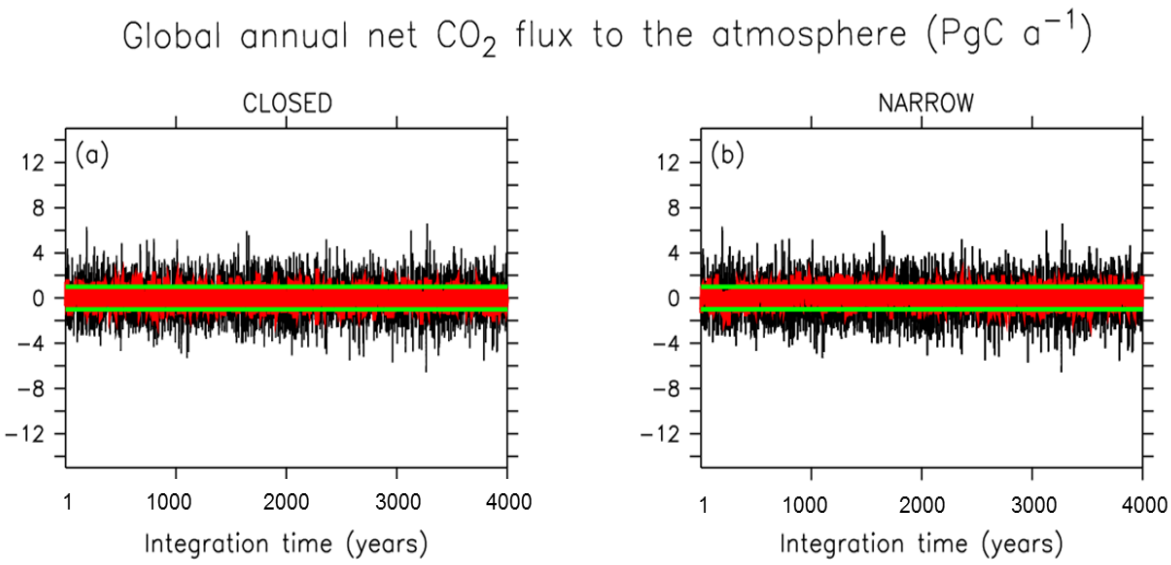

Fig. 2.4. Global annual (black) average atmosphere pCO_2 flux from the land and ocean (PgC a^{-1}) for the **(a)** CLOSED and **(b)** NARROW GFDL-ESM2G seaway simulations. 5-year boxcar smoothing is applied (red) to the annual average values (black). Green lines indicate ±1 PgC a^{-1} for evaluation of quasi-equilibrium via the CMIP5 criteria defined in Dunne et al. (2012b).

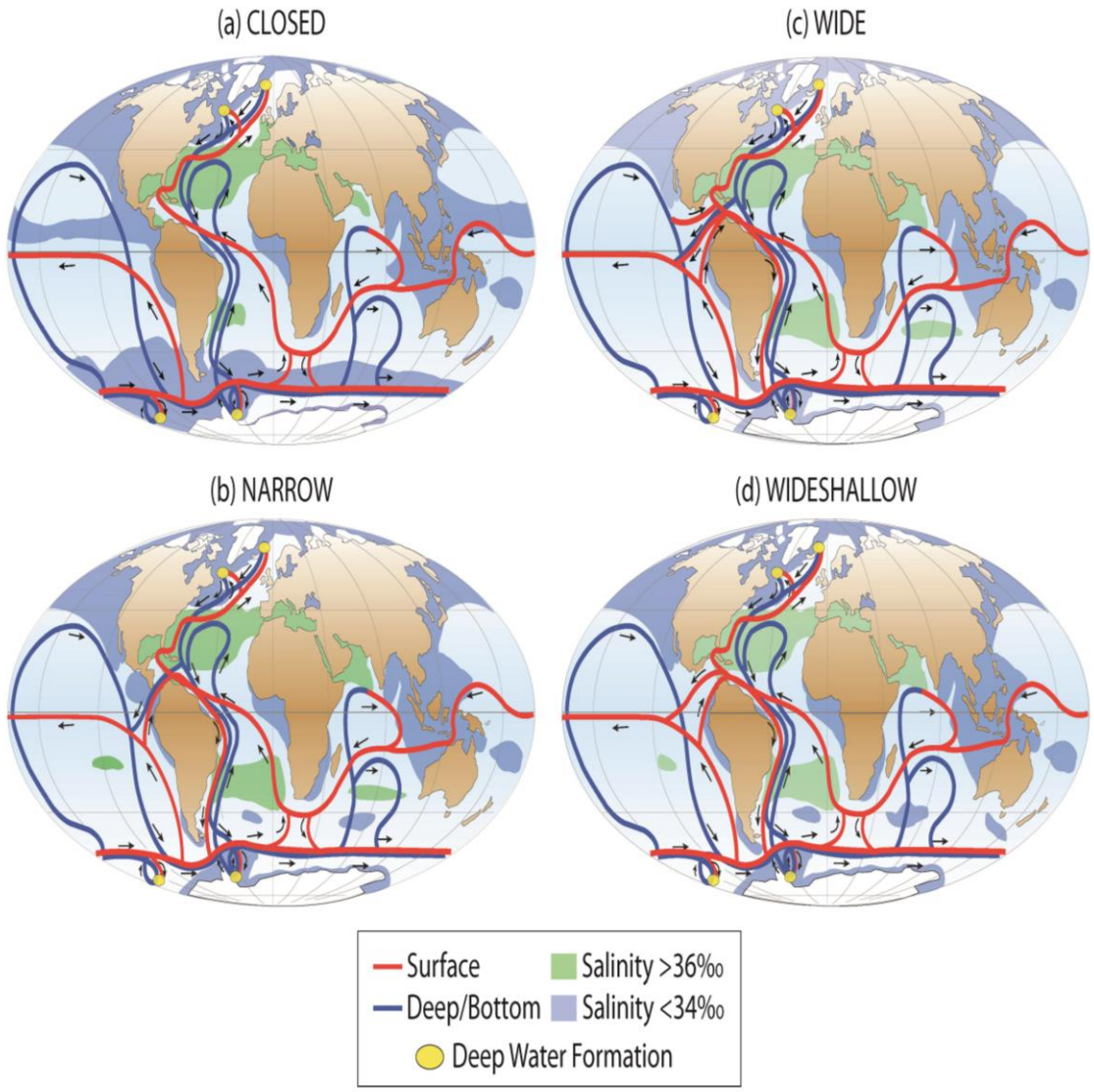

Fig. 3.1. Simplified GFDL-ESM2G global ocean circulation (modified from Rahmstorf (2002)) for the **(a)** CLOSED, **(b)** NARROW, **(c)** WIDE, and **(d)** WIDESHALLOW seaway simulations. Red (blue) lines indicate surface (deep/bottom) waters. Yellow ovals indicate deep-water formation regions. Shading represents regions with salinity > 36 psu (green) and < 34 psu (blue).

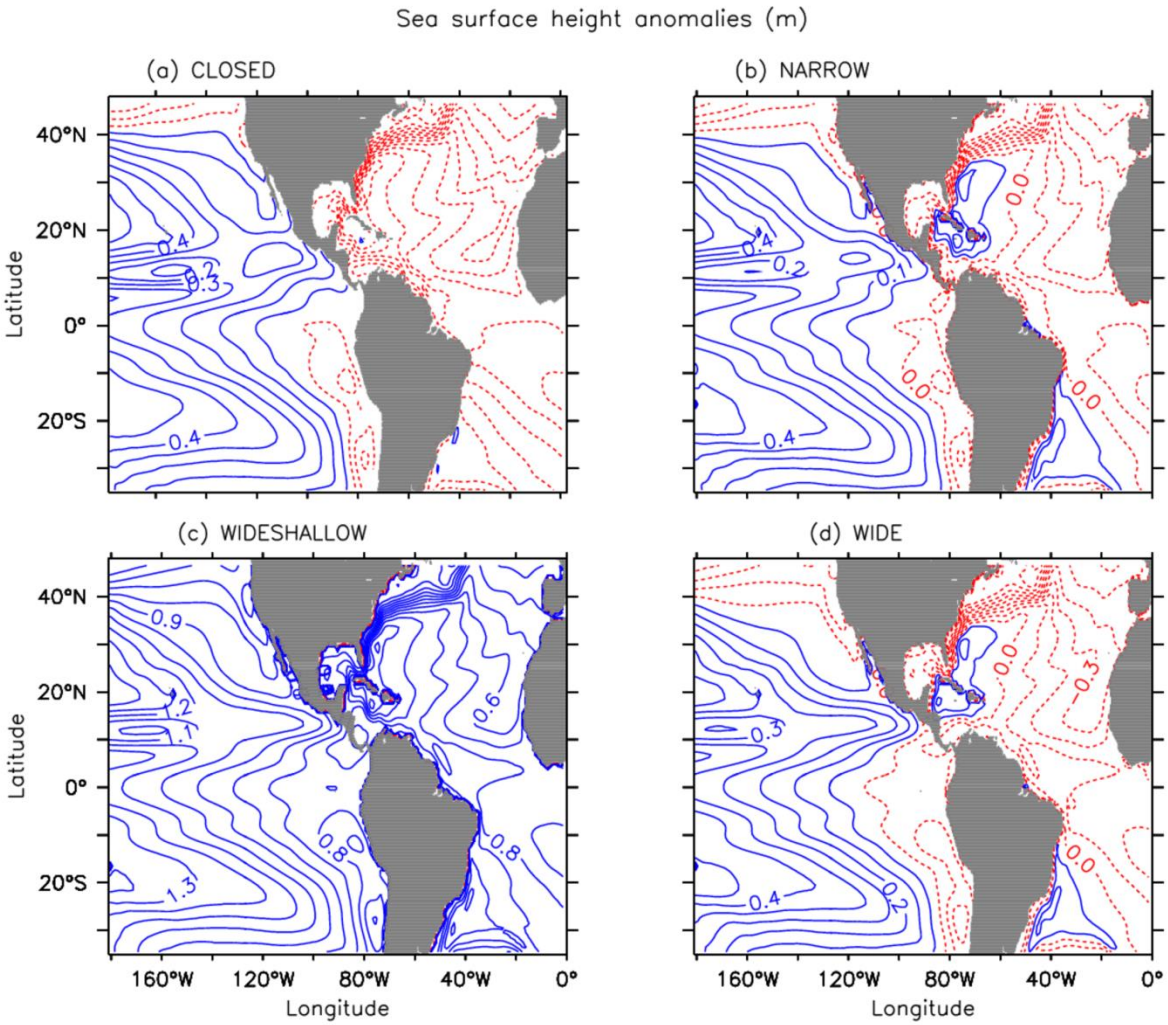

Fig. 3.2. Sea surface height (SSH) anomalies (m) relative to the global mean for the **(a)** CLOSED, **(b)** NARROW, **(c)** WIDESHALLOW, and **(d)** WIDE GFDL-ESM2G seaway simulations. Blue (red) contours indicate positive (negative) SSH anomalies.

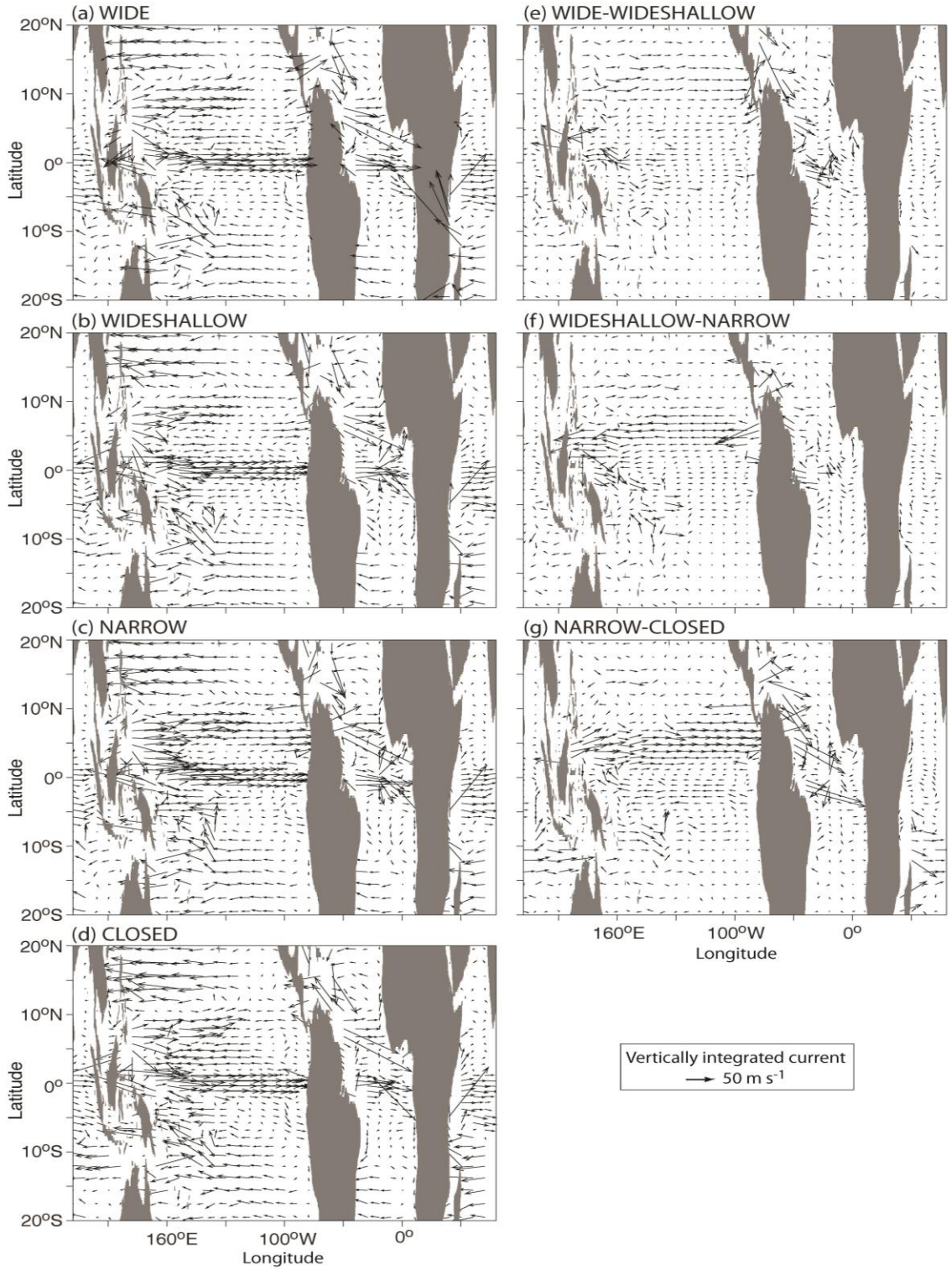

Fig. 3.3. GFDL-ESM2G 100-year annual average vertically integrated full-depth current (m s^{-1}; vectors) from 20ºN-20ºS for **(a)** WIDE, **(b)** WIDESHALLOW, **(c)** NARROW, **(d)**

CLOSED, and the time progression of the gradual shoaling and closure of the seaway: **(e)** WIDE-WIDESHALLOW, **(f)** WIDESHALLOW-NARROW, and **(g)** NARROW-CLOSED differences.

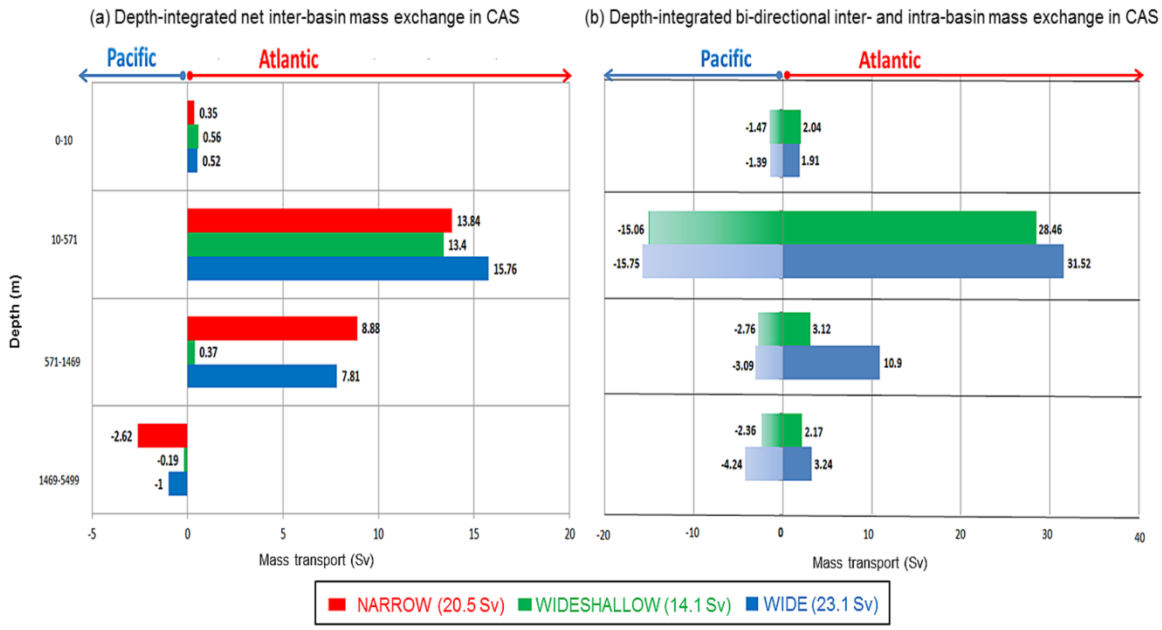

Fig. 3.4. GFDL-ESM2G 100-year annual average depth-integrated **(a)** net inter-basin and **(b)** bi-directional inter- and intra-basin mass transport (Sv; 10^6 m^3 s^{-1}) exchange in the CAS region as defined by the yellow transect (Fig. 2.1b; 77.5ºW; 8.2ºN) and boxes (Fig. 2.1c and Fig. 2.1d; 18º-8ºN; 100º-77ºW) for the NARROW and WIDE/WIDESHALLOW experiments, respectively. Positive (negative) mass transport values indicate transport from the Pacific to the Caribbean (Caribbean to Pacific). Full depth-integrated net inter-basin mass transport (Sv) values are included in parenthesis in the legend.

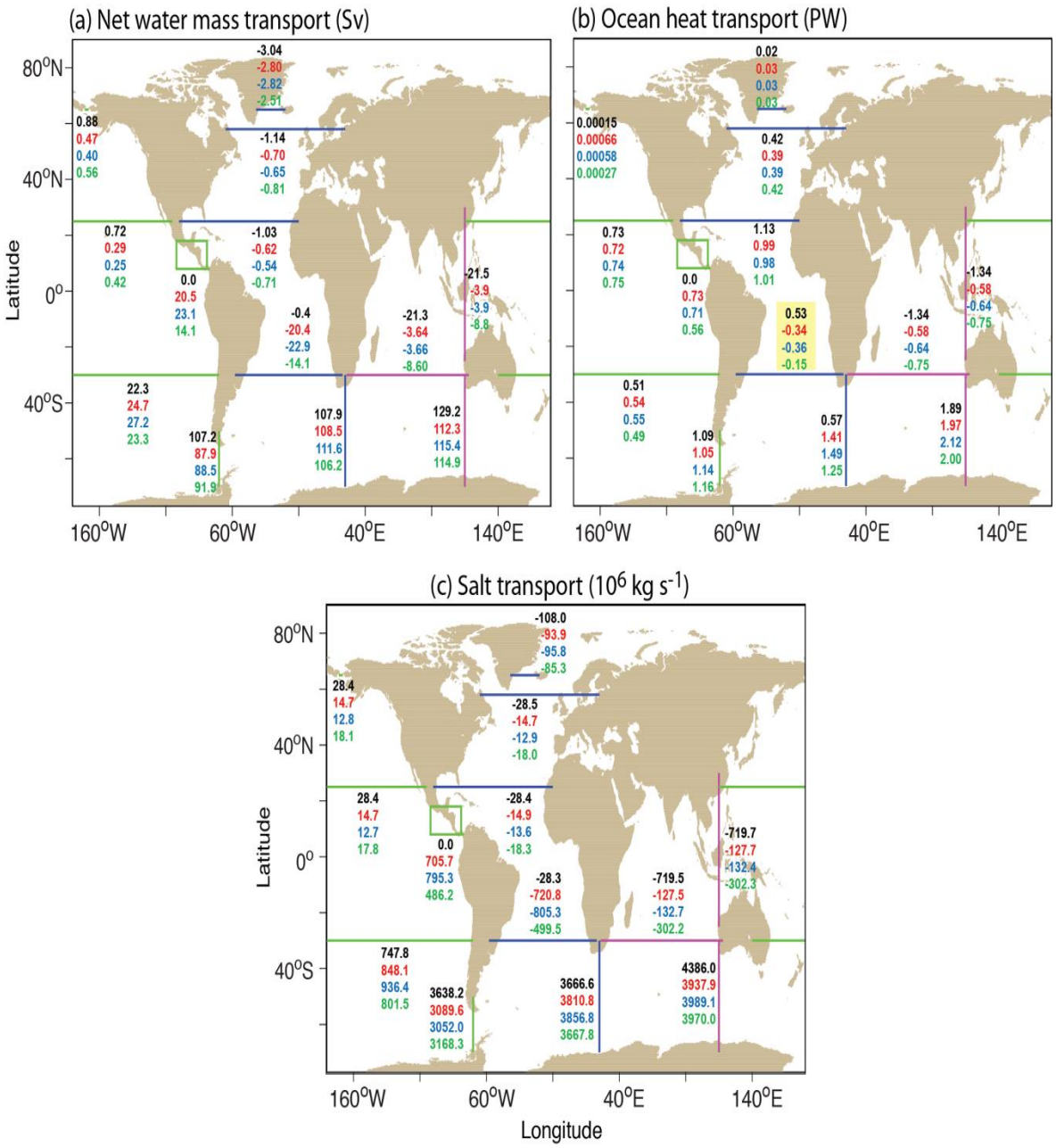

Fig. 3.5. GFDL-ESM2G 100-year annual average **(a)** net water mass (Sv; 10^6 m^3 s^{-1}), **(b)** ocean heat (PW), and **(c)** salt (10^6 kg s^{-1}) transports calculated for the CLOSED (black), NARROW (red), WIDE (blue), and WIDESHALLOW (green) seaway experiments for 13 transects in the Pacific (green), Atlantic (blue), and Indian (magenta) Oceans. Total transport is integrated from 0-5499 m with northward/eastward (southward/westward)

positive (negative). Bering Strait (green) at 65ºN; North Pacific Ocean (green) at 25ºN; South Pacific Ocean (green) at 30ºS; CAS NARROW (green) at 77.5ºW and 8.2ºN; CAS WIDE and WIDESHALLOW (green) at 18º-8ºN and 100º-77 ºW; Drake Passage (green) at 70ºW; Denmark Strait (blue) at 65ºN; GIN Seas/Denmark Strait/Labrador Sea (blue) at 58ºN; North Atlantic (blue) at 25ºN; South Atlantic (blue) at 30ºS; Africa to Antarctica (blue) at 25ºE; South Indian Ocean (magenta) at 30ºS; Indonesian Throughflow (magenta) at 115ºE; Australia to Antarctica (magenta) at 115ºE. The yellow shading **(b)** indicates the only transport direction reversal.

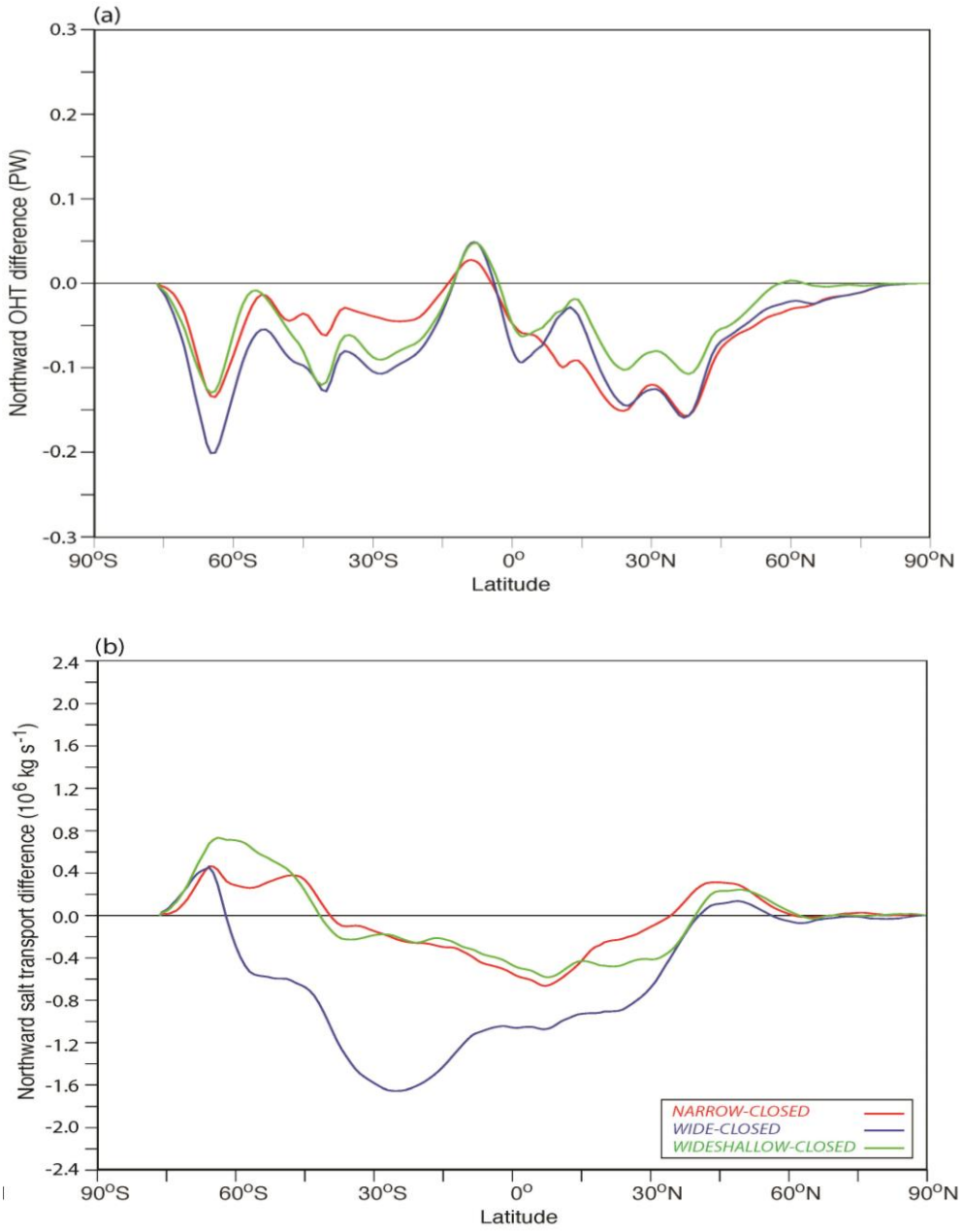

Fig. 3.6. GFDL-ESM2G 100-year annual average NARROW (red), WIDE (blue), and WIDESHALLOW (green) minus CLOSED northward **(a)** ocean heat transport (PW) and **(b)** salt transport (10^6 kg s^{-1}) difference.

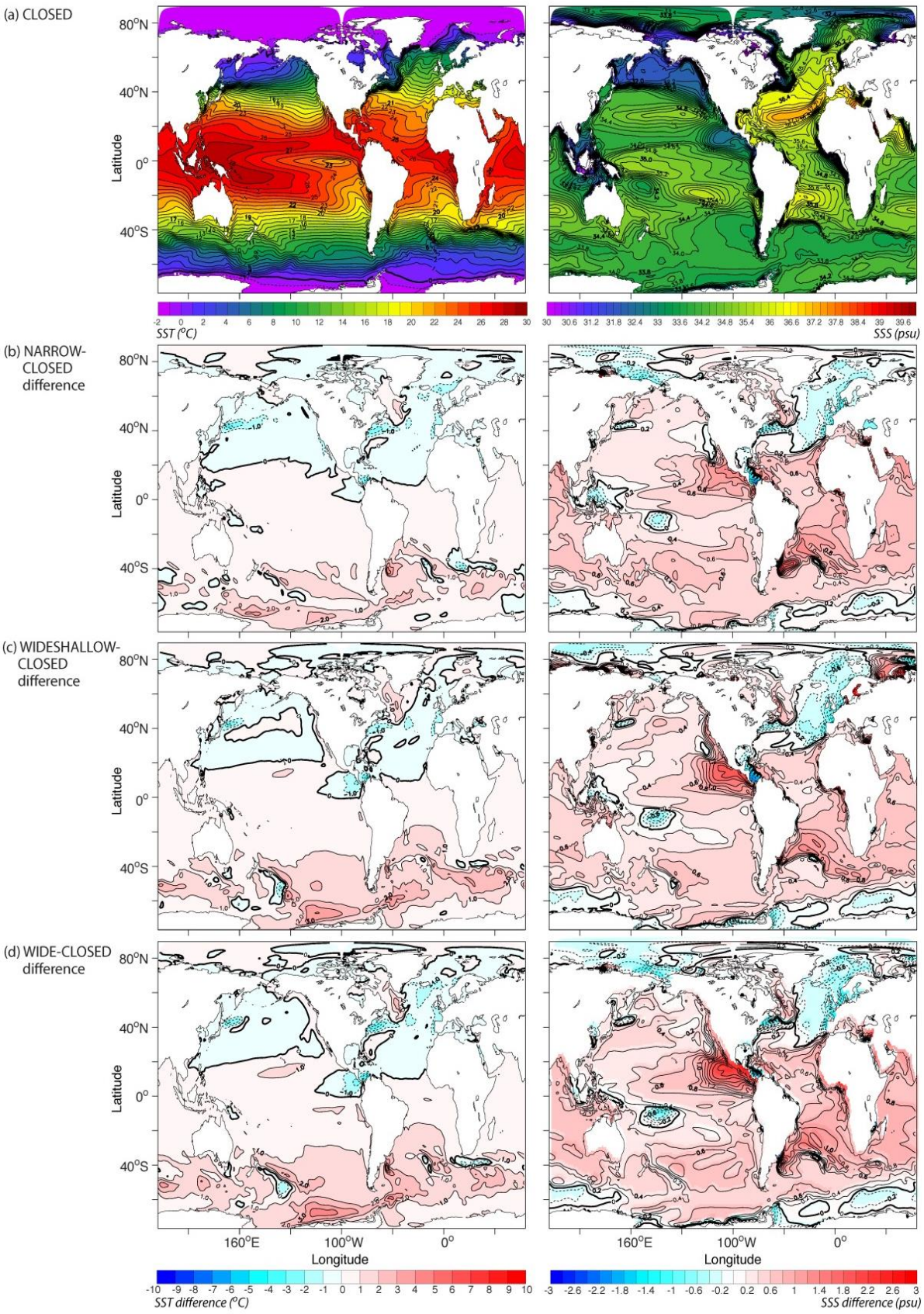
(a) CLOSED
(b) NARROW-CLOSED difference
(c) WIDESHALLOW-CLOSED difference
(d) WIDE-CLOSED difference
80°N
40°N
0°
40°S
Latitude
160°E
100°W
0°
Longitude
SST (°C)
SSS (psu)
SST difference (°C)
SSS difference (psu)

Fig. 3.7. GFDL-ESM2G 100-year annual average **(a)** CLOSED, **(b)** NARROW-CLOSED, **(c)** WIDESHALLOW-CLOSED, and **(d)** WIDE-CLOSED differences in sea surface temperature (SST; ºC; *left*) and sea surface salinity (SSS; psu; *right*) for the four seaway simulations.

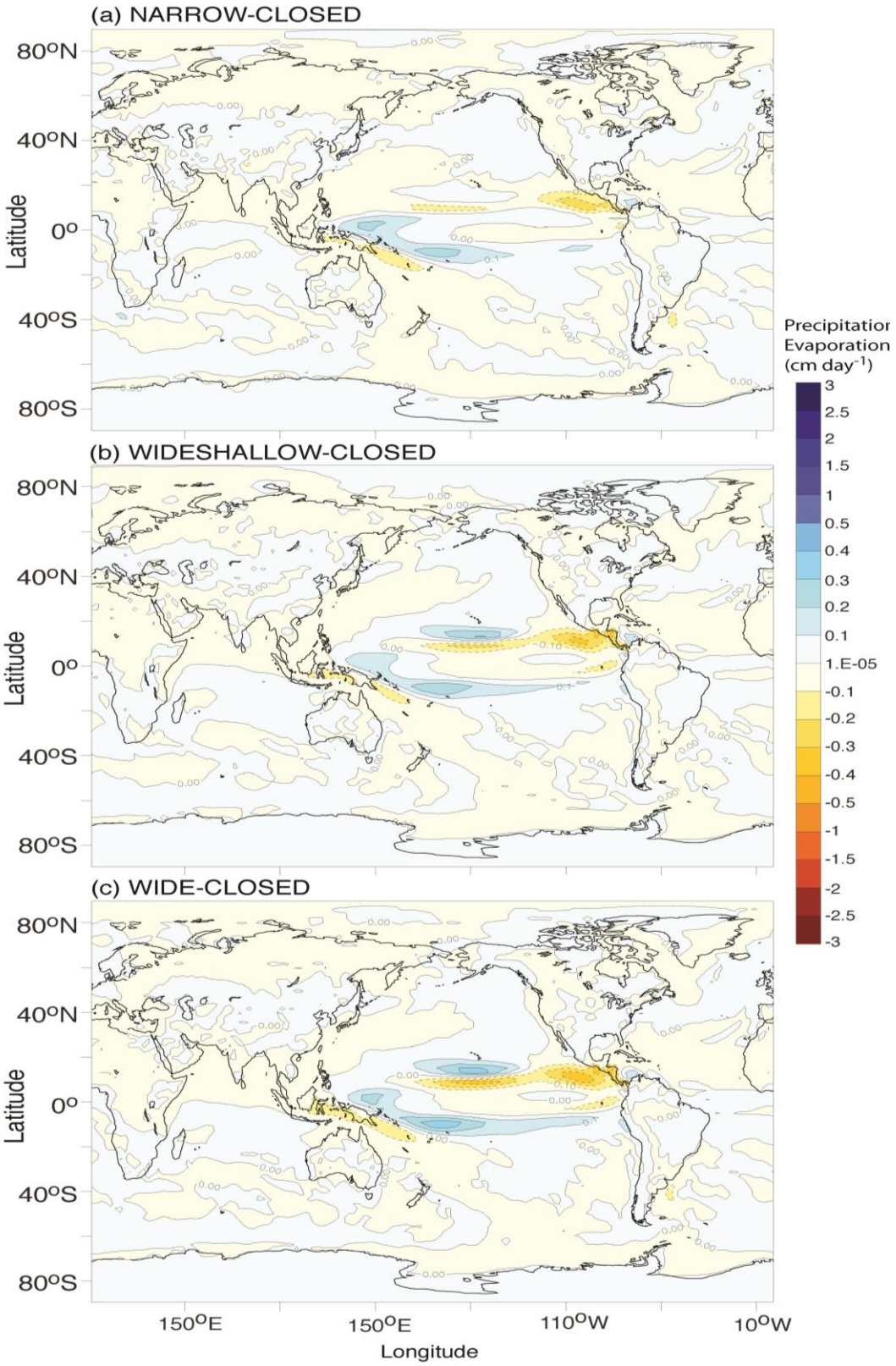
(a) NARROW-CLOSED
(b) WIDESHALLOW-CLOSED
(c) WIDE-CLOSED
80°N
40°N
0°
40°S
80°S
Latitude
150°E
150°E
110°W
10°W
Longitude
Precipitation
Evaporation
(cm day-1)
3
2.5
2
1.5
1
0.5
0.4
0.3
0.2
0.1
1.E-05
-0.1
-0.2
-0.3
-0.4
-0.5
-1
-1.5
-2
-2.5
-3

Fig. 3.8. GFDL-ESM2G 100-year annual average precipitation rate minus evaporation rate (cm day^{-1}) for **(a)** NARROW-CLOSED, **(b)** WIDESHALLOW-CLOSED, and **(c)** WIDE-CLOSED.

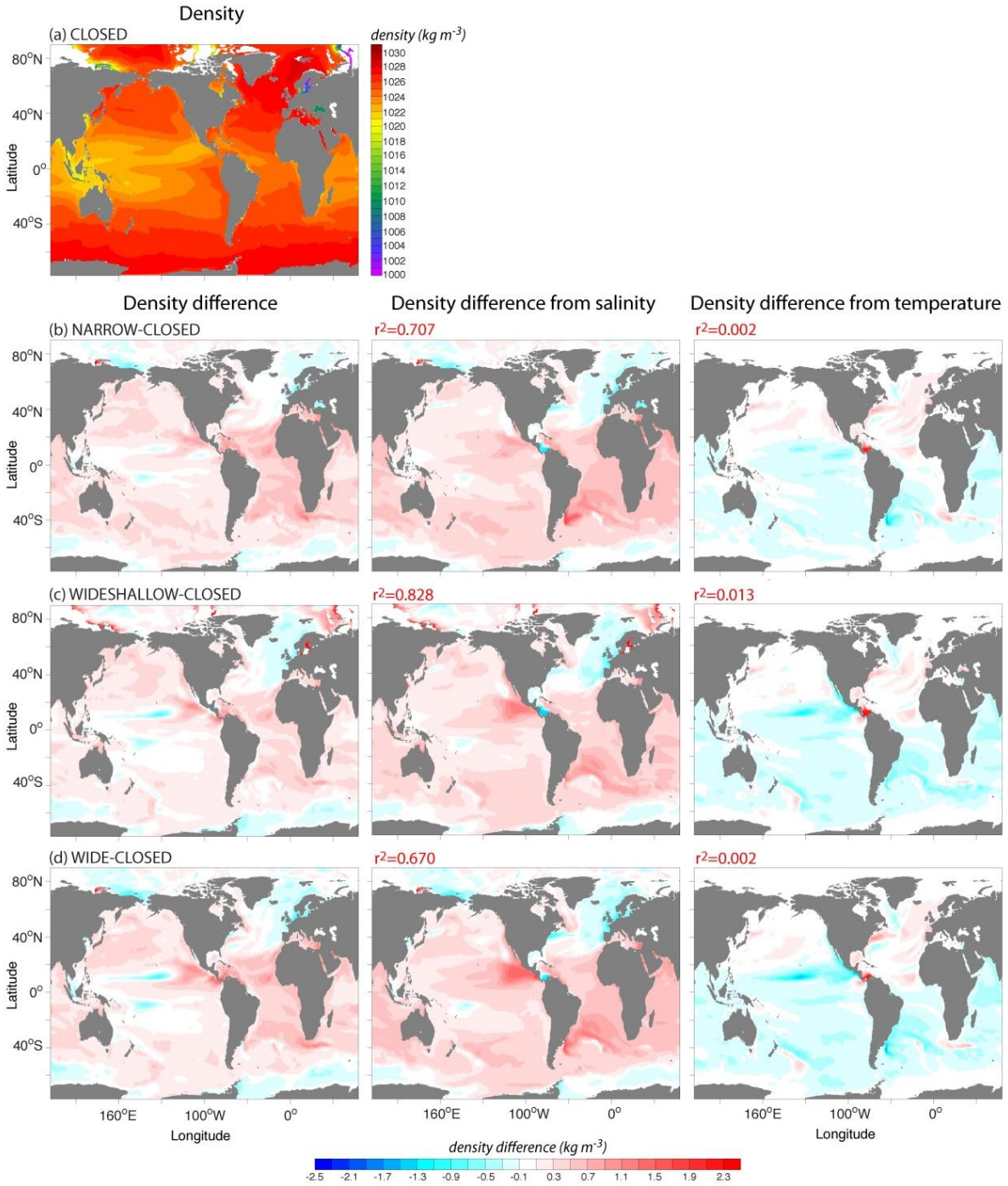

Fig. 3.9. GFDL-ESM2G 100-year annual average **(a)** CLOSED, **(b)** NARROW-CLOSED, **(c)** WIDESHALLOW-CLOSED, and **(d)** WIDE-CLOSED differences in the upper 100-m average ocean density (kg m^{-3}, *left*), and changes in the upper 100-m average ocean density from only changes in salinity with a seaway (kg m^{-3}, *middle*), and

from only changes in temperature with a seaway (kg m^{-3}, *right*) for the four seaway simulations. Coefficient of determination (r^2) values are indicated in red.

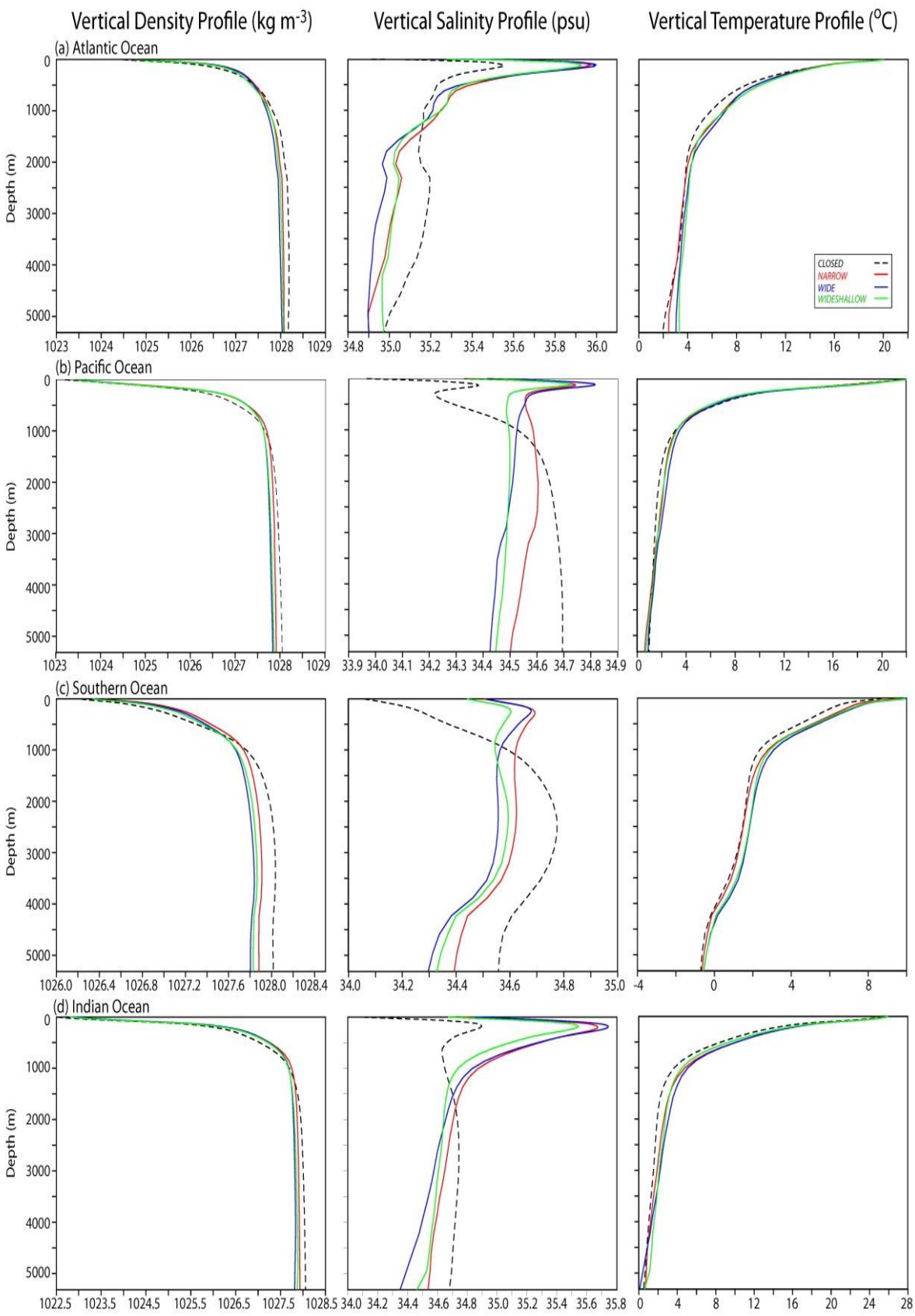
Vertical Density Profile (kg m-3)
Vertical Salinity Profile (psu)
Vertical Temperature Profile (°C)
(a) Atlantic Ocean
(b) Pacific Ocean
(c) Southern Ocean
(d) Indian Ocean
Depth (m)
CLOSED
NARROW
WIDE
WIDESHALLOW

Fig. 3.10. GFDL-ESM2G 100-year annual average vertical profiles of ocean density (kg m^{-3}; *left*), salinity (psu; *middle*), and temperature (°C; *right*) for the **(a)** Atlantic, **(b)** Pacific, **(c)** Southern, and **(d)** Indian Oceans for the CLOSED (black dashed), NARROW (red), WIDE (blue), and WIDESHALLOW (green) seaway experiments.

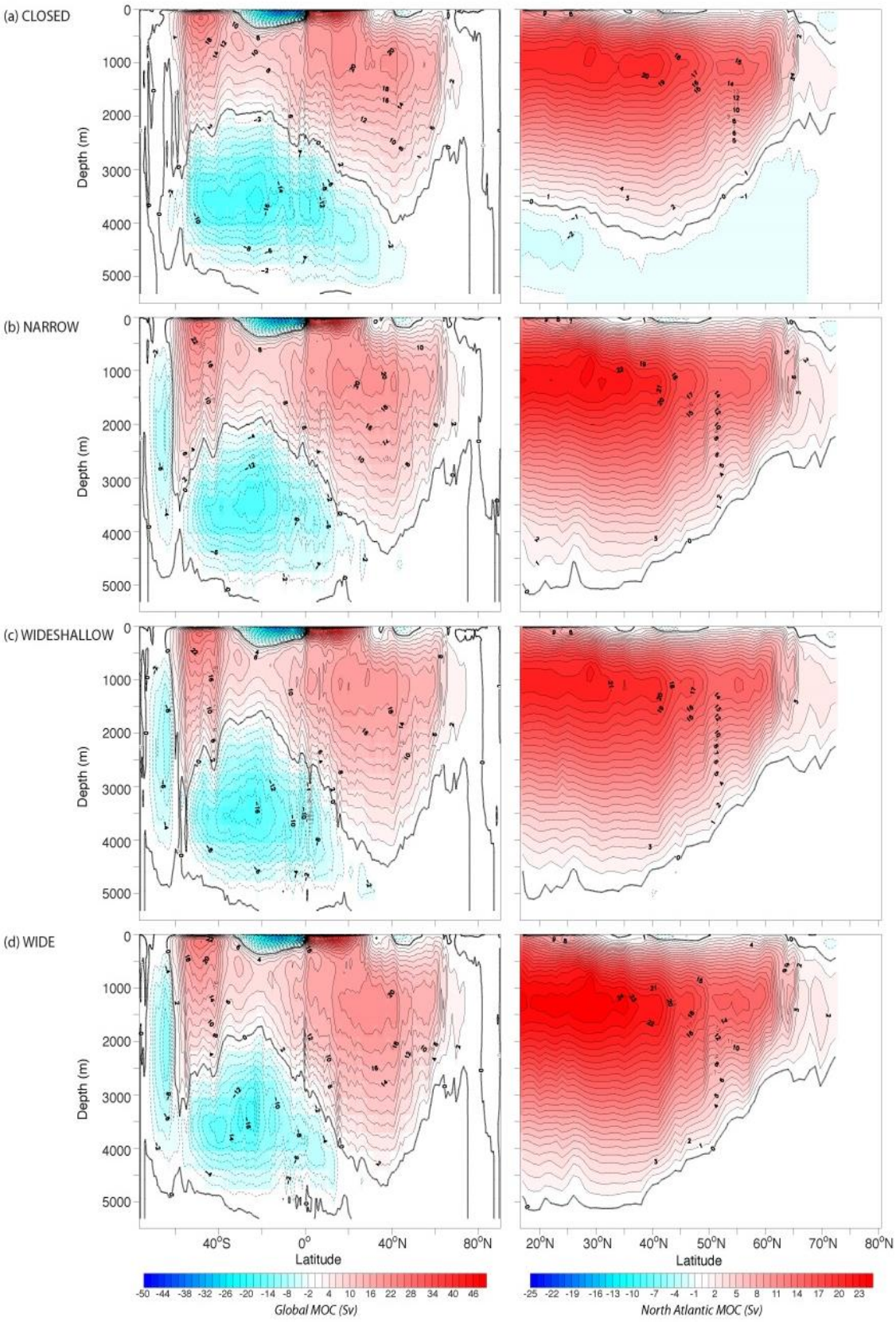
(a) CLOSED
(b) NARROW
(c) WIDESHALLOW
(d) WIDE
Depth (m)
0
1000
2000
3000
4000
5000
40°S
0°
40°N
80°N
Latitude
20°N
30°N
40°N
50°N
60°N
70°N
80°N
Latitude
-50 -44 -38 -32 -26 -20 -14 -8 -2 4 10 16 22 28 34 40 46
Global MOC (Sv)
-25 -22 -19 -16 -13 -10 -7 -4 -1 2 5 8 11 14 17 20 23
North Atlantic MOC (Sv)

Fig. 3.11. GFDL-ESM2G 100-year annual average global (*left*) and North Atlantic (*right*) meridional overturning streamfunction (1 Sv=10^6 m^3 s^{-1}) for the **(a)** CLOSED, **(b)** NARROW, **(c)** WIDESHALLOW, and **(d)** WIDE seaway experiments. Positive (negative) values in red (blue) indicate clockwise (counterclockwise) circulation.

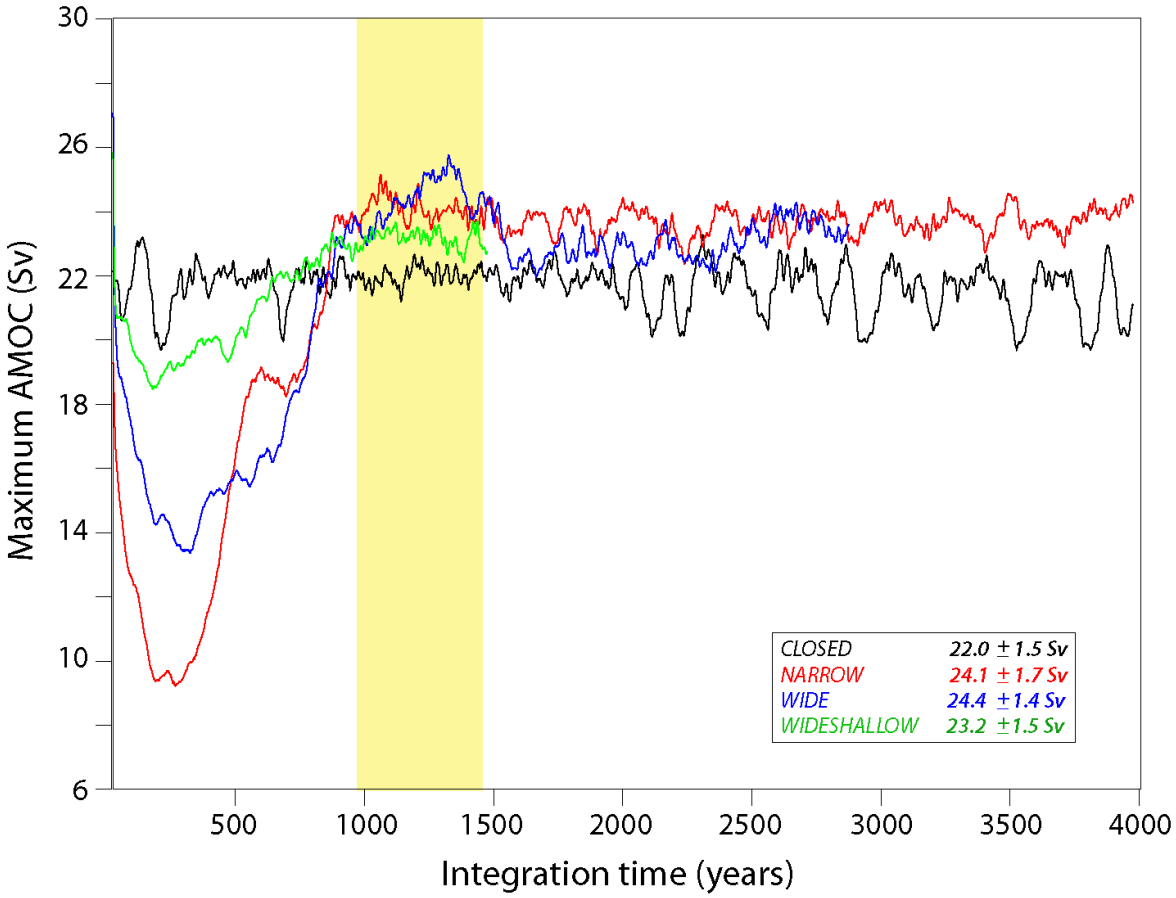

Fig. 3.12. Maximum Atlantic Meridional Overturning Circulation (AMOC; Sv) time series in density space from 20º-80ºN for the CLOSED (black), NARROW (red), WIDESHALLOW (green), and WIDE (blue) seaway experiments for model integration years 1-4000. The yellow shading indicates the 500-year period (1001-1500) used to compute the maximum AMOC values shown and 50-year boxcar smoothing is applied.

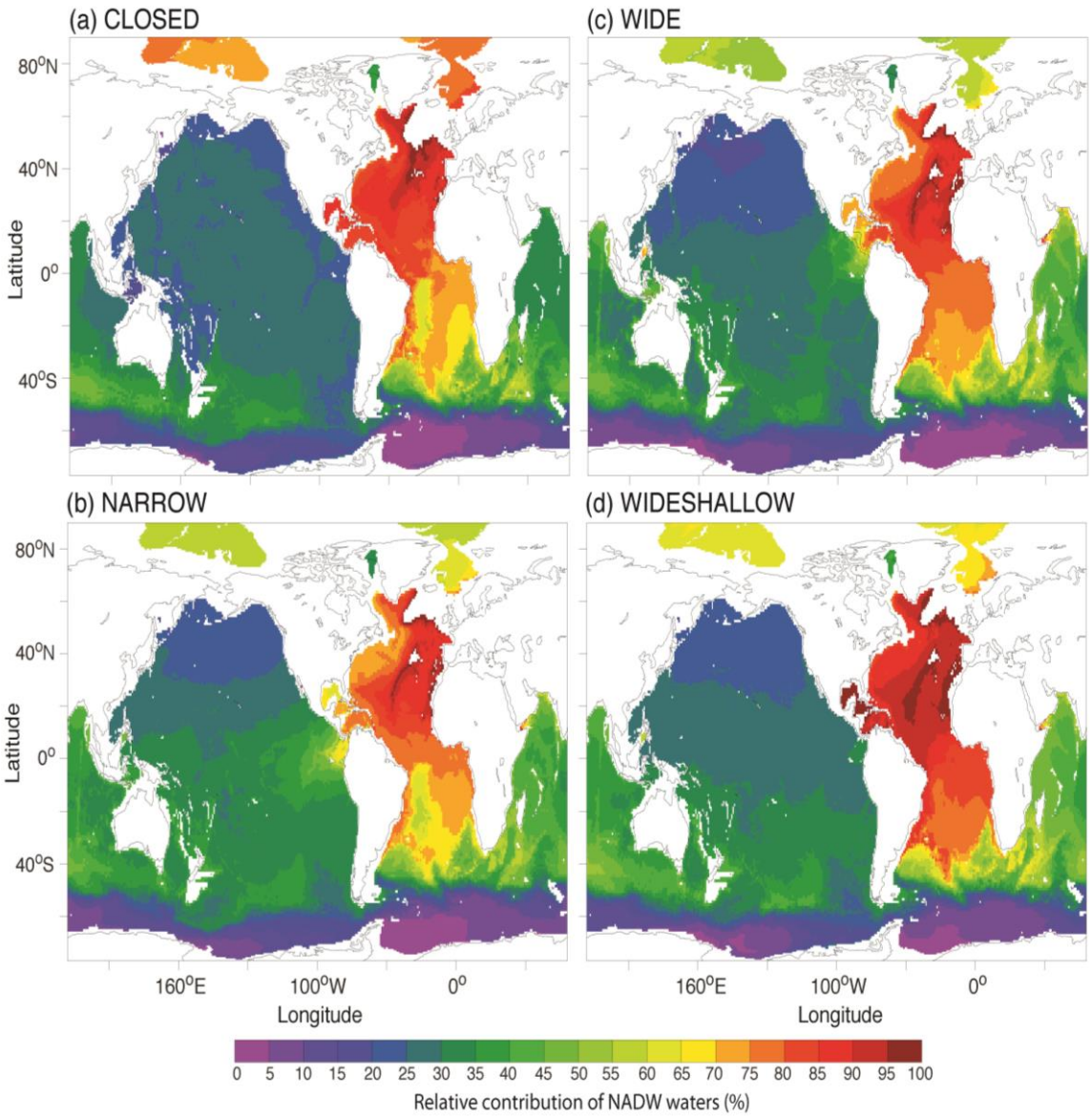

Fig. 3.13. GFDL-ESM2G 100-year annual average relative contribution of NADW (%) computed from (Eq. 1) and characterized by salinity for the **(a)** CLOSED, **(b)** NARROW, **(c)** WIDESHALLOW, and **(d)** WIDE seaway experiments. The calculation is based on Oppo and Fairbanks (1987) using end members chosen to represent the average salinity of the North Atlantic (20º-80 ºN; 30º-50ºW) and Drake Passage (50º-70 ºS; 70 ºW) from 1469-5499 m.

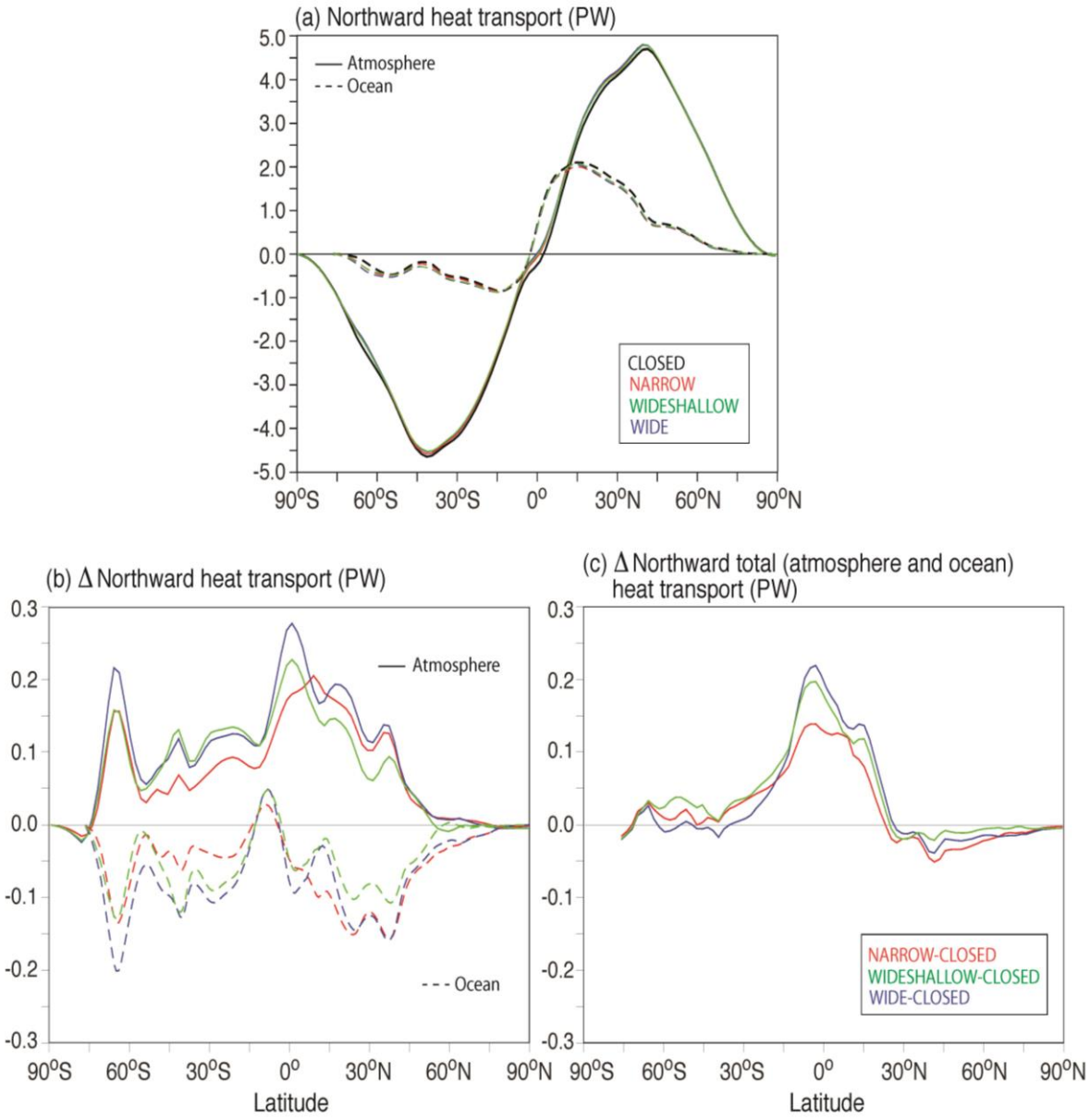

Fig. 4.1. GFDL-ESM2G 100-year annual global average **(a)** northward total (atmosphere plus ocean) heat transport (PW), **(b)** northward total heat transport difference with the CAS (PW), and **(c)** northward total heat transport difference with CAS (PW) by component with atmosphere (solid) and ocean (dashed) for the CLOSED (black), NARROW (red), WIDESHALLOW (green), and WIDE (blue) seaways.

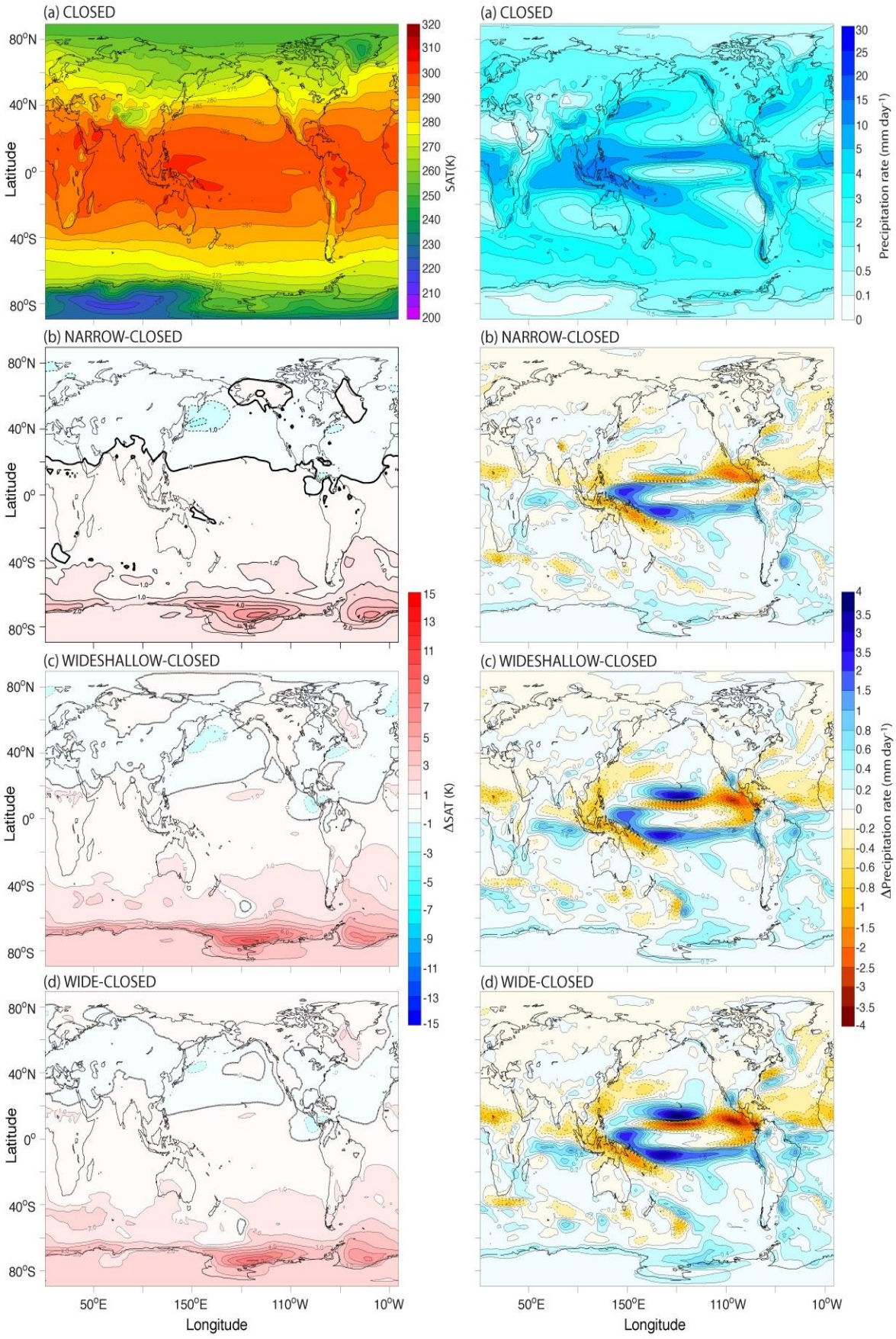
(a) CLOSED
(b) NARROW-CLOSED
(c) WIDESHALLOW-CLOSED
(d) WIDE-CLOSED
Latitude
Longitude
80°N
40°N
0°
40°S
80°S
50°E
150°E
110°W
10°W
SAT(K)
320
310
300
290
280
270
260
250
240
230
220
210
200
ΔSAT (K)
15
13
11
9
7
5
3
1
-1
-3
-5
-7
-9
-11
-13
-15
Precipitation rate (mm day⁻¹)
30
25
20
15
10
5
4
3
2
1
0.5
0.1
0
ΔPrecipitation rate (mm day⁻¹)
4
3.5
3
3.5
2
1.5
1
0.8
0.6
0.4
0.2
0
-0.2
-0.4
-0.6
-0.8
-1
-1.5
-2
-2.5
-3
-3.5
-4

Fig. 4.2. GFDL-ESM2G 100-year annual average 2-m surface air temperature (SAT; K; *left*) and precipitation rate (mm day^{-1}; *right*) for **(a)** CLOSED and the differences between the **(b)** NARROW, **(c)** WIDESHALLOW, and **(d)** WIDE and CLOSED seaway experiments.

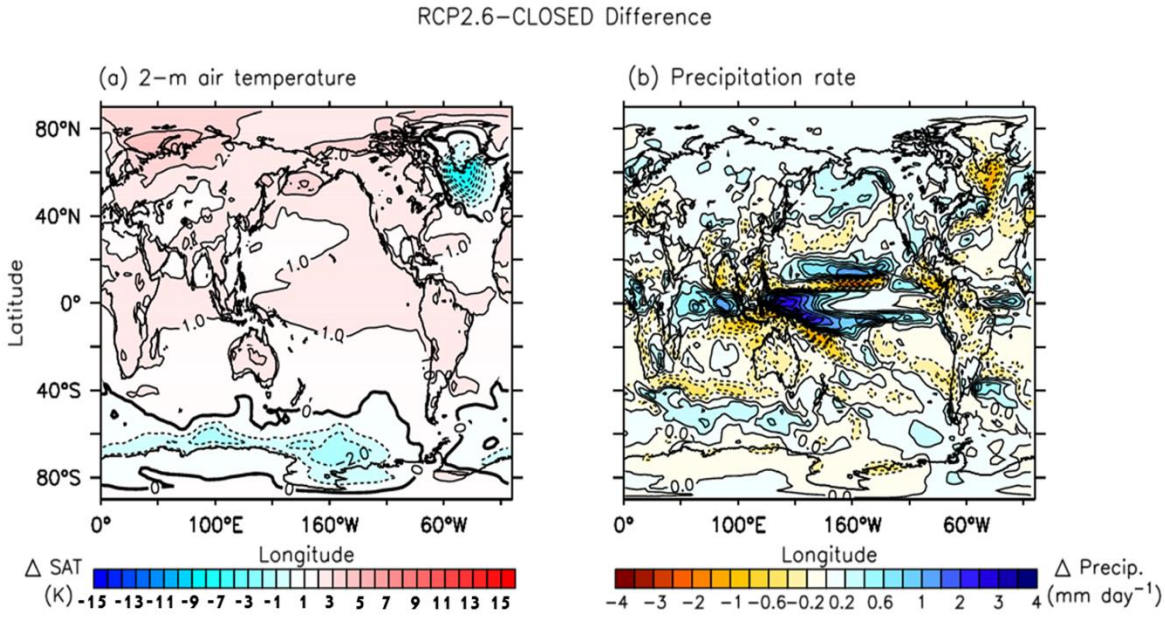

Fig. 4.3. GFDL-ESM2G 100-year annual average difference in **(a)** 2-m surface air temperature (SAT; K; *left*) and **(b)** precipitation rate (mm day^{-1}; *right*) between the CMIP5 RCP2.6 experiment and CLOSED seaway experiment (i.e., CMIP5 1860 preindustrial control).

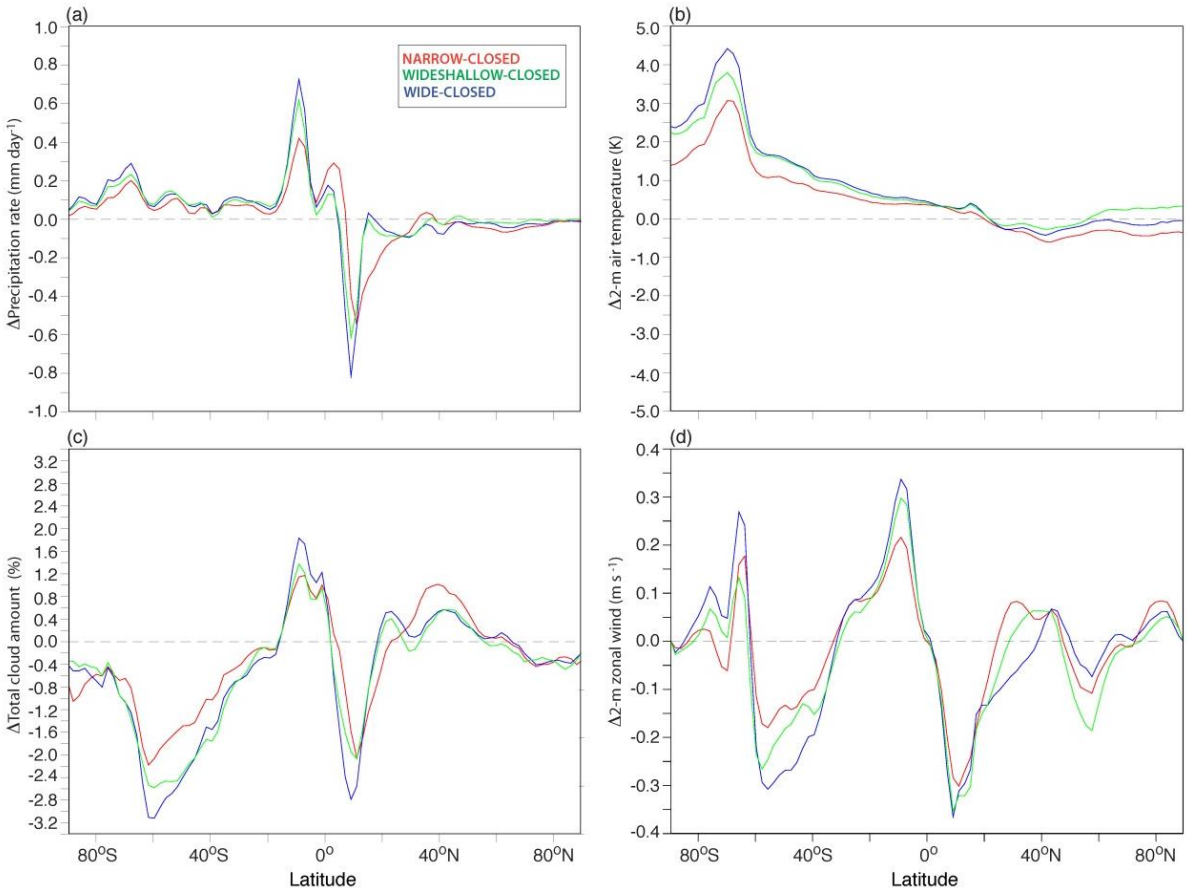

Fig. 4.4. GFDL-ESM2G 100-year zonal average **(a)** precipitation rate (mm day^{-1}), **(b)** 2-m surface air temperature (SAT; K), **(c)** total cloud amount (%), and **(d)** 2-m zonal wind (m s^{-1}) NARROW-CLOSED (red), WIDESHALLOW-CLOSED (green), and WIDE-CLOSED (blue) differences, and CLOSED (d; black) seaway simulations.

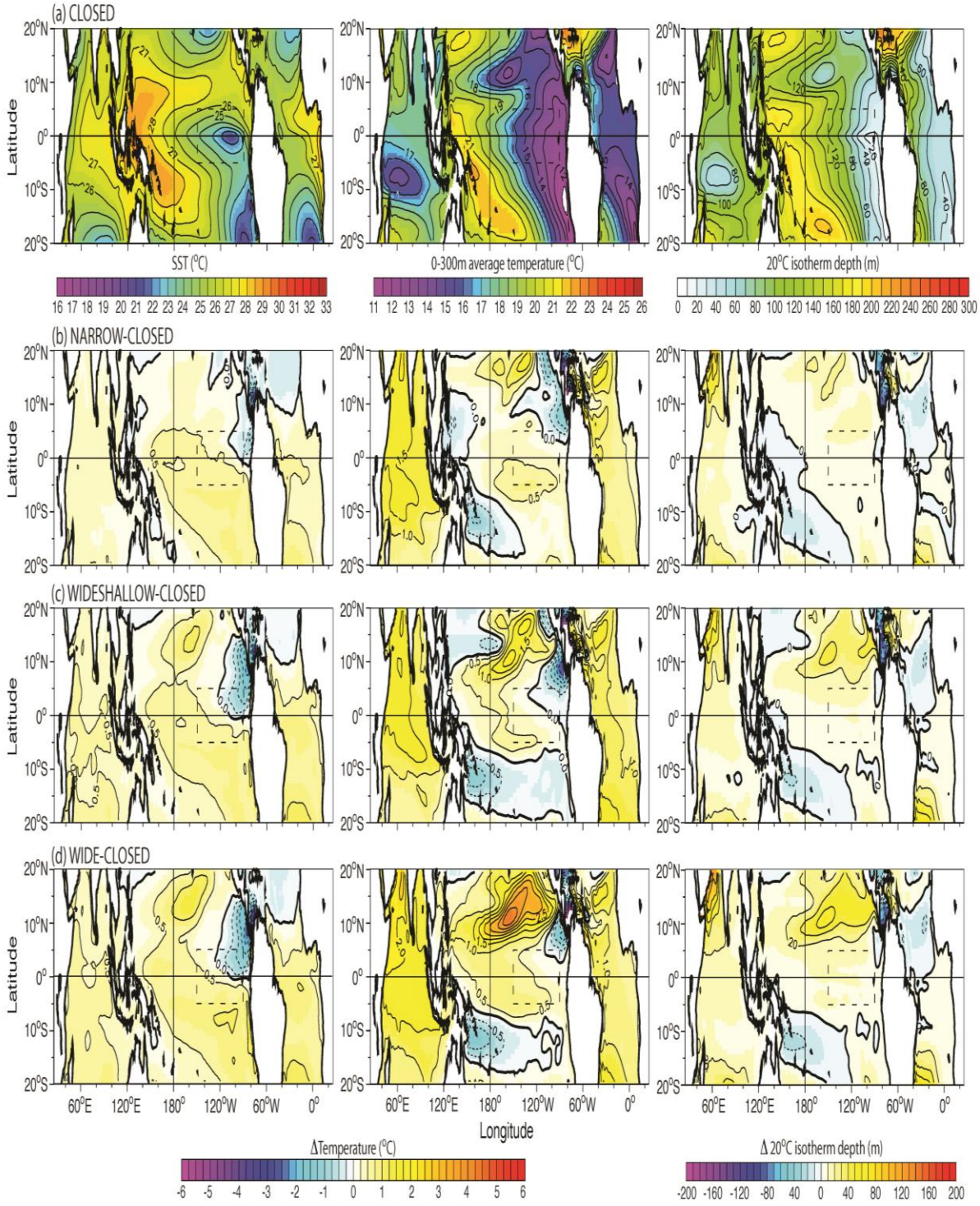

Fig. 4.5. GFDL-ESM2G 100-year annual average tropical (20ºN-20ºS) SST (ºC; *left*), 0-

300m average ocean temperature (ºC; *middle*), and 20ºC isotherm depth (m; *right*) for **(a)** CLOSED, and the difference between **(b)** NARROW, **(c)** WIDESHALLOW, and **(d)** WIDE and CLOSED. The dotted region indicates the Niño-3 region (5°N-5°S, 150°-90°W).

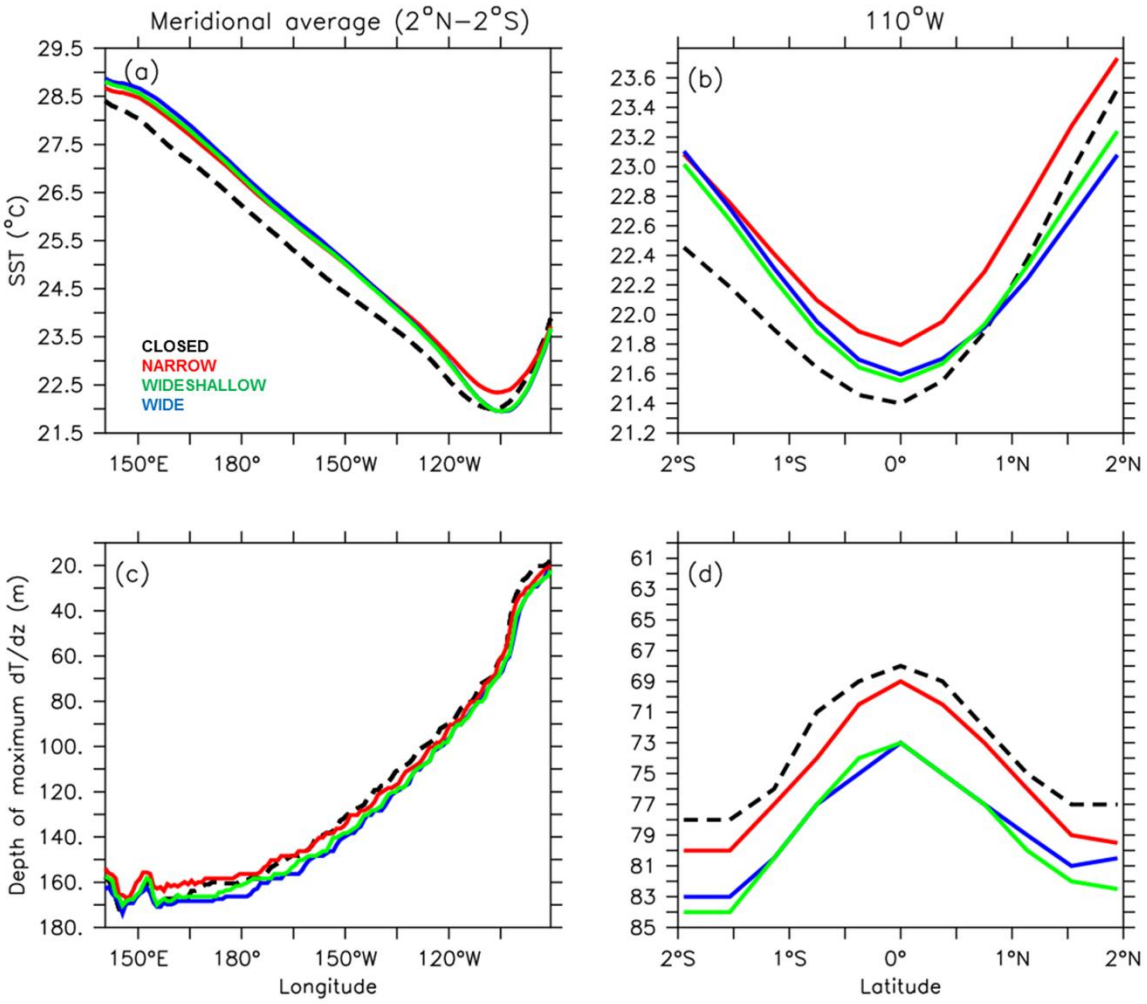

Fig. 4.6. GFDL-ESM2G 100-year annual equatorial Pacific (2°N-2°S, 140°E-90°W) meridional average **(a)** SST (°C) and **(b)** depth of maximum *dT/dz* (m; representing the thermocline depth), and slice at 110°W **(c)** SST (°C) and **(d)** depth of maximum *dT/dz* (m) for the CLOSED (black dash), NARROW (red), WIDESHALLOW (green), and WIDE (blue) seaway simulations.

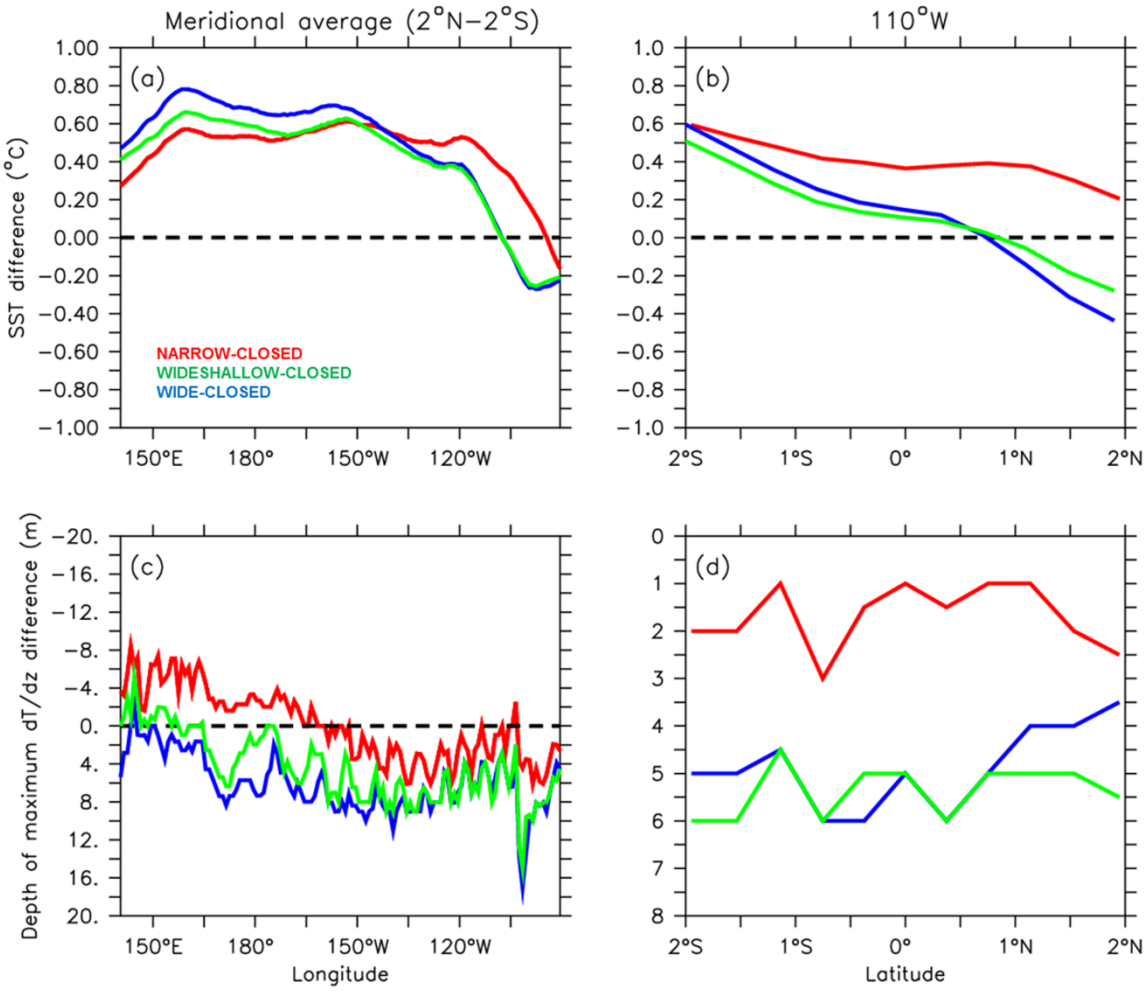

Fig. 4.7. GFDL-ESM2G 100-year annual equatorial Pacific (2°N-2°S, 140°E-90°W) meridional average difference in **(a)** SST (°C) and **(b)** depth of maximum *dT/dz* (m; representing the thermocline depth), and slice at 110°W difference in **(c)** SST (°C) and **(d)** depth of maximum *dT/dz* (m) between the NARROW (red), WIDESHALLOW (green), and WIDE (blue) and the CLOSED seaway simulations. Zero line is included for reference (black dash).

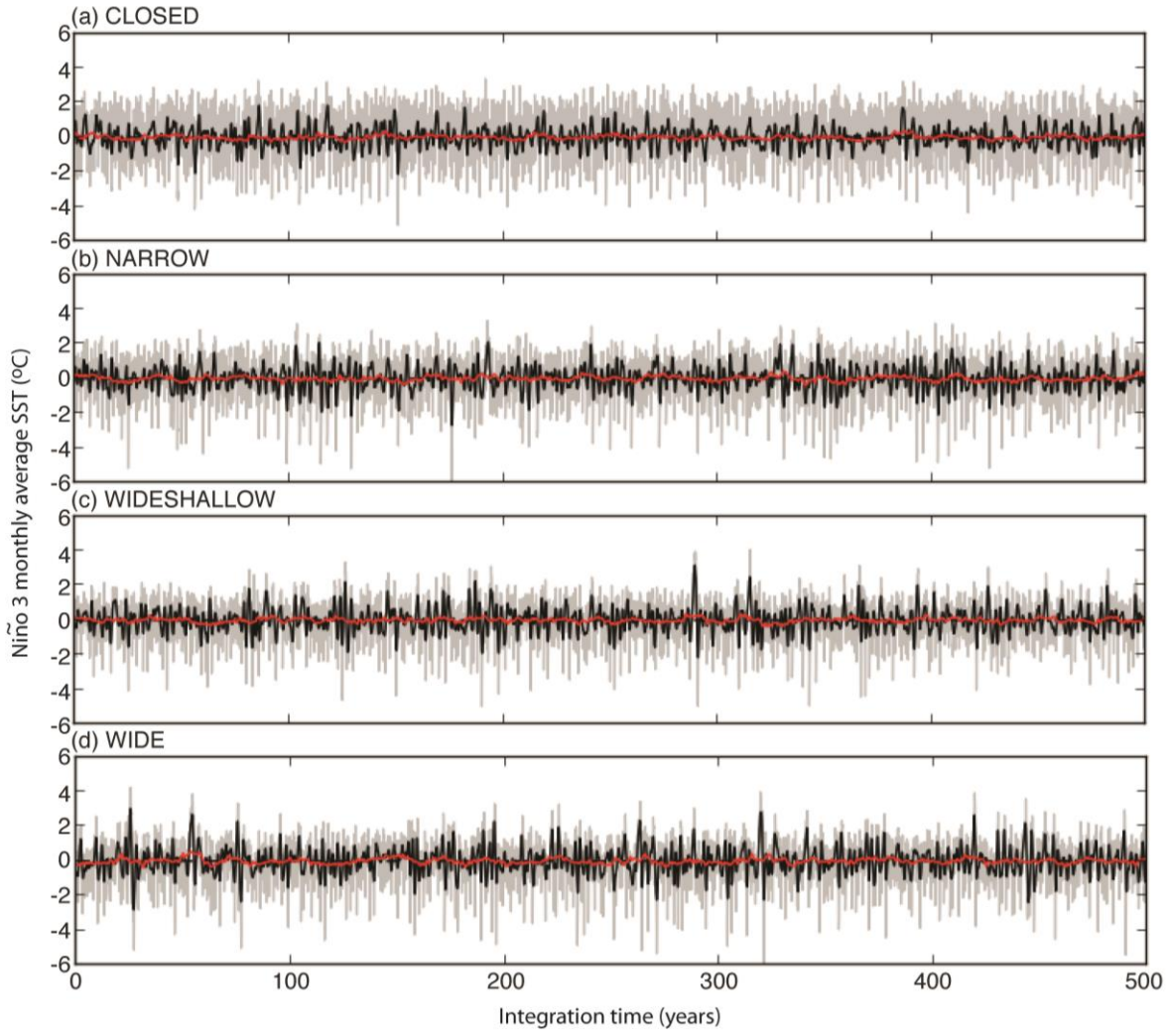

Fig. 4.8. GFDL-ESM2G Niño-3 (5°N-5°S, 150°-90°W) time series for 500-year (model years 1001-1500) monthly average sea surface temperatures (SST; °C) for the **(a)** CLOSED, **(b)** NARROW, **(c)** WIDESHALLOW, and **(d)** WIDE seaway simulations. Grey, black, and red lines indicate monthly, annual, and decadal time-averages.

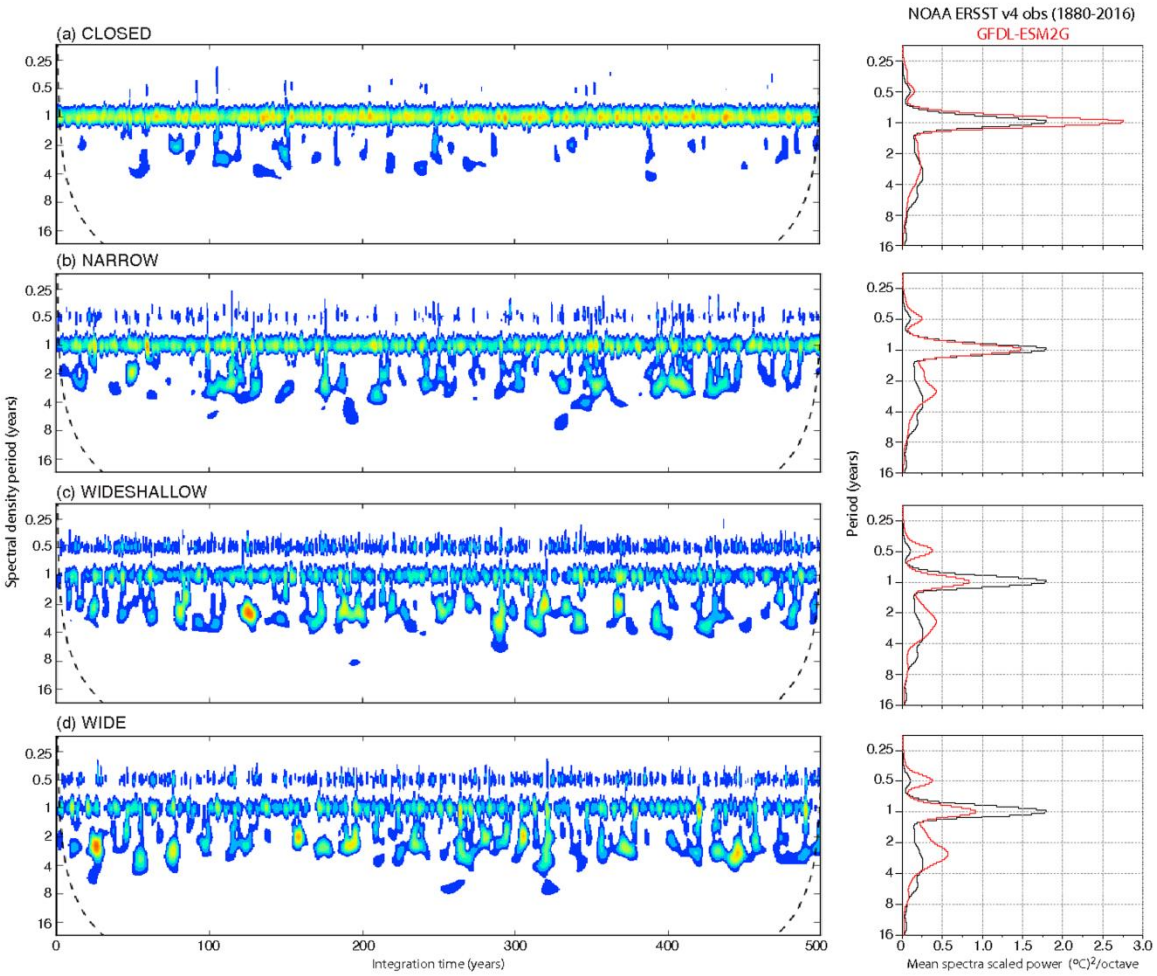

Fig. 4.9. GFDL-ESM2G Niño-3 (5°N-5°S, 150°-90°W; dotted box in Fig. 4.5) 500-year monthly average SST spectral density period (years; *left*) and SST power spectra ($°C^2$ $octave^{-1}$) vs period (years; *right*) for the **(a)** CLOSED, **(b)** NARROW, **(c)** WIDESHALLOW, and **(d)** WIDE seaway simulations and from NOAA's Extended Reconstruction version 4 for 1880-2016 observations (ERSST.v4; Huang et al. 2015; black, *right*). Details of the wavelet analysis method are described in Wittenberg et al. (2006, caption in their Fig. 20).

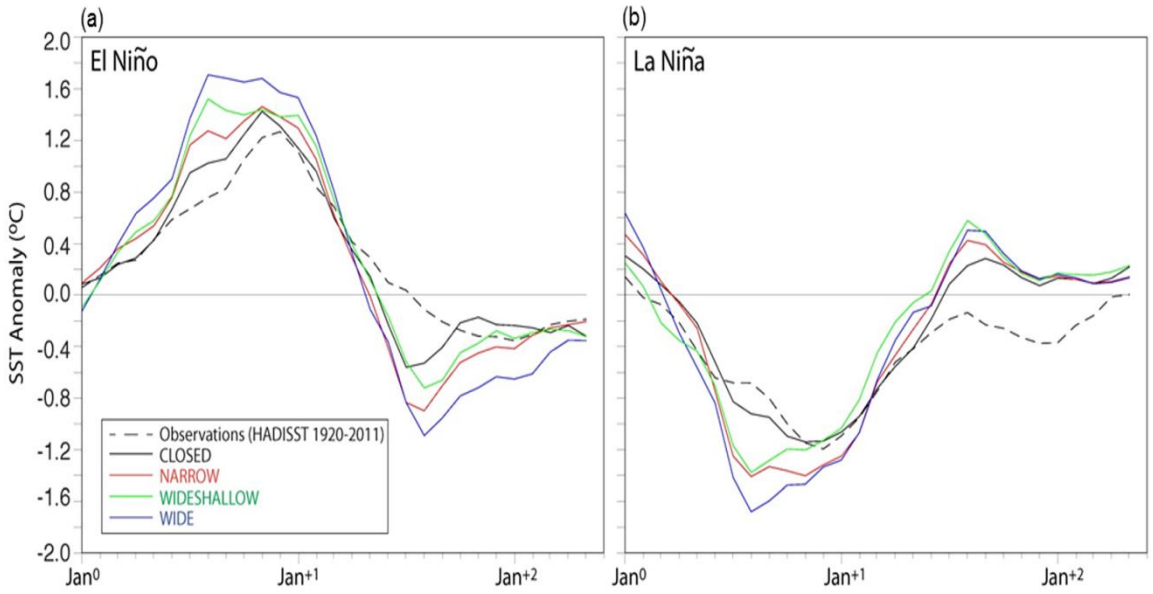

Fig. 4.10. GFDL-ESM2G 500-year average **(a)** El Niño (*left*) and **(b)** La Niña (*right*) Hovmöller SST anomaly (°C) average (3°N-3°S, 85°E-150°W) composites for the Hadley Centre Sea Ice and Sea Surface Temperature (HadISST) data set (Rayner et al. 2003) (black dash), CLOSED (black solid), NARROW (red), WIDESHALLOW (green), and WIDE (blue) seaway simulations.

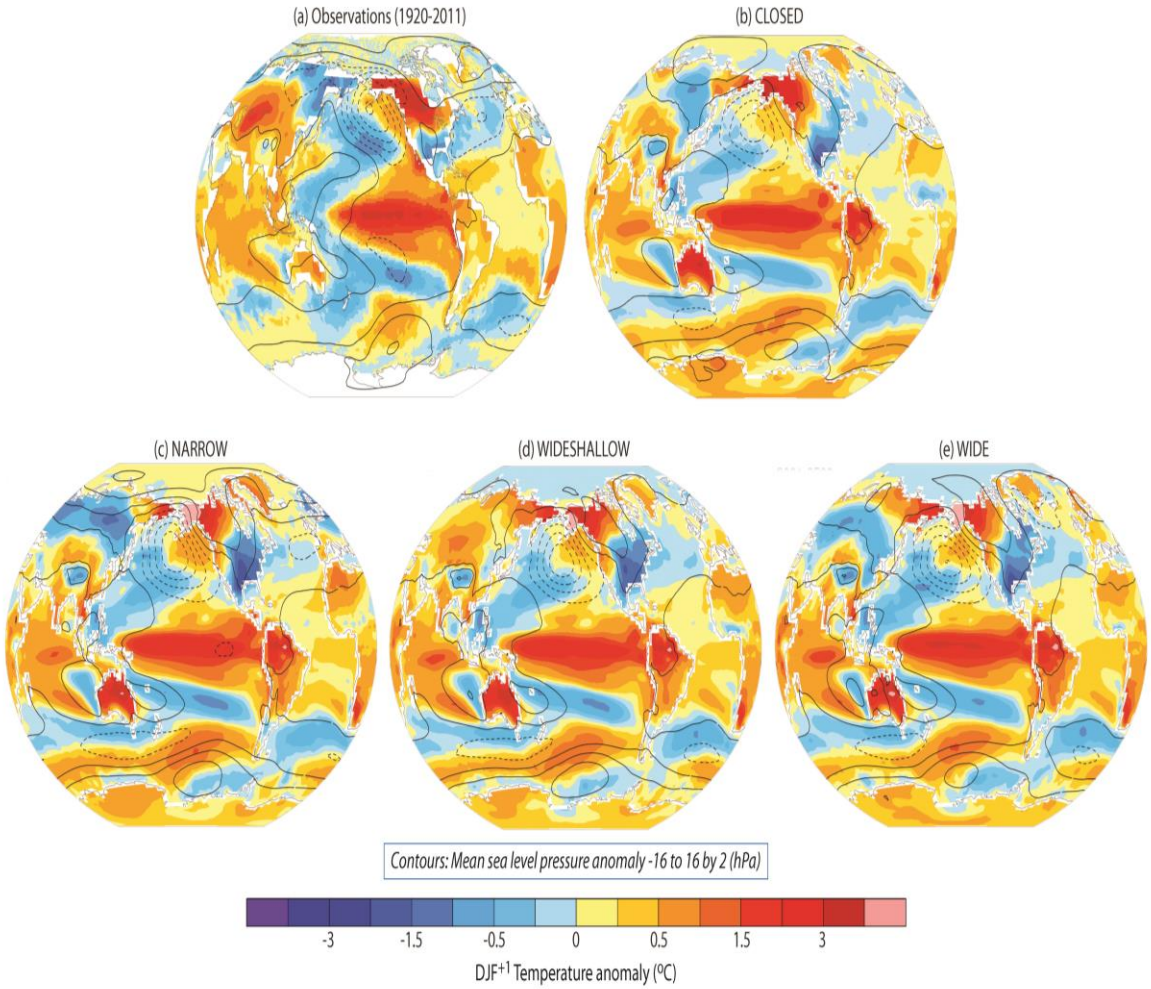

Fig. 4.11. Niño-3.4 (5°N-5°S, 170-120°W) spatial composite maps of 2-m air and sea surface temperature (°C; shaded) and mean sea level pressure (hPa; contours) anomalies for DJF^{+1} (boreal winter year 1) for the **(a)** Hadley Centre Sea Ice and Sea Surface Temperature (HadISST) data set (Rayner et al. 2003), NOAA Merged Land-Ocean Surface Temperature Analysis V3.5.3 (MLOST; Vose et al. 2012), and NOAA CIRES Twentieth Century Global Reanalysis version 2 (20thC_ReanV2; Compo et al. 2009) 1920-2011 observations, and GFDL-ESM2G 500-year **(b)** CLOSED, **(c)** NARROW, **(d)** WIDESHALLOW, and **(e)** WIDE seaway simulations.

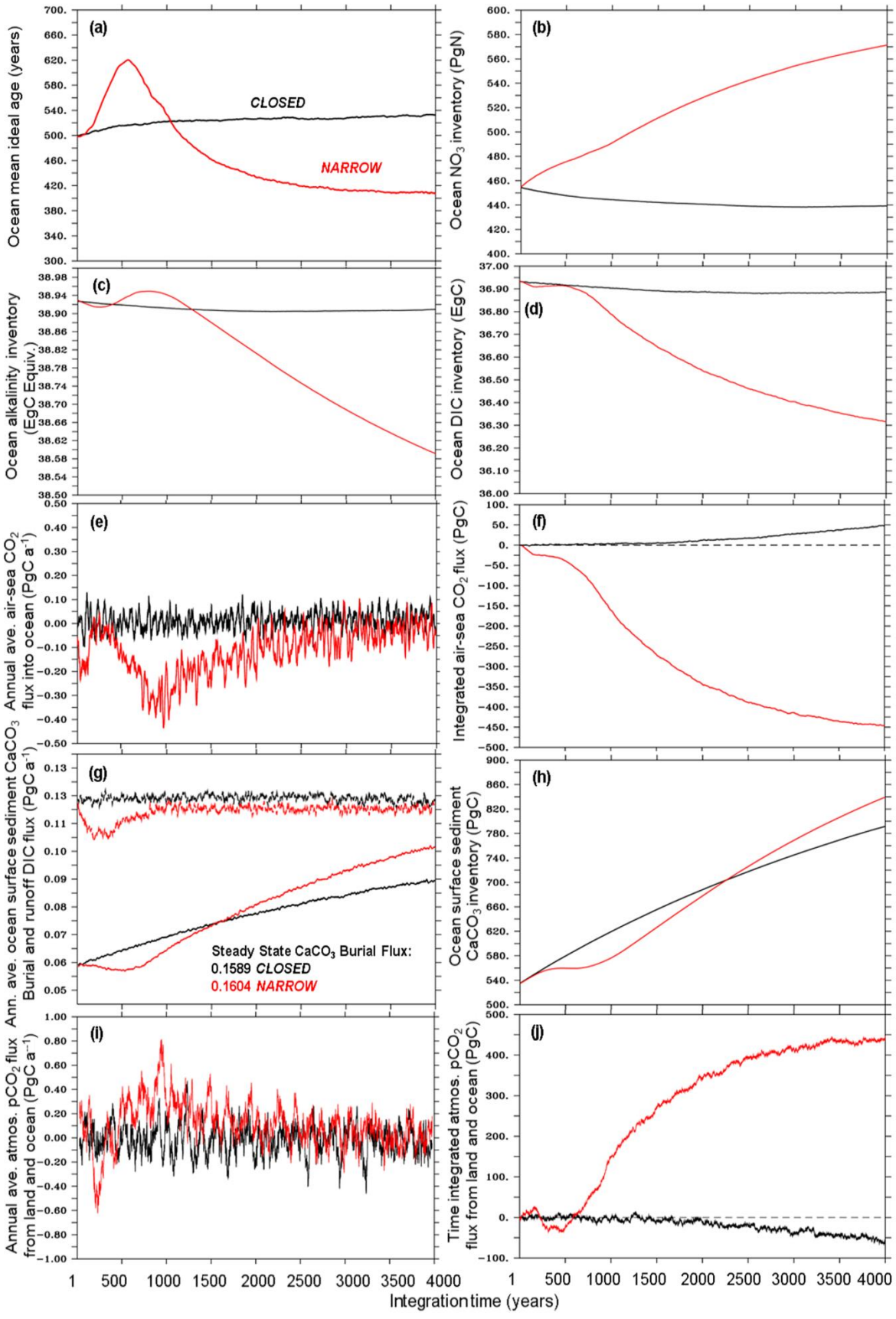
(a)
Ocean mean ideal age (years)
CLOSED
NARROW
(b)
Ocean NO3 inventory (PgN)
(c)
Ocean alkalinity inventory (EgC Equiv.)
(d)
Ocean DIC inventory (EgC)
(e)
Annual ave. air-sea CO2 flux into ocean (PgC a-1)
(f)
Integrated air-sea CO2 flux (PgC)
(g)
Ann. ave. ocean surface sediment CaCO3 Burial and runoff DIC flux (PgC a-1)
Steady State CaCO3 Burial Flux:
0.1589 CLOSED
0.1604 NARROW
(h)
Ocean surface sediment CaCO3 inventory (PgC)
(i)
Annual ave. atmos. pCO2 flux from land and ocean (PgC a-1)
(j)
Time integrated atmos. pCO2 flux from land and ocean (PgC)
Integration time (years)

Fig. 5.1. Global annual **(a)** ocean mean ideal age (years), **(b)** ocean NO_3^- inventory (PgN), **(c)** ocean alkalinity inventory (exagrams C equivalent), **(d)** ocean dissolved inorganic carbon inventory (DIC; exagrams C; EgC), **(e)** annual air-sea CO_2 flux (PgC a^{-1}; positive flux into the ocean), **(f)** integrated air-sea CO_2 flux (PgC; positive flux into the ocean), **(g)** annual ocean surface sediment $CaCO_3$ burial flux (PgC a^{-1}; solid lines; positive flux downward), river runoff flux of DIC (PgC a^{-1}; dashed lines); values represent long-term (~100 kyr) results using the offline calcite box model, **(h)** ocean surface sediment $CaCO_3$ inventory (PgC), **(i)** annual atmosphere pCO_2 flux from land and ocean ($PgCO_2$ a^{-1}; positive flux into atmosphere), and **(j)** annual integrated atmosphere pCO_2 flux from land and ocean (PgC; positive flux into atmosphere) for the CLOSED (black) and NARROW (red) GFDL-ESM2G seaway simulations. 20-year **(e)** and **(g),** and 50-year **(i)** boxcar smoothing is applied. Dashed lines represent the air-sea interface (zero line) in **(f)** and **(j)**.

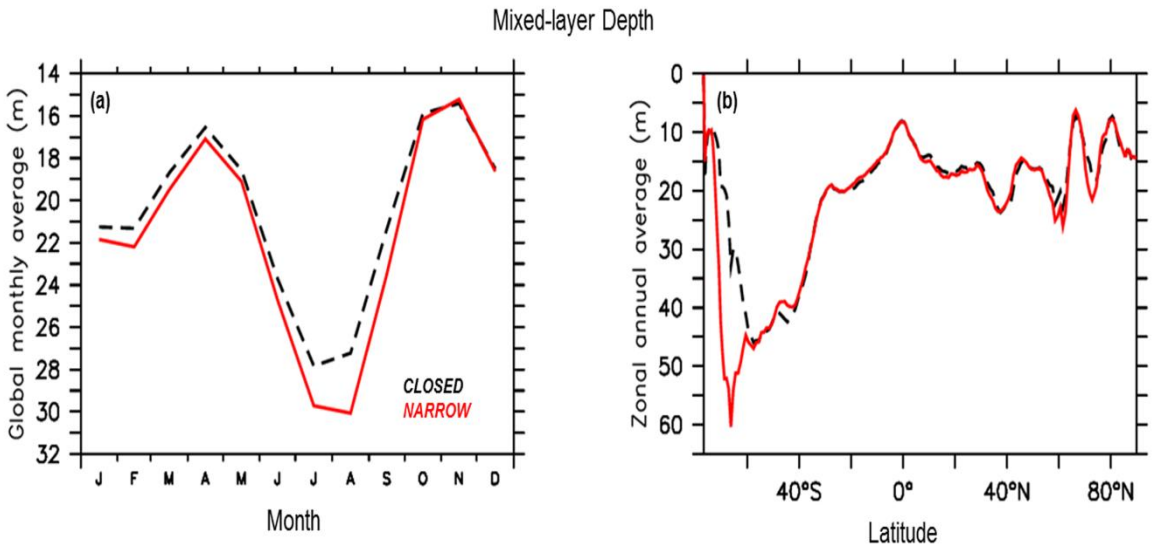

Fig. 5.2. 100-year **(a)** global monthly and **(b)** zonal annual average mixed layer depth (m) for the CLOSED (black dash) and NARROW (red) GFDL-ESM2G seaway simulations.

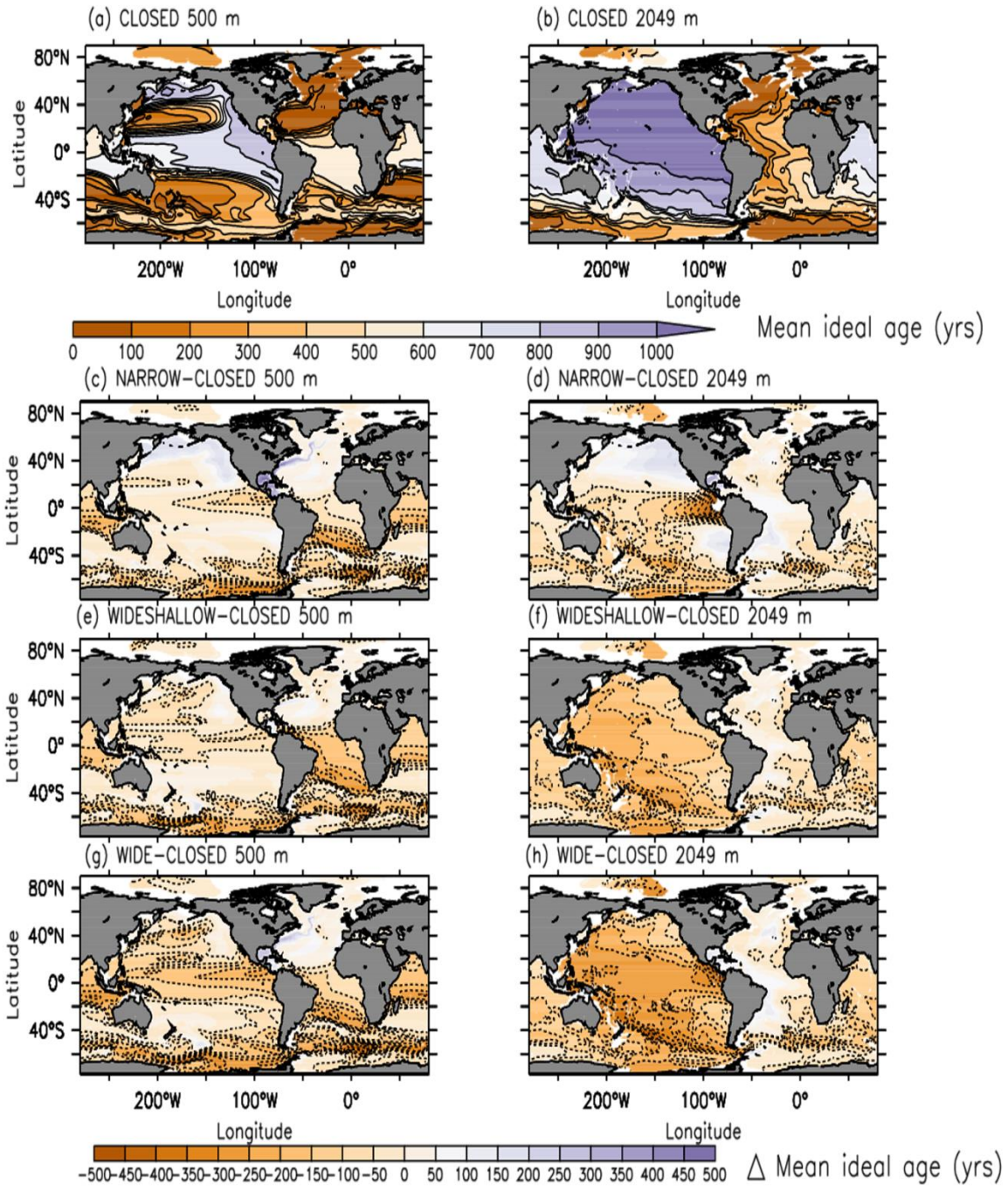

Fig. 5.3. 100-year annual average ocean ideal age (years) at 500 m (*left*) and 2049 m (*right*) for the **(a, b)** CLOSED, and **(c, d)** NARROW-CLOSED, **(e, f)** WIDESHALLOW-CLOSED, and **(g, h)** WIDE-CLOSED difference in the GFDL-ESM2G seaway simulations.

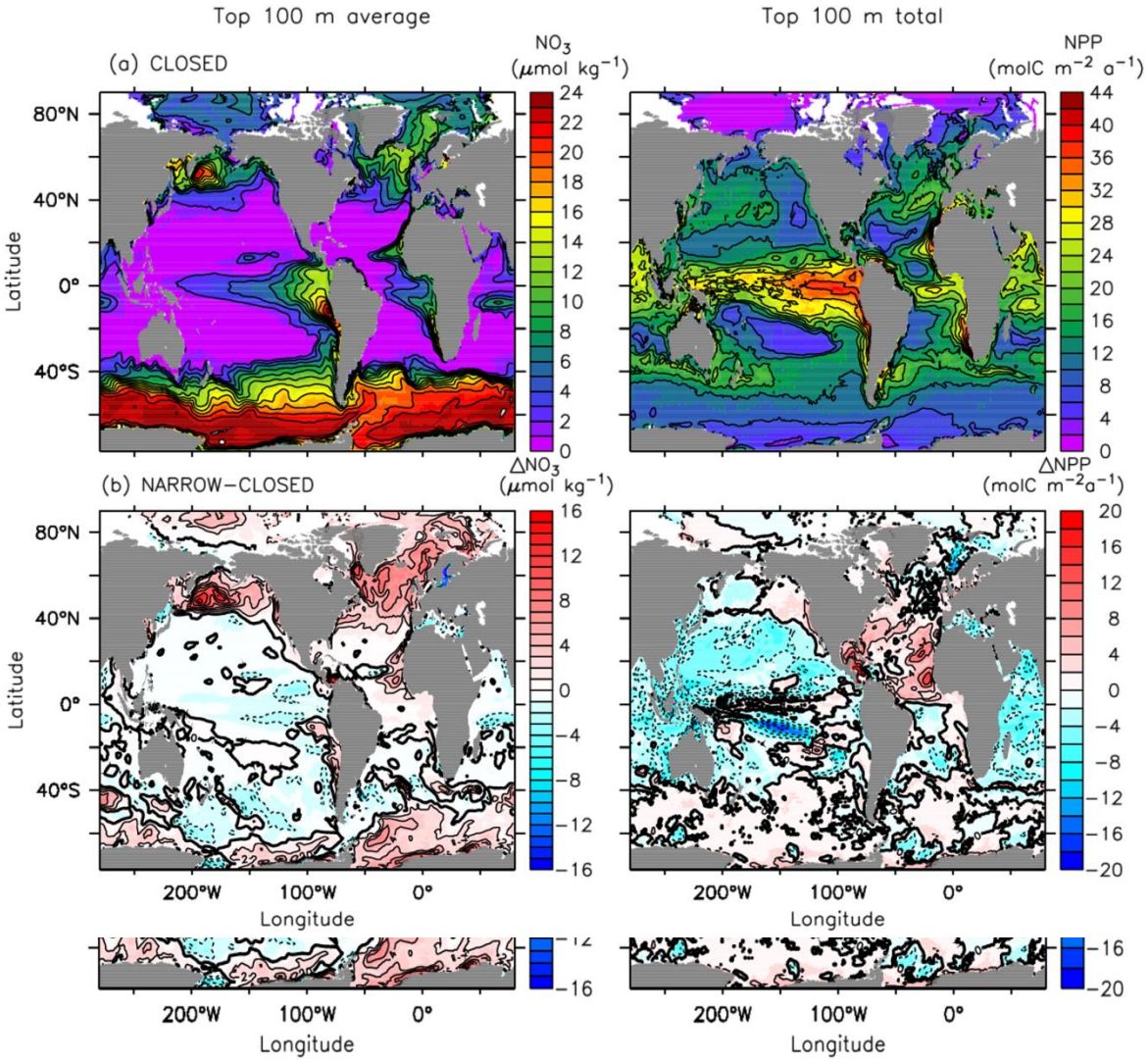

Fig. 5.4. 100-year global annual mean nitrate (NO_3^-) concentration (μmol kg^{-1}) averaged in the top 100 m (*left*) and total net primary productivity (NPP; molC m^{-2} a^{-1}) from NO_3^- using Anderson (1995) stoichiometry integrated in the top 100 m (*right*) for the **(a)** CLOSED and **(b)** NARROW-CLOSED difference in the GFDL-ESM2G seaway simulations.

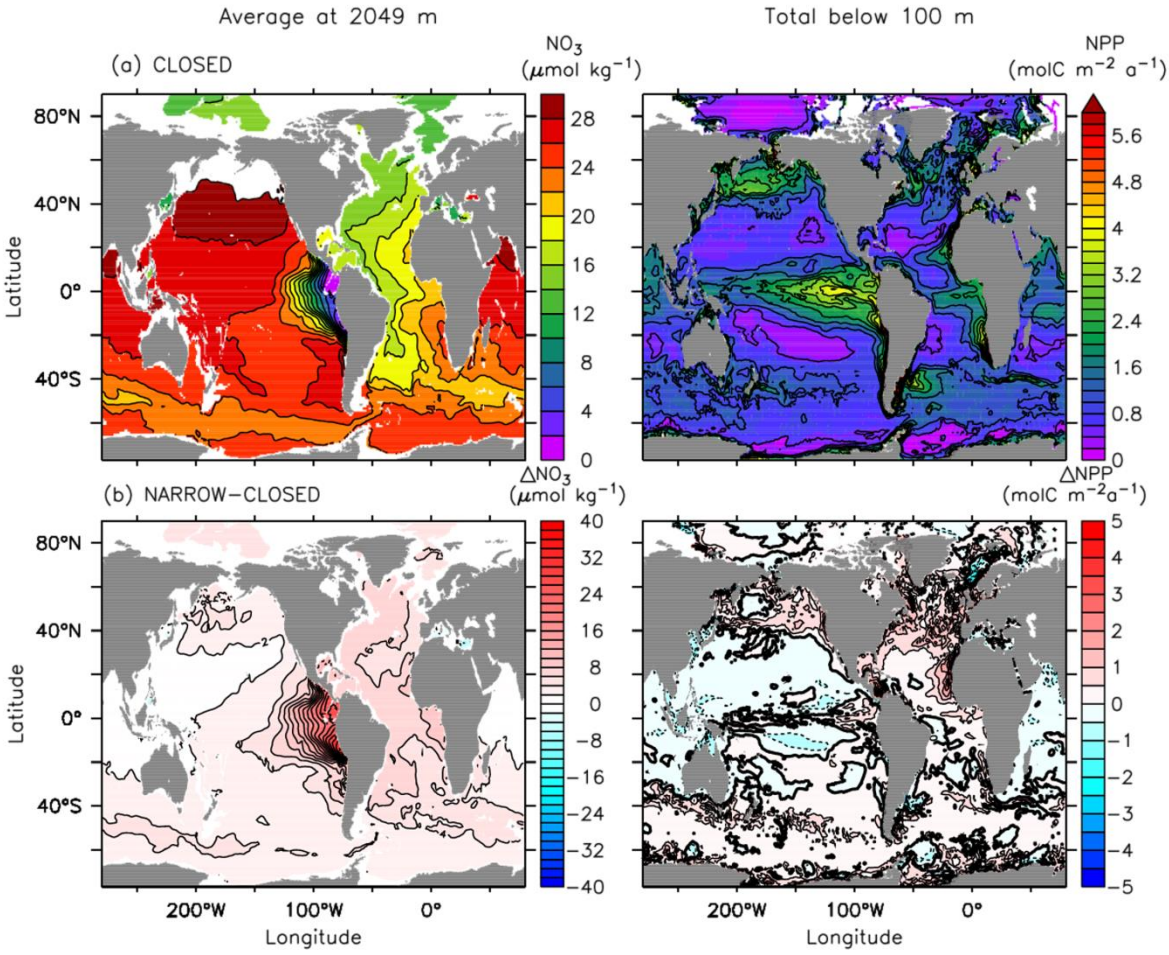

Fig. 5.5. 100-year global annual mean nitrate (NO_3^-) concentration (μmol kg^{-1}) at 2049 m (*left*) and particulate organic nitrogen sinking flux (molC m^{-2} a^{-1}) at 100 m (*right*) using Anderson (1995) stoichiometry for the **(a)** CLOSED and **(b)** NARROW-CLOSED difference in the GFDL-ESM2G seaway simulations.

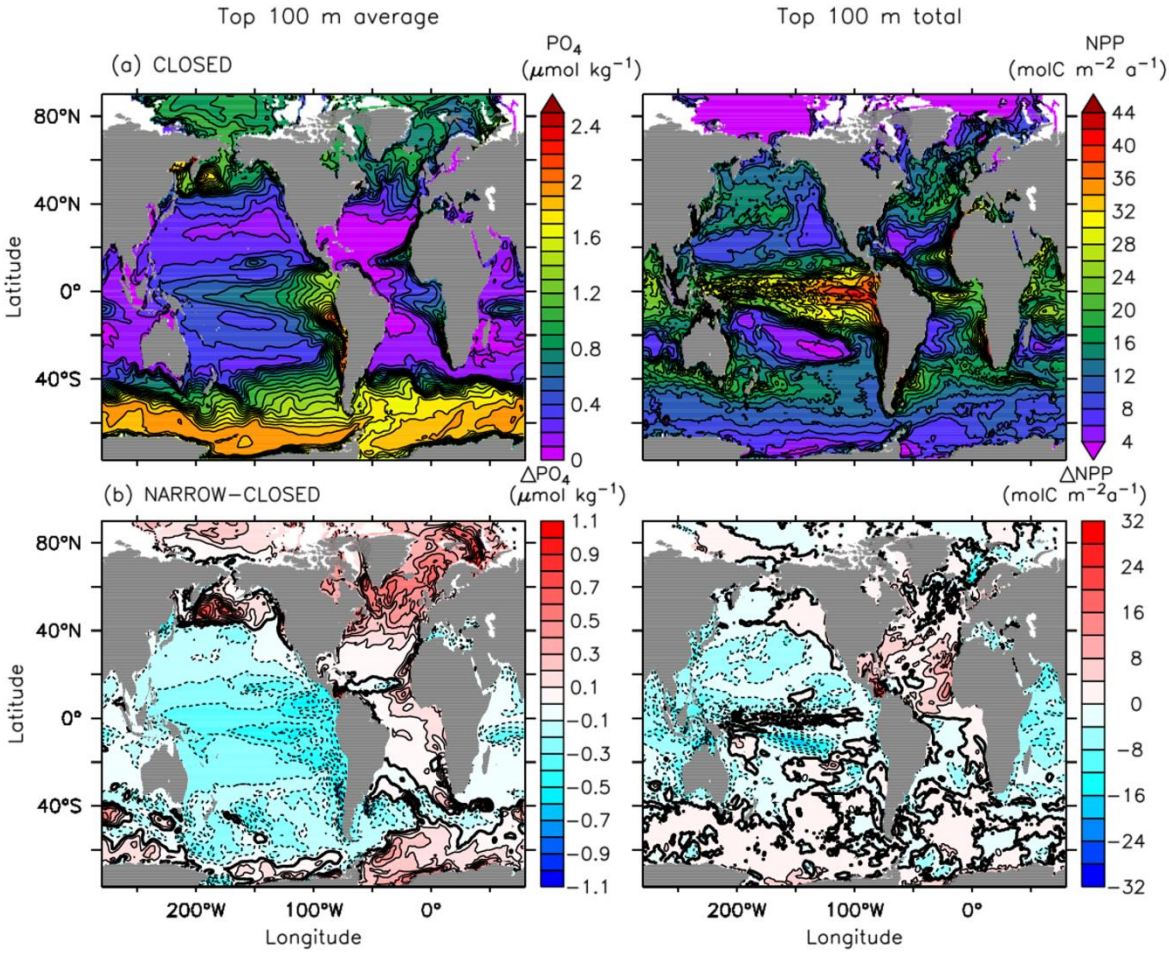

Fig. 5.6. 100-year global annual mean phosphate (PO_4^{3-}) concentration (μmol kg^{-1}) averaged in the top 100 m (*left*) and total net primary productivity (molC m^{-2} a^{-1}) from PO_4^{3-} using Anderson (1995) stoichiometry integrated in the top 100 m (*right*) for the **(a)** CLOSED and **(b)** NARROW-CLOSED difference in the GFDL-ESM2G seaway simulations.

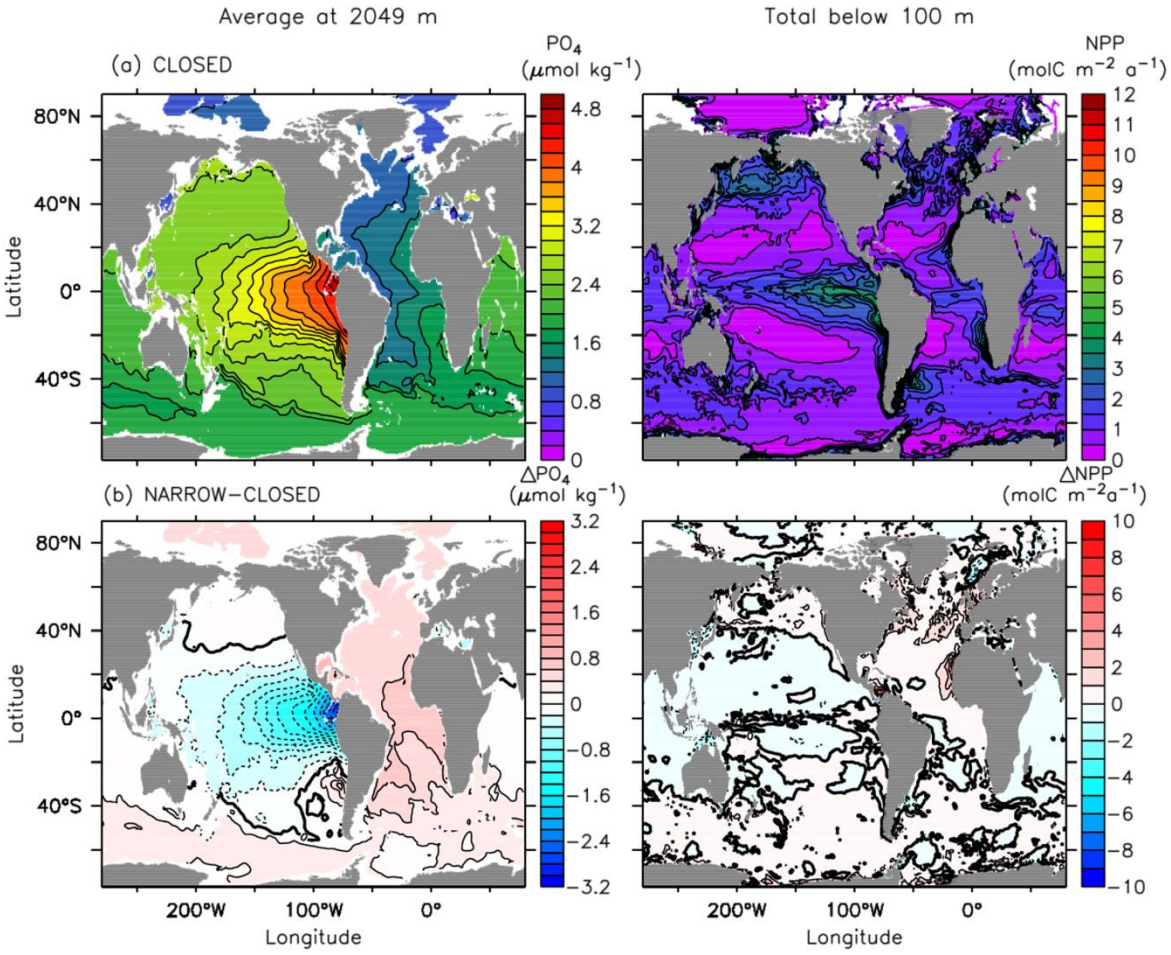

Fig. 5.7. 100-year global annual mean phosphate (PO_4^{3-}) concentration (μmol kg^{-1}) at 2049 m (*left*) and particulate organic phosphate sinking flux (molC m^{-2} a^{-1}) at 100 m (*right*) using Anderson (1995) stoichiometry for the **(a)** CLOSED and **(b)** NARROW-CLOSED difference in the GFDL-ESM2G seaway simulations.

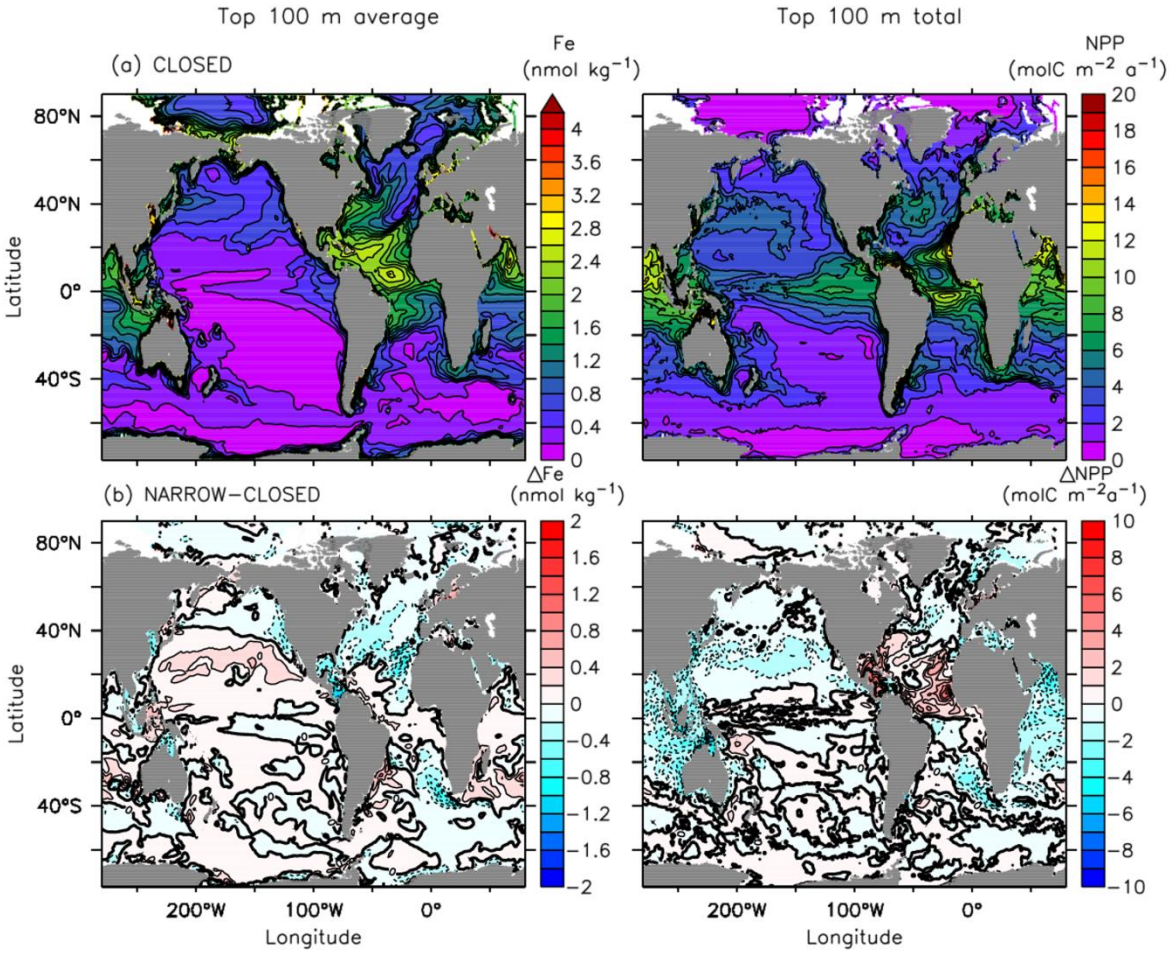

Fig. 5.8. 100-year global annual mean dissolved iron (Fe) concentration (nmol kg^{-1}) in the top 100 m (*left*), at 2049 m (*middle*), and total net primary productivity (molC m^{-2} a^{-1}) from Fe using 10,000C:1Fe stoichiometry (Anderson and Morel 1982; Morel and Hudson 1985) integrated in the top 100 m (*right*) for the **(a)** CLOSED and **(b)** NARROW-CLOSED difference in the GFDL-ESM2G seaway simulations.

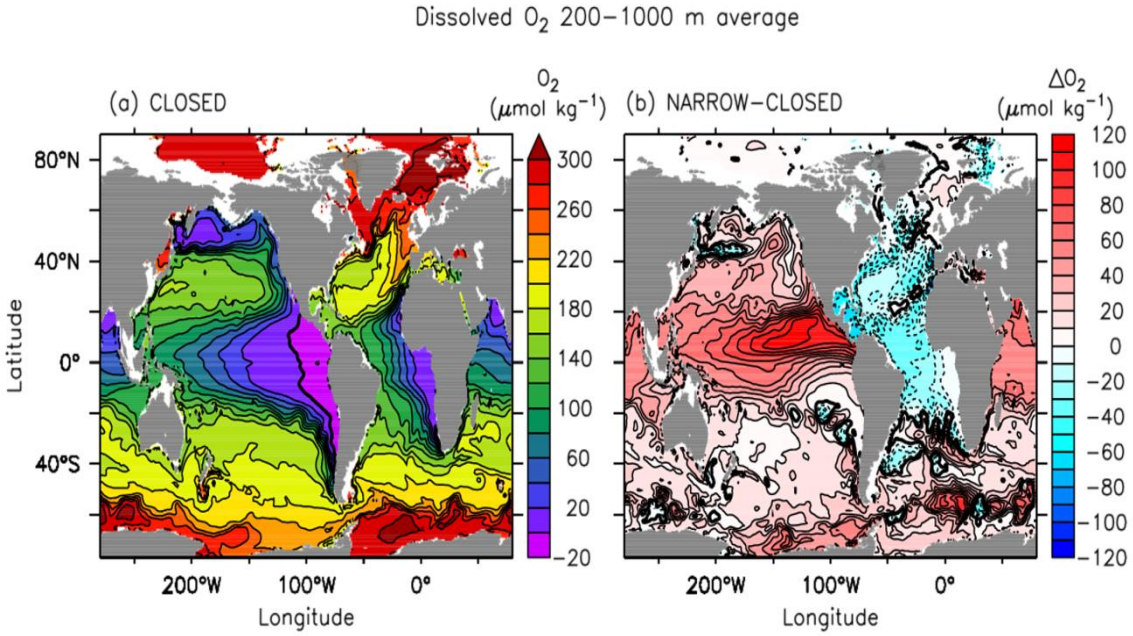

Fig. 5.9. 100-year annual average dissolved oxygen (μmol kg^{-1}) averaged from 200-1000 m for the **(a)** CLOSED and **(b)** NARROW-CLOSED difference in the GFDL-ESM2G seaway simulations.

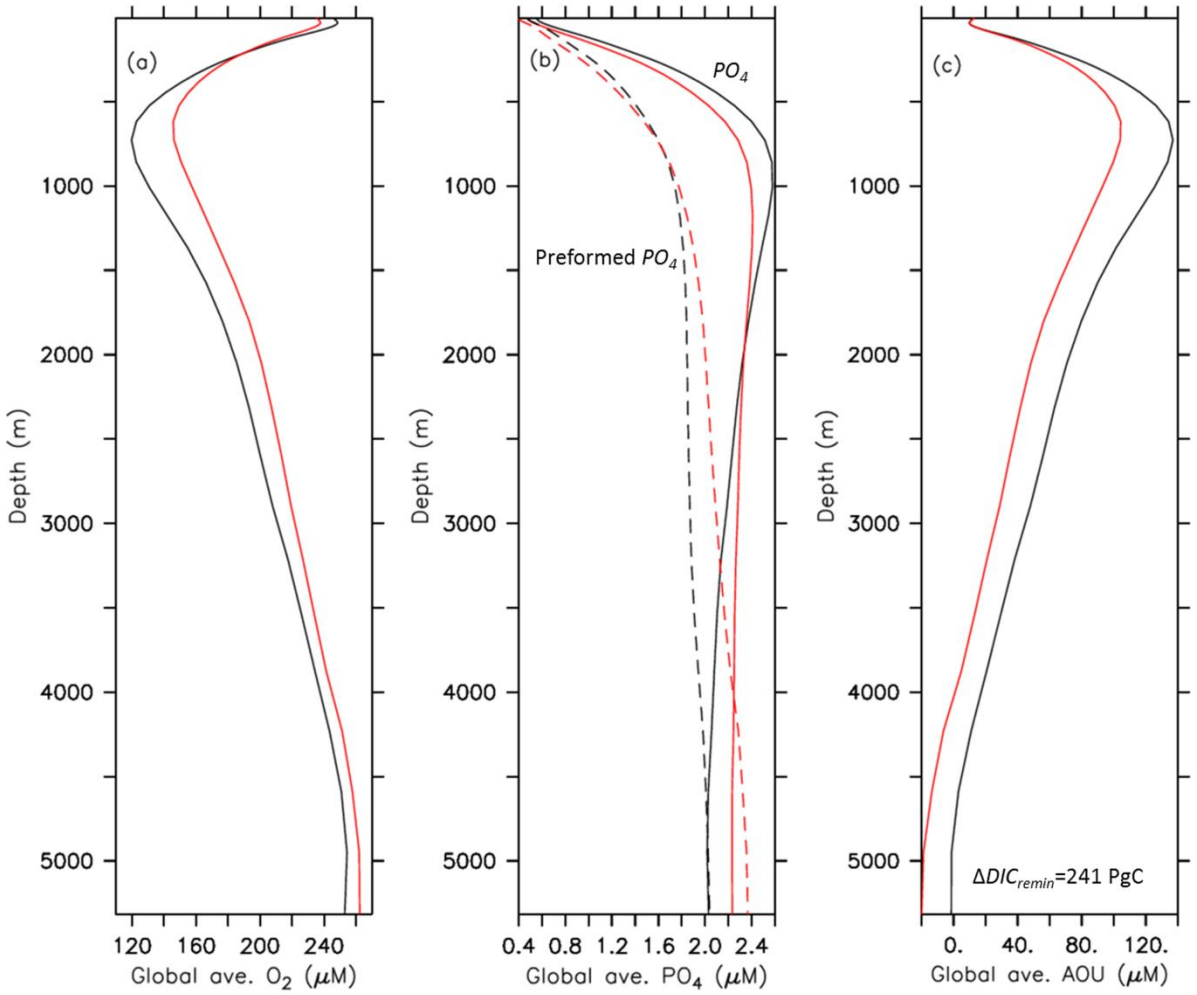

Fig. 5.10. Vertical profiles of global average concentrations of **(a)** dissolved O_2 (μM), **(b)** total (solid) and preformed (dashed) PO_4^{3-} (μM), and **(c)** apparent oxygen utilization (AOU; μM) for the CLOSED (black) and NARROW (red) GFDL-ESM2G seaway simulations. AOU in **(c)** computed from the difference between O_2 at saturation assuming equilibrium with the air-sea interface and actual dissolved O_2 concentrations. The difference in remineralized dissolved inorganic carbon (ΔDIC_{remin}) between the NARROW and CLOSED seaways is 241 PgC released to the atmosphere.

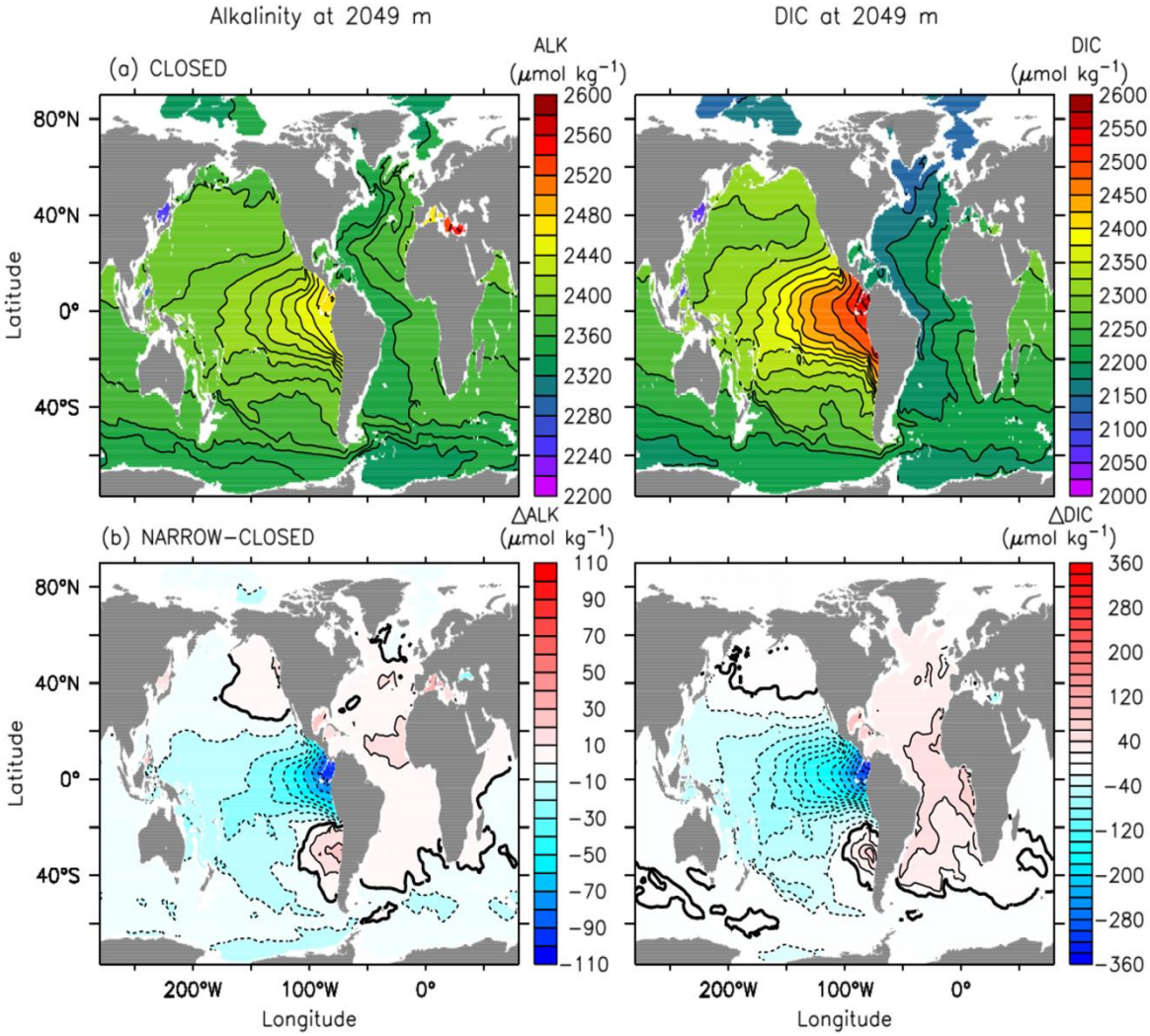

Fig. 5.11. 100-year annual average ocean alkalinity (*left*) and dissolved inorganic carbon, DIC (*right*) at 2049 m depth for the **(a)** CLOSED and **(b)** NARROW-CLOSED difference in the GFDL-ESM2G seaway simulations. Units are in μmol kg^{-1}.

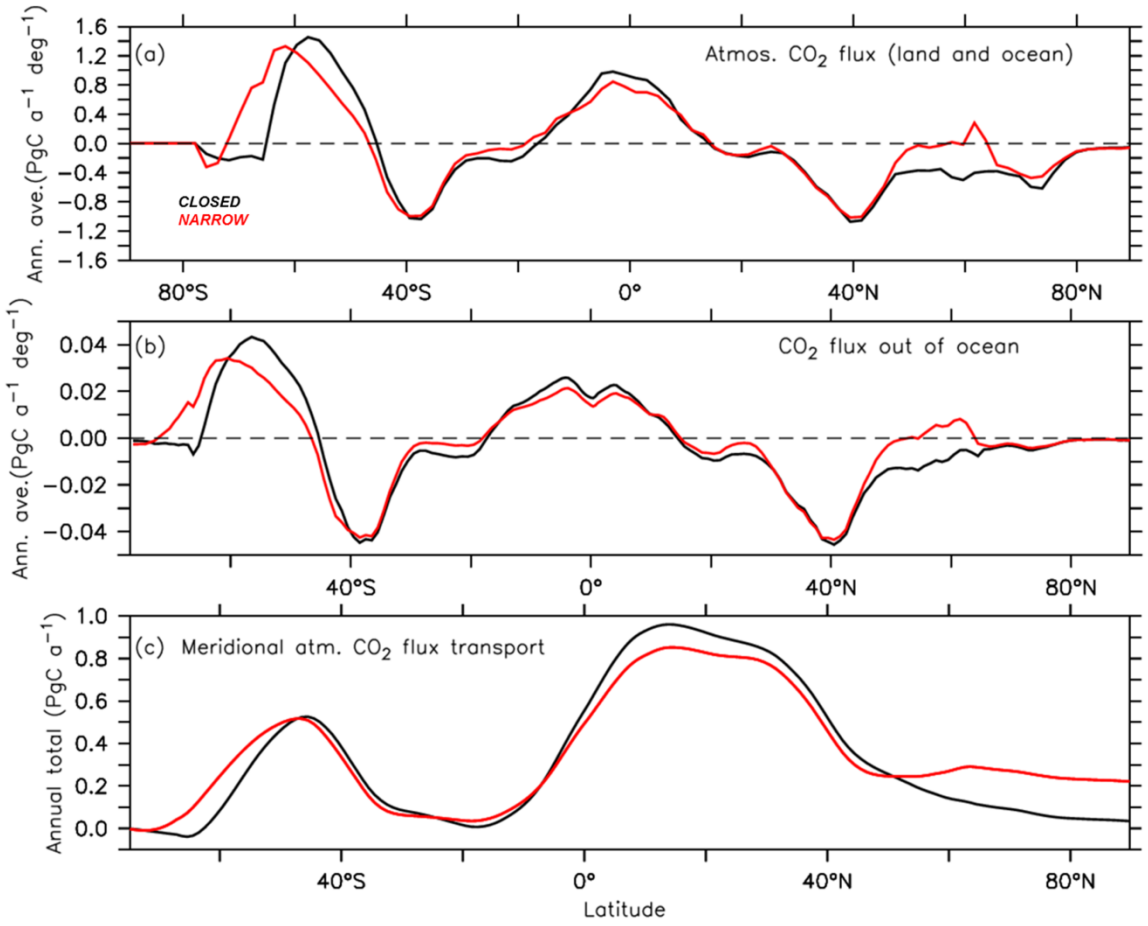

Fig. 5.12. Global 100-year annual zonal average **(a)** atmosphere pCO_2 flux from the land and ocean (PgC a^{-1} deg^{-1}; positive into the atmosphere) and **(b)** from the ocean only (PgC a^{-1} deg^{-1}; positive into the atmosphere), and **(c)** annual total meridional atmosphere CO_2 flux transport (PgC a^{-1}; northward positive) for the CLOSED (black) and NARROW (red) GFDL-ESM2G seaway simulations. Dashed line (zero line) represents the air-sea interface.

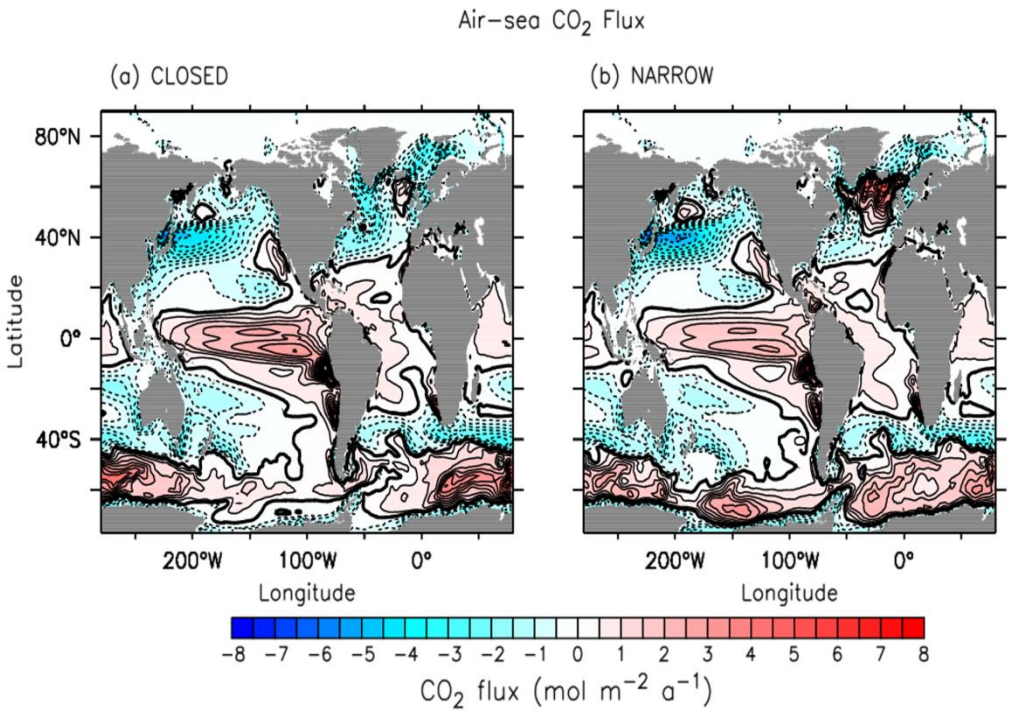

Fig. 5.13. 100-year annual average air-sea CO_2 flux (mol m^{-2} a^{-1}) for the **(a)** CLOSED and **(b)** NARROW GFDL-ESM2G seaway simulations. Positive values (red) indicate a flux out of the ocean.